The International Conference on AI, IoT, Embedded Technologies & Sustainable Energy

AITEC'2024

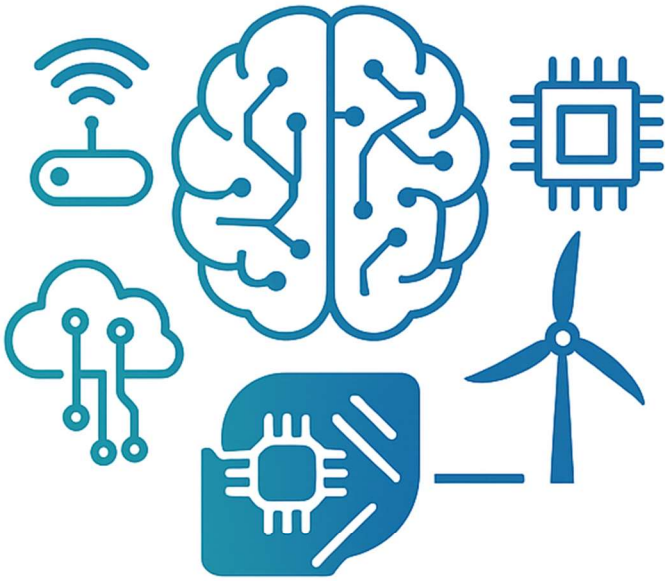

Proceedings

Monastir – Tunisia
December 23-24, 2024

Assessment of Traffic Congestion Impacts on Energy Consumption and Vehicle Emissions at the Urban Roundabout El Gazali, Sousse city

Radhed CHARFI
Departement of Transportation Technology
ISTLS, University of Sousse
Erriadh City 4023, Sousse, Tunisia
charfiradhedh17@gmail.com

Abdessalem JBARA
LESTE Laboratory
ENIM, University of Monastir
Ibn El Jazzar Street, Monastir 5035, Tunisia
j.abdesslem@yahoo.fr

Najah KECHICHE
LMSE Laboratory
ENIM, University of Monastir
Ibn El Jazzar Street, Monastir 5035, Tunisia
kechiche2000@gmail.com

Khalifa SLIMI
LESTE Laboratory
ENIM, University of Monastir
Ibn El Jazzar Street, Monastir 5035, Tunisia
khalifa_slimi@yahoo.fr

***Abstract*— This study aims to assess the impact of road congestion on energy consumption and pollutant emissions at the El Ghazali roundabout in the city of Sousse, Tunisia. The SIDRA Intersection and SUMO simulation tools were employed to analyze two traffic scenarios: congested and free-flow conditions. The results indicate that the roundabout operates at the lowest level of service, leading to poor traffic flow, increased fuel consumption, and higher pollutant emissions. By comparing these scenarios, the study highlights the critical need for traffic management improvements. The findings emphasize the potential for infrastructure enhancements and the promotion of alternative transportation methods to mitigate congestion-related environmental impacts, offering valuable insights for urban planning and transportation policy.**

Keywords*— *congestion, roundabout, level of service, traffic simulation, SIDRA, SUMO, energy consumption, pollutant emissions.

I. INTRODUCTION

Road congestion represents a major challenge for cities around the world, affecting not only the quality of life of urban residents but also environmental sustainability and economic efficiency [1, 2].

In Sousse, Tunisia, the El Ghazali urban roundabout serves as a strategic traffic hub for the city. However, it is frequently subject to significant congestion, especially during peak hours. This congestion has detrimental effects on traffic flow, leading to an increase in fuel consumption and pollutant emissions, thereby exacerbating the region's environmental issues, such as air pollution and greenhouse gas emissions.

This research focuses on modeling and simulating the impacts of road congestion on vehicle energy consumption and pollutant emissions at the scale of an urban roundabout. The main objective of this study is to assess the performance of the El Ghazali roundabout under two traffic conditions, namely free-flow and congested traffic scenarios. To achieve this task, two advanced simulation tools are used: SIDRA Intersection and SUMO [3, 4]. These tools allow for a detailed analysis of traffic dynamics, taking into account various parameters such as vehicle flows, crossing times, and changes in speed and traffic density.

SIDRA Intersection, primarily used for evaluating intersection performance, allows for the calculation of various indicators such as the level of service (LOS), delay times, and queue lengths. On the other hand, SUMO (Simulation of Urban Mobility) is a microscopic simulation tool that offers fine-grained traffic modeling by simulating the behavior of each vehicle and evaluating emissions and energy consumption based on different traffic conditions. The integration of these two tools provides a comprehensive view of the impacts of road congestion, both on the operational performance of the roundabout and on environmental aspects related to fuel consumption and pollutant emissions.

This investigation aims to understand the relationship between traffic conditions and their environmental impacts. By analyzing these interactions, the study proposes recommendations for optimizing traffic management at the El Ghazali roundabout, focusing on strategies to reduce congestion and enhance long-term environmental sustainability. These recommendations may include adjustments to the roundabout design, improved traffic signal management, and solutions for sustainable mobility, such as promoting public transport and active transportation options.

II. METHODOLOGY

A. Presentation of the Study Area

The El Ghazali roundabout, located in Sousse, a coastal city in Tunisia, is a critical urban intersection connecting key routes to the city center and surrounding neighborhoods. Situated at coordinates 35.8282° N, 10.6088° E, it holds a strategic position within the road network, linking the city's entrance to various zones and connecting the highway to other heavily trafficked roads [5].

Surrounded by residential and commercial areas, as well as university campuses and dormitories, the roundabout experiences significant daily traffic through its four main approaches. Despite its multi-lane design, it frequently suffers from severe congestion, particularly during peak hours, due to rapid urbanization and the growing number of vehicles. Figure 1 illustrates the location of this roundabout within the city of Sousse, highlighting its strategic importance in the region.

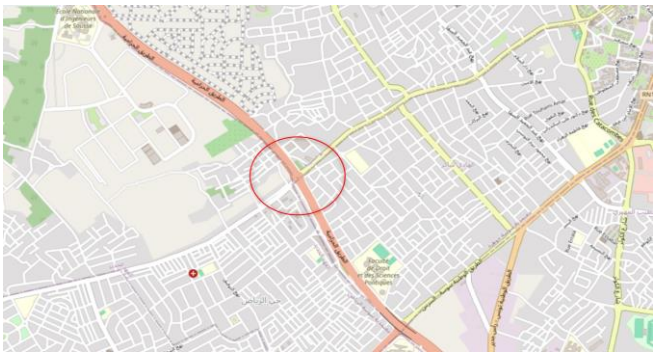

Fig. 1. Geographical Localisation of the Studied Roundabout.

In Sousse, the average frequency of public transport lines during peak hours is approximately 1 hour and 30 minutes, although for the busiest routes, it ranges between 15 and 20 minutes. These lines serve an average of 50 passengers per day, indicating relatively low usage [6]. Furthermore, travel speeds at key congestion hotspots, such as the El Ghazali– roundabout, drop below 10 km/h during peak hours, resulting in significant delays [6]. This study focuses on modeling and simulating traffic at this critical intersection to assess the impacts of congestion on fuel consumption and vehicular emissions, addressing the operational and environmental challenges identified.

B. *Road Traffic Data Collection*

The traffic data collection at the El Ghazali roundabout, conducted over 12 hours and 45 minutes on April 18, 2024, provided a detailed analysis of vehicle flows and categories across its four approaches. The Southwest (SW) and Northwest (NW) approaches were identified as the busiest, with peak traffic recorded between 7:30 AM and 8:30 AM, reaching 6,509 vehicles per hour, as shown in Figure 2.

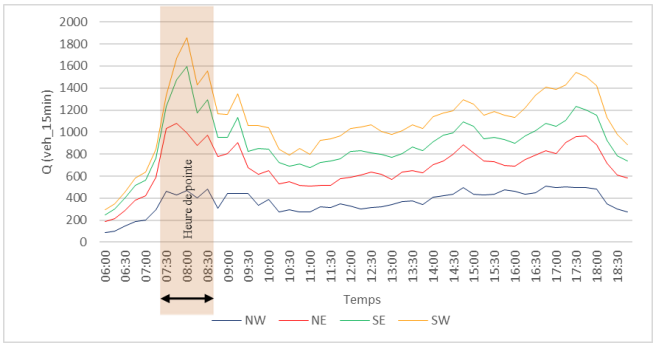

Fig. 2. Traffic Flow Variations at the Roundabout Intersection.

This period corresponded to the morning rush hour, marked by significant congestion. Directional traffic counts conducted on May 2, 2024, showed that light vehicles accounted for 93% of the traffic, while two-wheelers, heavy vehicles, and buses represented 5%, 1%, and 1%, respectively.

In comparison, during the fluid traffic conditions analyzed on May 16, 2024, between 10:00 AM and 11:00 AM, the total traffic volume was significantly lower, with light vehicles accounting for 95% of the flow. The reduction in traffic volume between congested and fluid conditions was approximately 54%, demonstrating a notable decline in overall vehicular flow during non-peak hours. Moreover, the percentage of light vehicles remained stable, highlighting their dominance, while two-wheelers and heavy vehicles showed only minor fluctuations.

This analysis highlights the stark contrast between peak and off-peak traffic conditions at the roundabout, both in terms of volume and flow distribution. The findings emphasize the need for targeted interventions to alleviate congestion during peak hours, particularly on the SW and NW approaches, which are consistently the most congested.

C. *Presentation of the SIDRA Intersection and SUMO tools*

In this study, two tools were used to assess the performance of the roundabout and traffic conditions at its level. The first tool is SIDRA Intersection 8.0 [7], and the second is SUMO 1.12.0 [8].

SIDRA Intersection evaluation steps are summarized as follows:

- Data collection: Gathering roundabout data (geometry, traffic volumes, etc.).
- Model creation: Building the roundabout model in SIDRA based on the collected data.
- Calibration: Adjusting the model to reflect real-world conditions.
- Simulation: Running simulations for various traffic scenarios.
- Analysis: Evaluating performance indicators to identify issues.

Road traffic analysis using SUMO is outlined as follows:

- Data collection: Gathering traffic data from the site.
- Network upload: Upload the road network from OpenStreetMap web site.
- Traffic flow assignment: Setting vehicle flows and define pathways.
- Simulation: Running simulations for various traffic scenarios.
- Analysis: Evaluating performance indicators to identify congestion and suggest improvements.

III. Results and Discussion

A. *Roundabout Performance Evaluation with SIDRA*

- *Level Of Service (LOS)*

The level of service (LOS) analysis of the El Ghazali roundabout reveals severe congestion on all approaches. SE (Southeast), NW (Northwest), NE (Northeast), and SW (Southwest) exhibit a critical LOS of F (Fig. 3). This indicates significant delays and an overall low efficiency for the roundabout.

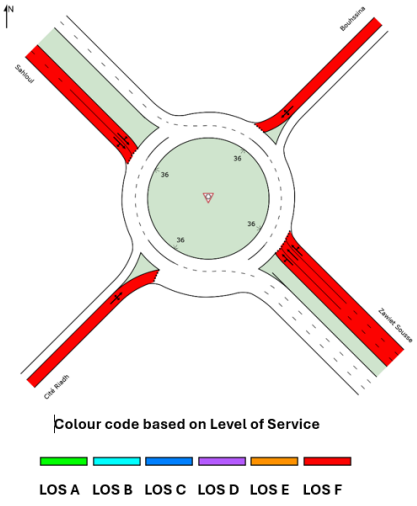

Fig. 3. Level of Service Analysis.

Fig. 3 illustrates the LOS analysis results, with red segments indicating saturated traffic and long vehicle delays. This congestion, caused by the intersection operating beyond its optimal capacity, results in significant vehicle accumulation, prolonged queues, and poor traffic flow. The overall efficiency of the roundabout is severely compromised, leading to extended delays and difficulties for vehicles entering and exiting the intersection.

- *Comparative Study: Free-Flow vs Congested Traffic*

➢ *Average Delay Time*

The average delay times, as shown in Table 1, underscore the significant impact of congestion. Severe delays are recorded in the congested state, reaching 1854.2 seconds for the Northeast direction and 2526.4 seconds for the Southwest direction. In contrast, the free-flow state shows much lower delays, with maximums of 89.2 seconds and 77.5 seconds for the same directions. Overall, a 95% relative difference was observed, highlighting the critical impact of congestion on vehicle waiting times.

TABLE I. AVERAGE DELAY TIME IN SECOND

Congestion					
Delay (s)	Approaches				Intersection
	Southeast	Northeast	Northwest	Southwest	
	54,2	1854,2	51,3	2526,4	799,6
Free-flow					
Delay (s)	Approaches				Intersection
	Southeast	Northeast	Northwest	Southwest	
	16	89,2	13,4	77,5	36,3

➢ *Queue Length*

The queue lengths for both congested and free-flow traffic conditions are shown in Figure 4. In the congested state, the South-West (SW) approach had the longest queue, exceeding 1000 meters, followed by the North-East (NE) approach with a significant queue length of approximately 700 meters. The South-East (SE) and North-West (NW) approaches had much shorter queues, measuring around 130 meters and 172 meters, respectively.

Under free-flowing conditions, the queues were notably shorter, reflecting a less critical traffic situation. The South-West (SW) approach still had the longest queue, but it was considerably reduced compared to the congested scenario.

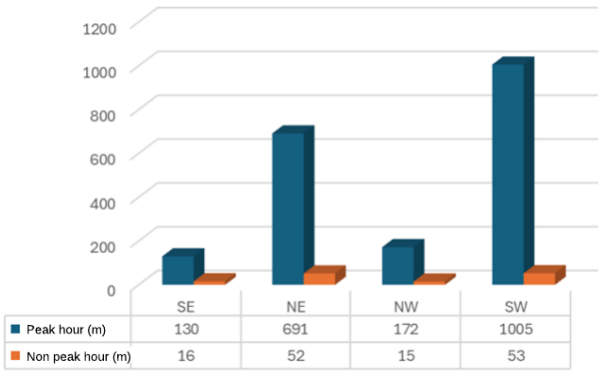

Fig. 4. Queue Lengths in Meter

➢ *Fuel Consumption*

Congestion significantly increases fuel consumption, with vehicles using much more fuel per kilometer in dense traffic compared to free-flow conditions. Fig. 5 shows that the North-East (NE) approach records the highest consumption at 64.4 L/100 km, due to heavy vehicle accumulation and prolonged idling. The South-West (SW) approach shows 10.9 L/100 km under free-flow conditions, indicating inefficiency despite lower traffic pressure.

On average, fuel consumption at the roundabout reaches 32.3 L/100 km in congested conditions, compared to 9.1 L/100 km in free-flow conditions, representing a 72% increase. This highlights the critical impact of congestion on energy efficiency and emissions, emphasizing the need to alleviate traffic at intersections.

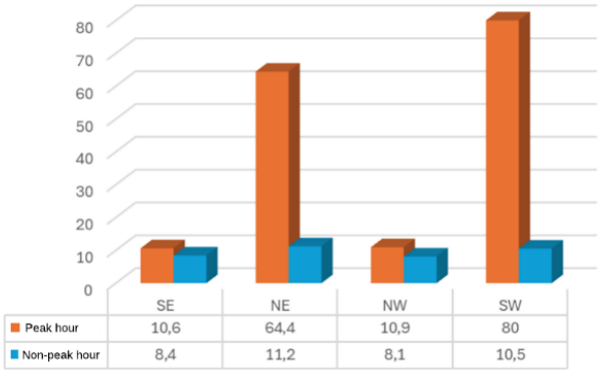

Fig. 5. Average Fuel Consumption in L/100 km

➢ *Vehicle Emissions*

Congested traffic leads to significantly higher CO_2 emissions, particularly in the South-West approach, where emissions reach 3963.9 kg, as shown in Figure 6. Under free-flow conditions, emissions are much lower, at 438.6 kg in the South-West approach, reflecting an 89% reduction. Across the entire intersection during peak hours, total CO_2 emissions amount to 6,937.4 kg under congested conditions, compared to 1,183 kg under free-flow conditions, representing a reduction of 82.94%.

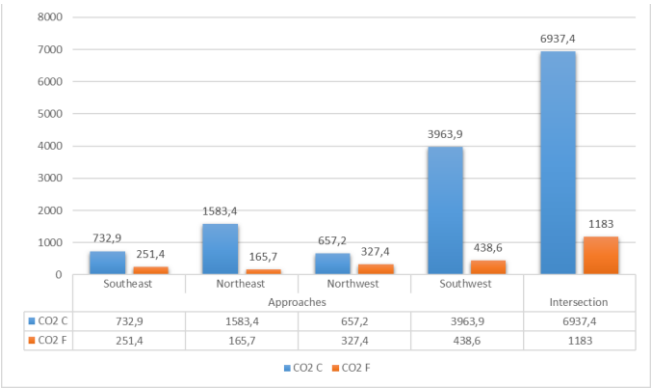

Fig. 6. CO_2 Emissions in Kilogram

In the same context, Figure 7 shows that emissions of carbon monoxide (CO), hydrocarbons (HC), and nitrogen oxides (NO_x) are also higher under congested traffic conditions than in free-flow conditions. CO and HC emissions are significantly elevated in congestion, reaching 0.56 g/km and 0.23 g/km, respectively, compared to 0.092 g/km and 0.02 g/km in free-flow conditions, due unstable operating regime.

The NO_x emissions also increase from 0.139 g/km in free-flow conditions to 0.306 g/km in congestion, though the difference is less pronounced, as NO_x is generated by high

temperatures resulting from abrupt accelerations and prolonged idling.

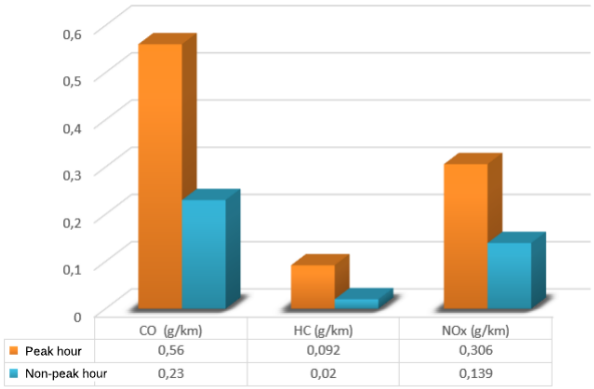

Fig. 7. Average Vehicular Emissions of CO, HC, and NO_x in g/km

In summary, the obtained results indicate that congestion significantly hampers intersection performance, leading to increased wait times, higher fuel consumption, and greater pollutant emissions. This underscores the importance of improving traffic flow at the roundabout to optimize energy efficiency and minimize environmental effects.

B. Microscopic Traffic Analysis with SUMO

- *Speed, Waiting Time, and Lost Time*

Fig. 8 presents three graphs from the SUMO simulation, highlighting clear differences between congested (CONG) and free-flow (FL) traffic conditions. In the congested state, speed is highly irregular, with frequent fluctuations due to repeated stop-and-go cycles, as shown in the first graph, where speed during peak hours varies significantly and often approaches zero.

The second graph illustrates cumulative wait times, which reach significant peaks during congestion, reflecting long delays at intersections or queues.

The third graph highlights lost time, which accumulates rapidly during peak hours, surpassing 600 seconds by the end of the observed period, demonstrating the severe inefficiency caused by congestion.

In contrast, the free-flow state exhibits a much different pattern. Speed remains consistently stable and high, with no significant fluctuations, indicative of smooth traffic flow, as represented in the first graph.

The cumulative wait times during non-peak hours, shown in the second graph, are negligible and stay close to zero throughout, confirming minimal interruptions.

Similarly, the lost time in the non-peak scenario remains minimal, staying below 100 seconds, showcasing the efficiency and fluidity of traffic under free-flow conditions.

Together, these graphs vividly demonstrate the adverse effects of congestion on traffic metrics compared to the favorable conditions in a free-flow state.

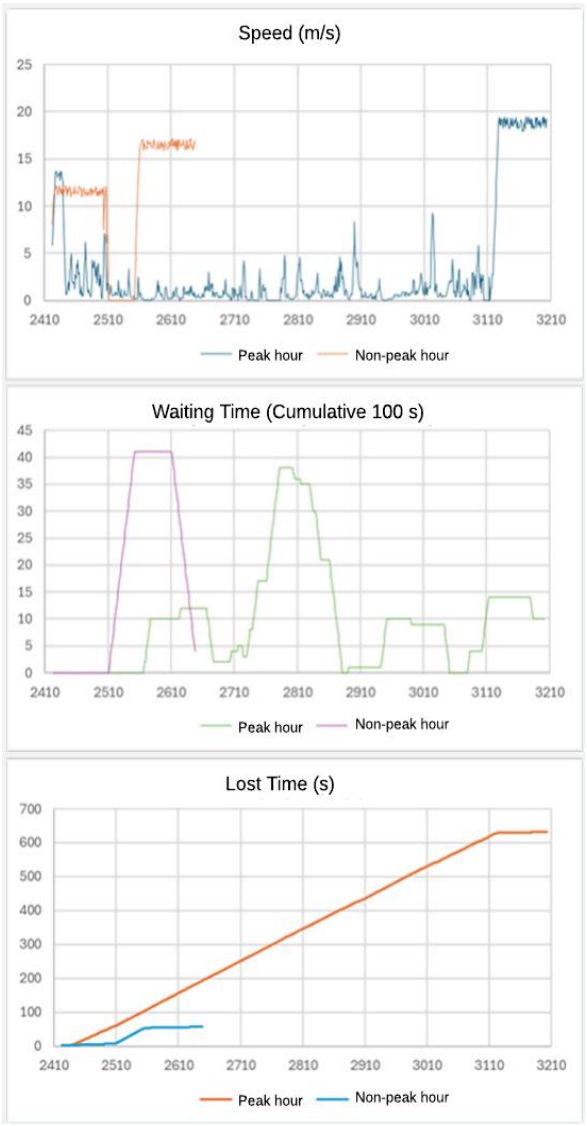

Fig. 8. Speed (m/s), Cumulative Waiting Time (s) , and Lost Time (s)

The results in Table 2 show a significant deterioration in traffic conditions during congestion compared to a free-flowing cycle.

The average speed drops by 76%, from 48.67 km/h to 11.67 km/h, while cumulative wait time increases by 93%, reaching 7,354 seconds compared to just 494 seconds under free-flow conditions.

In the same way, the average lost time rises dramatically by 94%, from 30.74 seconds to 586.48 seconds. These differences highlight the major negative impact of congestion at this roundabout.

TABLE II. SPEED, WAIT TIME, AND LOST TIME FOR THE TWO SIMULATED TRAFFIC SCENARIOS

Driving Cycle	Average Speed (km/h)	Cumulative Waiting Time (s)	Average Lost Time (s)
Free-Flow	48.66	494	30.74
Congestion	11.67	7354	586.48
Difference (%)	76	93	94

The results above emphasize the detrimental effects of congestion, highlighting traffic inefficiencies, whereas smooth traffic flow promotes optimized circulation, minimizes time loss, and improves flow management.

- *Fuel Consumption*

Fig. 9, illustrates the variations in fuel consumption rate (in g/s) during the trip. In congested conditions, the rate peaks at approximately 4.66 g/s, compared to 0.99 g/s under free-flow conditions.

Congestion is marked by more frequent and significant fluctuations in fuel consumption due to repeated stop and go, resulting in an increased fuel consumption rate.

This constant fluctuation forces the engine to operate inefficiently, consuming more fuel during each cycle of acceleration and deceleration.

The increased frequency of idle periods, combined with higher engine loads, contributes to reduced engine efficiency, leading to a higher fuel consumption rate.

In contrast, free-flow conditions allow for smoother and more consistent driving, reducing these fluctuations and resulting in lower fuel consumption rates.

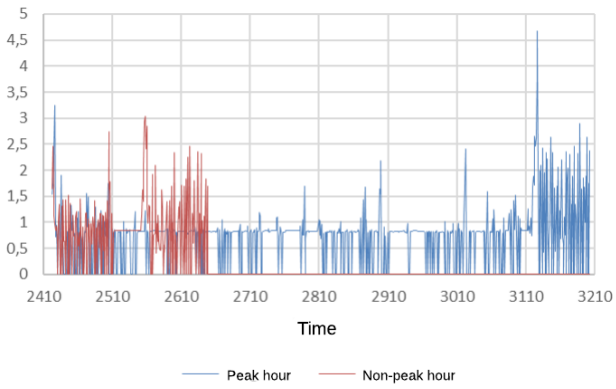

Fig. 9. Fuel Consumption Rates (g/s) for the Two Simulated Traffic Scenarios.

- *Atmospheric Emissions*

Fig. 10 provides a macroscopic view of CO2 emissions using the SUMO Graphical User Interface (GUI) at the El Ghazali roundabout. The figure clearly shows that CO2 emissions can reach up to 6000 g along the analyzed site during peak hours.

Greenhouse gases like CO_2 trap heat in the Earth's atmosphere, creating the "greenhouse effect," which is essential for maintaining the planet's temperature but problematic when intensified due to excessive emissions. CO_2 accounts for the largest share of human-induced GHG emissions and has a long atmospheric lifetime, contributing significantly to climate change.

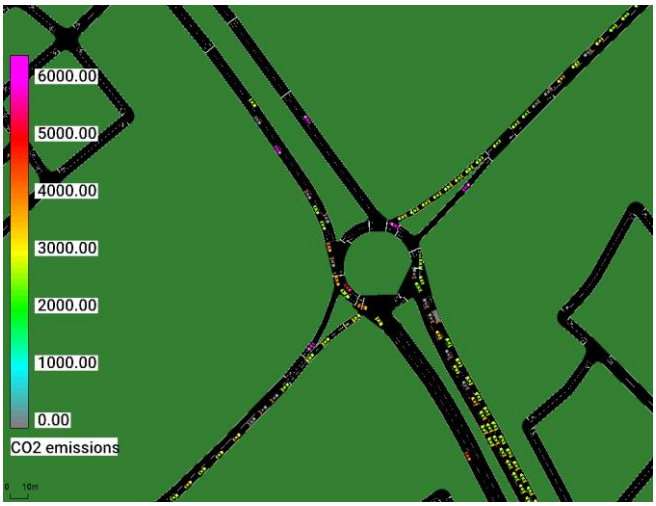

Fig. 10. CO_2 Simulation Results in SUMO Graphical User Interface

Fig. 11 highlights the frequent spikes in CO_2 emissions under congested conditions, driven by speed instabilities, frequent stops, and go, all of which significantly increase emissions. In contrast, free-flow (FL) conditions exhibit lower and less intense CO_2 emissions, attributed to consistent driving at stable speeds. Similarly, emissions of carbon monoxide (CO) and nitrogen oxides (NO_x) are notably higher during congestion, as repeated stops and go reduce engine efficiency. Hydrocarbon (HC) and particulate matter (PM_x) emissions also rise, primarily due to unstable combustion caused by frequent speed fluctuations.

These findings emphasize the adverse effects of congestion, where traffic inefficiencies result in elevated emissions compared to the benefits of smooth traffic flow. Efficient flow management reduces time losses, optimizes fuel consumption, and minimizes environmental impacts. Congested driving cycles, characterized by irregular speed patterns, create suboptimal conditions, leading to higher emissions of CO_2, CO, NO_x, HC, and PM_x due to continuous engine strain.

The importance of maintaining smooth traffic flow cannot be overstated in efforts to reduce emissions. Effective flow management and infrastructure improvements can help mitigate the negative impacts of congestion. The fuel consumption is significantly higher during congestion due to repeated acceleration and deceleration, further emphasizing the strong correlation between fuel use and pollution. Optimizing driving cycles by reducing stops and promoting steady speeds presents a viable strategy to lower both fuel consumption and pollutant emissions.

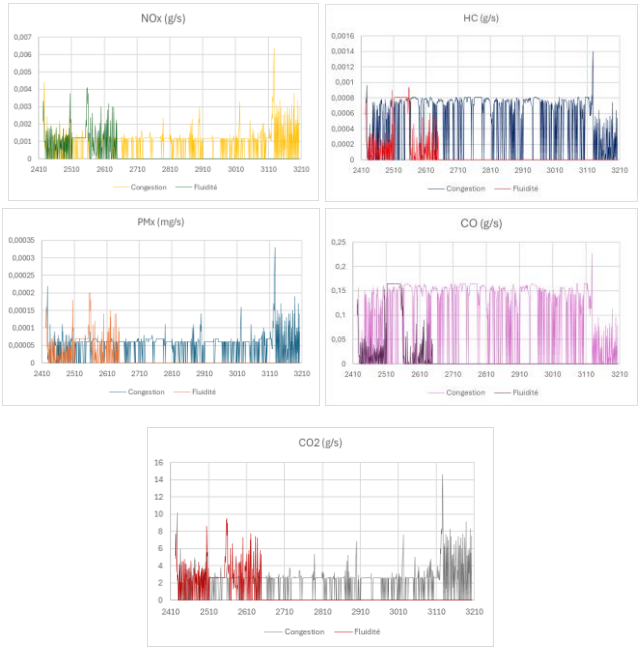

Fig. 11. Atmospheric Emissions for the Two Simulated Scenarios

IV. Recommendations for Mitigating Traffic Congestion

One possible solution is to widen the access lanes to the roundabout to enhance traffic flow management. For instance, the capacity of the roundabout could be increased by adding additional lanes to the South-West (SW) approach, provided adequate space is available, as illustrated in Figure 12. Another strategy involves minimizing conflict points by introducing bypass lanes to reduce the volume of traffic entering the roundabout.

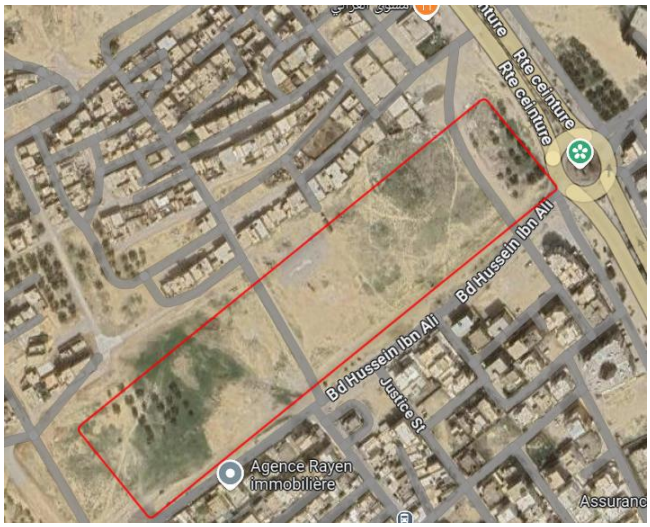

Fig. 12. Proposal to Add Supplementary Lanes on the SW Branch of the Roundabout.

Several strategies can be implemented to alleviate congestion. Promoting sustainable transportation modes, such as cycling and walking, through the development of safe bike lanes, and improving bus services to encourage greater public transit use are key measures.

Traffic simulation tools like SUMO or VISSIM can be employed to evaluate various design scenarios, optimizing traffic flow while reducing energy consumption. Installing traffic sensors and cameras for real-time data collection enables adaptive traffic management, enhancing congestion control. Furthermore, educating drivers on safe driving practices and utilizing dynamic signage to suggest alternative routes can help reduce traffic volumes and discourage behaviors that exacerbate delays.

V. Conclusion

In conclusion, this research underscores the critical role of proactive urban infrastructure planning and management in mitigating the adverse effects of congestion. The proposed solutions such as optimizing roundabout design, encouraging sustainable mobility, and implementing intelligent transport systems (ITS) present effective strategies for improving traffic flow and air quality in the study area. These findings provide a solid foundation for shaping traffic management policies that integrate sustainable and environmentally friendly practices.

For future research, the study area could be expanded to encompass an entire road network, enabling a more comprehensive analysis. Additionally, artificial intelligence tools could be employed to monitor traffic patterns, fuel consumption, and emissions, particularly during peak hours, to further enhance traffic efficiency and environmental outcomes.

References

[1] V. Lomendra, P. Sharmila, D. Ganess and N. Vandisha, "Assessing the causes & impacts of traffic congestion on the society, economy and individual: A case of Mauritius as an emerging economy," Studies in Business and Economics, vol 13(3), pp. 230-242, 2018.

[2] J. Borut, S. Kumperščak, and T. Bratina, "The Impact of Traffic Flow on Fuel Consumption Increase in the Urban Environment," Fme Transactions, vol 46 (2), 2018.

[3] R. Prakash, A. Shahin, and F. Shirwali, "Evaluating operational performance of intersections using SIDRA." The Open Transportation Journal, vol 8 (1), 2014.

[4] B. Leite, P. Azevedo, R. Leixo and R. J. F. Rossetti, "Simulating a three-lane roundabout using SUMO," International Conference on Intelligent Transport Systems (INTSYS 2019). Cham: Springer, pp 18–31, 2020.

[5] Technical Report, “Plan des Déplacements Urbains (PDU) de la ville de Sousse Objectifs, contenu et organisation du projet,” Available on : https://medcities.org/documents/Presentation+PDU+de+Sousse.pdf

[6] Technical Report “Programme de développement urbain intégré de la ville de Sousse Plan de Déplacements Urbains du Grand Sousse Rapport technique de la mission 2 : Diagnostic de la mobilité & orientations stratégiques,” Available on : www.transitec.net

[7] A. S. I. Albrka, R. Reşatoğlua, H. Tozan, “Evaluation and Analysis of Traffic Flow at Signalized Intersections in Nicosia Using of SIDRA 5 Software,” Jurnal Kejuruteraan, vol 30(2), pp. 171-178, 2018.

[8] M. Zaky, D. G. Airulla, E. Joelianto, H. Y. Sutarto, “Urban traffic simulation using SUMO open source tools,” Internetworking Indonesia Journal vol 9(1), pp. 83-88, 2017.

Numerical Analysis of Earth-to-Air Heat Exchanger Integrated with Thermo-Electric Cooling for Air-Cooling Applications in Saudi Arabia

M. O. Yousof
Mechanical Engineering Dept
University of Sheffield
Sheffield, United Kingdom
Myousof1@sheffield.ac.uk

M. Ouzzane
Ecole Nationale Polytechnique d'Alger
Algiers, (Algeria)
Mohamed.Ouzzane@usherbrooke.ca

K. J. Hughes
Mechanical Engineering Dept
University of Sheffield
Sheffield, United Kingdom
k.j.hughes@sheffield.ac.uk

***Abstract*— In Saudi Arabia, where HVAC systems dominate electricity use, this study proposes combining an Earth-to-Air Heat Exchanger (EAHE) with a Thermo-Electric Cooling (TEC) device to improve cooling efficiency. A numerical model has been developed to simulate system behavior, showing promising results for reducing air temperatures while optimizing performance for different pipe lengths.**

Keywords—HVAC systems, Earth-to-Air Heat Exchanger (EAHE), Thermo-Electric Cooling (TEC), Geothermal energy, Cooling efficiency, Transient thermal behavior.

I. INTRODUCTION

Saudi Arabia's Vision 2030 prioritizes reducing oil dependency and expanding renewable energy to meet increasing energy demands while cutting carbon emissions [1, 2]. Residential HVAC systems currently consume 50% of the country's electricity, especially during peak times, necessitating efficient cooling solutions [3]. This study focuses on using shallow geothermal energy, Earth to Air Heat Exchanger (EAHE) which is a sustainable and locally available resource, for air conditioning in hot climates like Saudi Arabia. Shallow geothermal systems utilize stable underground temperatures at 2–4 meters depth to provide efficient cooling through heat pumps or heat exchangers [4] Despite its environmental benefits, geothermal energy must be optimized to address the country's high cooling demand [5]. This research investigates integrating shallow geothermal systems (EAHE) with thermo-electric coolers (TEC) to enhance cooling efficiency and reduce energy consumption. By combining these technologies, the study aims to provide innovative solutions for sustainable HVAC systems, aligning with Saudi Arabia's renewable energy goals and contributing to Vision 2030.

A. EARTH TO AIR HEAT EXCHANGER (EAHE)

Shallow Geothermal Energy refers to heat extracted from the ground from a couple of meters up to 200m. This type of geothermal energy is affected by the solar radiation that is absorbed by the ground, which acts as a solar battery. To utilize this heat, a heat pump or any form of heat exchanger is needed [6].The main advantage of the shallow level is that the temperature becomes approximately constant after a certain depth and this is typically 2-4 meres. The Kasuda equation [7]. This behaviour could be used in many applications such as EAHE

The Earth-to-Air Heat Exchanger (EAHE) is an energy-efficient technology that uses underground pipes to cool or heat air by utilize the stable temperatures of the soil. Acting as an auxiliary system for air conditioning, EAHE reduces energy demand while improving indoor comfort. It operates by transferring heat through conduction and convection, providing cooling for ventilation air in summer and preheating in winter [8][9].

The EAHE outlet temperature is influenced by factors like location, depth, pipe dimensions, thermal conductivity, airflow velocity, and the system configuration. Due to the soil's thermal inertia, underground temperatures fluctuate less than surface temperatures, enabling EAHE to cool air in summer and warm it in winter effectively. Advantages of EAHE include its use of air as a working fluid, eliminating the need for CFCs and reducing environmental pollution. It consumes less energy than conventional systems, relying only on a fan, as opposed to energy-intensive compressors. EAHE also features a simple design, low maintenance requirements, and a dual function for heating and cooling without modifications, making it cost-effective and energy efficient. However, EAHE has some disadvantages, such as high initial installation costs due to excavation, non-uniform pipe temperatures caused by air convection, and the risk of microbial growth in ventilation systems [10]. Furthermore, in extreme climates such as South Algeria, where summer temperatures reach 45°C, EAHE alone cannot meet cooling demands [11].

B. THERMO-ELECTRIC COOLER (TEC)

The Peltier phenomenon occurs when a temperature difference occurs between the thermocouple's two junctions, thus causing one side of the Peltier to become cold and the other to become hot [12]. Furthermore, with the consumption of electricity, a Peltier module is used to transfer heat from a hot region to a comparatively cold region of space. This cooling is a solid-state heat transfer technology that uses P-type and N-type semiconductors to generate heat [13]. A key feature of thermo-electric elements is that changing their polarity reverses the hot and cold junctions, as well as the heat absorption and rejection. Compared to vapor compression systems, Peltier coolers offer advantages such as no moving parts (e.g., compressors), no leaks, and no refrigerant gas. Other benefits include being quieter, more durable, dependable, low-maintenance, portable, compact, and environmentally friendly with no ozone depletion potential [13]. However, Peltier modules have disadvantages like higher cost and a low coefficient of performance (COP), typically less than 0.5 for refrigerators operating at a temperature difference of 20 K [14]. COP can be improved by selecting materials with a high Figure of Merit (Z), which indicates the material's suitability for thermoelectric applications [14]. Thermo-electric coolers are used in portable coolers, electronic devices, medical applications like blood transport, and air conditioning systems. A study by Bansal et al. [15] compared energy consumption and costs between thermoelectric, vapor compression, and absorption systems of equivalent capacity, finding that thermoelectric systems performed and costed between vapor compression and absorption systems.

The objective of this study is to propose a mathematical and numerical model for a cooling system model for hot climates using geothermal energy by combining Earth to Air Heat Exchanger (EAHE) and Thermo-Electrical Cooling (TEC) to achieve a significant temperature reduction of the supplied air.

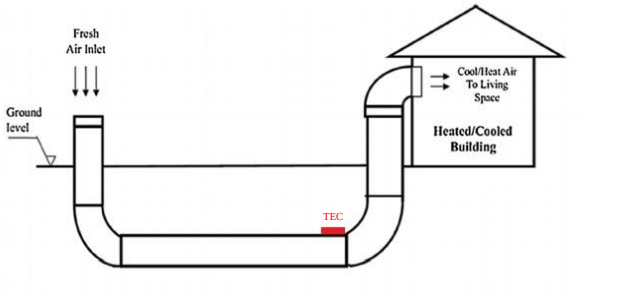

Figure 1. EAHE-TEC System [16]

II. METHODOLOGY

A. *Mathematical Model*

The mathematical model is divided into two parts, one for EAHE and the other for TEC for simplicity. Figure 2 illustrates how the system has been divided and shows all the components. Finite volume method FVM has been used for solving the system equations.

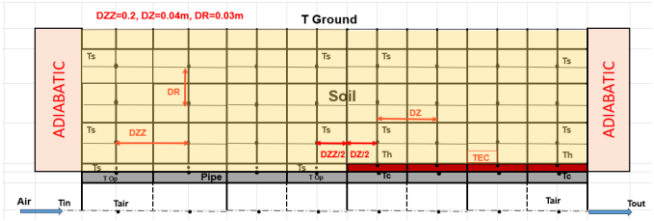

Figure 2. EAHE-TEC FVM schematic.

a. Earth to air heat exchanger (EAHE)

The theoretical model adopted in this work has been applied in many research studies (Samia Hamdane et al. [17]) and in terms of accuracy, it has shown enough satisfaction for this type of problem. This model is based on the following main assumptions:

- In the ground, the problem is transient two-dimensional heat conduction.
- In the buried pipe, the problem is one-dimensional convective heat flow.
- The ground includes the pipe, is considered as a horizontal cylinder, and the problem is axisymmetric.
- One half of the domain is taken for simplicity of calculations.
- All properties of the soil, pipe and air are constant.
- The left and right boundaries of the system are assumed to be adiabatic.

In the soil, the physical problem is purely based on heat transfer by conduction characterized by the following fundamental differential equation in cylindrical coordinates (r,z):

$$\frac{\partial T}{\partial t} = \alpha_s \left(\frac{1}{r} \frac{\partial T}{\partial r} \left(r \frac{\partial T}{\partial r} \right) + \frac{\partial^2 T}{\partial z^2} \right) \quad (1)$$

A fan drives the air in the pipe and exchanges heat with the ground across the interface (soil/pipe). The energy conservation equation applied to the element of air in the pipe is given by:

$$\dot{m} Cp_a \frac{\partial T_a}{\partial z} = U.2\pi.R_{po}\left(T(r = R_{po}) - T_a\right) \quad (2)$$

The heat flux from the air is equal to the heat flux received by soil according to the following equation:

$$k_s \cdot \left.\frac{\partial T}{\partial r}\right|_{R_{po}} = U\left(T(r = R_{po}) - T_a\right) \quad (3)$$

Where: U is calculated by the following equation:

$$U = \left[\frac{1}{2\pi R_{pi} \Delta z h} + \frac{1}{2\pi k_p \Delta z} \ln\left(\frac{R_{po}}{R_{pi}}\right) \right]^{-1} \quad (4)$$

The initial and boundary conditions adopted in this work are:

$T(r,z,t=0) = TG$

$T(r < Ri, z=0,t) = T_{amb}$

$T(r > Ro, z=Lp,t) = T(r = R_{lim},z,t) = TG$

The table below summarizes the key parameters used in the analysis, including dimensions, material properties, and environmental conditions.

Table of the system Parameters		
Parameter	***Value***	***Description***
Ri	0.1016 m	Inside Diameter (8 inches)
Ro	0.10953 m	Outside Diameter (8.625 inches)
DZZ	0.2 m	Mesh in Z-dir of NOTEC
DR	0.03 m	Mesh in R-dir
NG	80	Number of Nodes along R-dir
VELO	2.5 m/s	Air Velocity
VOLT	6 V	TEC Voltage
NTEC	10	Number of TECs used
TG	304.15 K	Ground Temperature (31°C)
Tamb	318.15 K	Ambient Temperature (45°C)
Tair in	318.15 K	Initial Temperature
Δt	900 s	Time Step
ρ_{Air}	1.225 kg/m³	Air Density
Cpa	1005 J/kg·K	Air Specific Heat
κ_{Air}	0.0242 W/m·K	Air Thermal Conductivity
υ_{Air}	1.85×10^{-5} Pa·s	Air Dynamic Viscosity
PRNTL	0.7144	Prandtl Number
ρ_{soil}	1800 kg/m³	Soil Density
Cps	1340 J/kg·K	Soil Specific Heat
κ_s	1.5 W/m·K	Soil Thermal Conductivity
κ_p	0.16 W/m·K	Pipe Thermal Conductivity
ρ_p	1300 kg/m³	Pipe Density
Cpp	900 J/kg·K	Pipe Heat Capacity

Table 1: EAHE -TEC system parameters

b. Thermo-Electric Cooler (TEC)

Zhaoxia [18] suggested a method to estimate the physical characteristics of a thermoelectric cooler from a vendor datasheet. This method has been used and Table 2 illustrates thermoelectric characteristics of the model RS 2172399.

Thermo-Electric Characteristics			
R_M (Ω)	2.32208317	Z (1/K)	0.002384185
α_M (V/K)	0.079220176	Model Size (mm)	40 × 40 × 3.3
K_M (W/K)	1.133584521		

Table 2: Thermo-Electric characteristics of the model RS 2172399

Where Seebeck coefficient, α_M, is defined as the ratio of the generated electric voltage to the temperature difference.
R_M is electrical resistivity in Ohm and K_M is thermal conductivity in W/K.
The Peltier heat transfer equation describes the amount of heat transferred at a junction due to the Peltier effect

$$Q_{Peltier} = \alpha \times T \times I \quad (5)$$

'T' is the temperature at the junction of two materials and 'Q' is the amount of heat transferred per unit time.
The net heat removed from the cold junction is given by

$$Q_C = \alpha \times T_C \times I - 0.5 \times I^2 \times R - K \times \Delta T \quad (6)$$

The amount of heat rejected from the hot side is obtained as

$$Q_h = \alpha \times T_h \times I - 0.5 \times I^2 \times R - K \times \Delta T \quad (7)$$

The electrical power (W) across the thermo-couple

$$W = Q_h - Q_C \quad (8)$$

$$W = \alpha \times I \times (T_h - T_C) + I^2 \times R \quad (9)$$

Voltage across the couple

$$V = \alpha \times (T_h - T_C) + I \times R \quad (10)$$

Coefficient of performance or thermal efficiency

$$COP = \frac{Qc}{W} \quad (11)$$

The initial conditions adopted for TEC are:
TC= 288.15 K , TH= 316.15K , I= 1.6 Amp

B. Numerical Model

FORTRAN

Fortran (Formula Translation) is a programming language often used for solving scientific and math problems. It is very fast at handling complex calculations and is popular in fields like science and engineering [19]. Fortran is especially useful for solving systems of equations in areas like physics, engineering, and computational science. It is good at working with large amounts of data and doing complicated calculations. The flowchart below, Figure3, shows the steps involved in solving the equations, explaining the process in order.

The system has been solved for the following unknowns: air temperature (T_{air}), temperature of the outer surface of the pipe (T_{pipe}), cold-side temperature of TEC (TC), hot-side temperature of TEC (TH), electrical current that is needed to power TEC (I), and temperatures of multiple Nodes in the soil (T_{soil}).

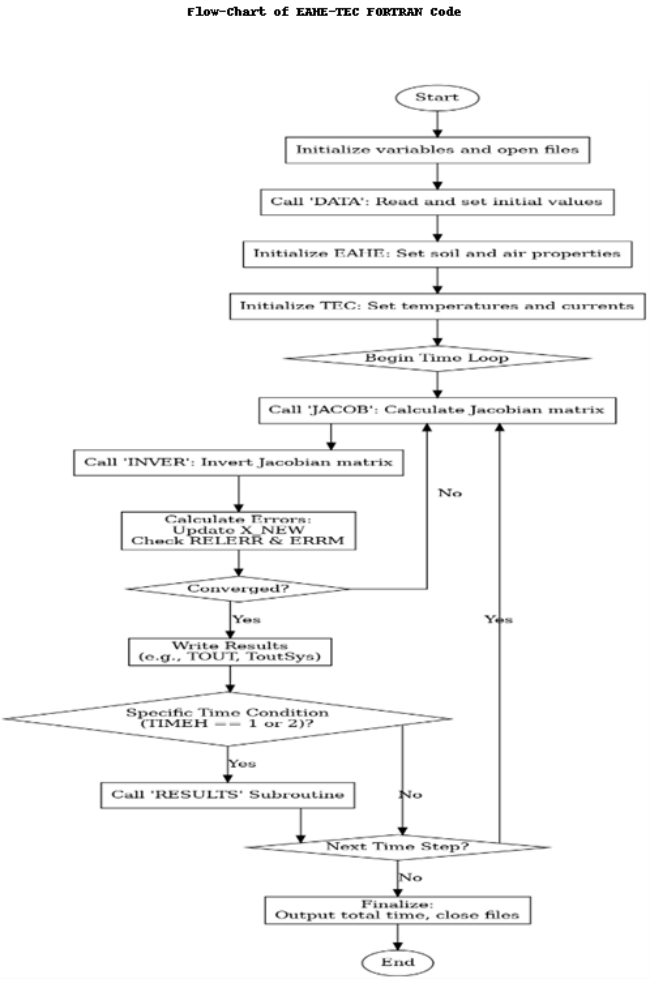

Figure 3.Flow-Chart of EAHE-TEC FORTRAN Code

III. Results and Analysis

The results section presents temperature profiles for 5m, 10m, and 20m system lengths over three-time intervals (1 hour, 2 hours, and 3 hours) with 10 TECs integrated into the setup. These results highlight the system's cooling performance, analyzing axial and radial temperature distributions to evaluate the effectiveness of the EAHE-TEC hybrid system under varying conditions.

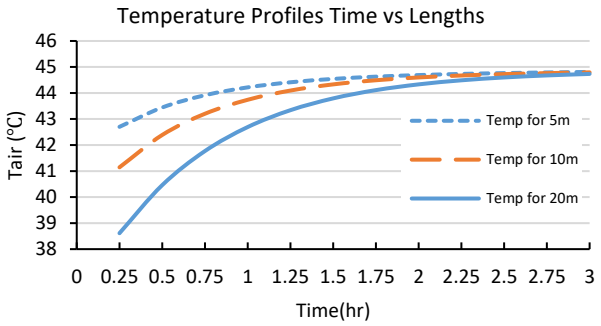

Figure 4. Temperature Profiles for 5m, 10m, and 20m with time

Figure 4 illustrates the temperature profiles for 5m, 10m, and 20m lengths over time. At 15 minutes (0.25 hour), the 20m length exhibits the lowest temperature, around 38.5°C, followed by the 10m length at approximately 41°C, and the

5m length at about 42.8°C. This trend indicates that longer lengths produce lower temperatures initially due to slower heat transfer. After 3 hours, all profiles gradually rise toward 45°C, which is the inlet temperature of the system.

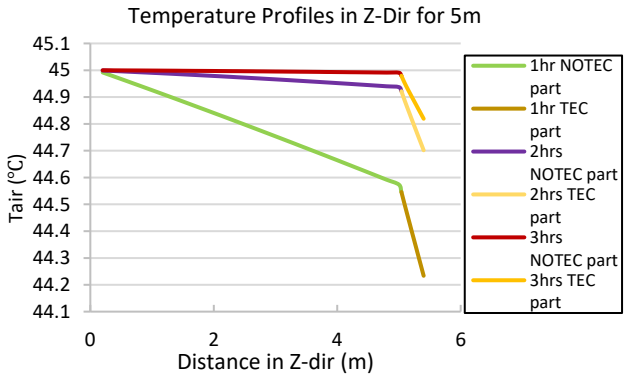

Figure 5. Temperature Profiles in Z-Dir for 5m

Figure 5 displays temperature profiles in the Z-direction for a 5m system, with data shown for 1 hour, 2 hours, and 3 hours' time intervals, comparing sections with and without TECs. At the end of the NOTEC region, the temperature decreases over time, with values around 44.55°C for 1 hour, 44.96°C for 2 hours, and 44.98°C for 3 hours. At the end of the system (TEC region), the temperature for 1 hour is around 44.22°C, 44.7°C for 2 hours, and 44.8°C for 3 hours.

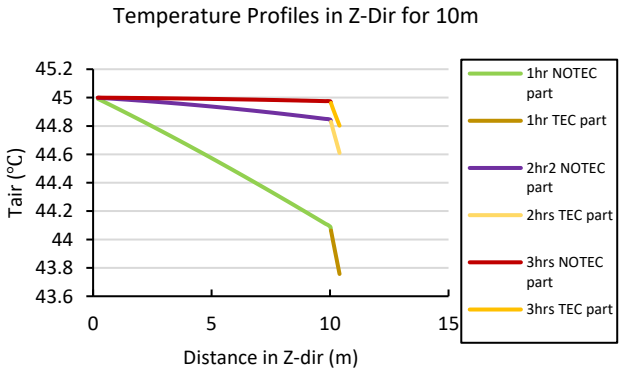

Figure 6. Temperature Profiles in Z-Dir for 10m

Figure 6 presents temperature profiles in the Z-direction for a 10m system, showing data for 1 hour, 2 hours, and 3 hours' time intervals. At the end of the NOTEC region, the temperature decreases over time, with values around 44.1°C for 1 hour, 44.8°C for 2 hours, and 44.97°C for 3 hours. At the end of the system (TEC region), the temperature for 1 hour drops to around 43.7°C, 44.6°C for 2 hours, and 44.79°C for 3 hours.

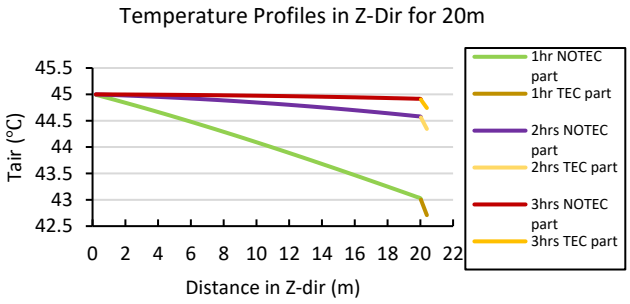

Figure 7. Temperature Profiles in Z-Dir for 20m

Figure 7 illustrates temperature profiles in the Z-direction for a 20m system, showing data for 1 hour, 2 hours, and 3 hours' time intervals, comparing the NOTEC and TEC sections. At the end of the NOTEC region, the temperature decreases with time, showing values of approximately 43.0°C for 1 hour, 44.51°C for 2 hours, and 44.99°C for 3 hours. At the end of the system (TEC region), the temperature for 1 hour drops to around 42.52°C, 44.4°C for 2 hours, and 44.6°C for 3 hours.

From figures 5-7, The temperature profiles across different lengths (5m, 10m, and 20m) show that longer lengths result in lower temperatures in the NOTEC region, 20m shows 43.0°C. Over time, the NOTEC region for all lengths gradually approaches higher temperatures, indicating the influence of the accumulative heat in the soil with time. Similarly, the output temperature of the system for 20m length shows the lowest temperature 42.52°C after 1 hour. However, it increases significantly with time due to the heat cumulative in the soil from the hot-side of TECs.

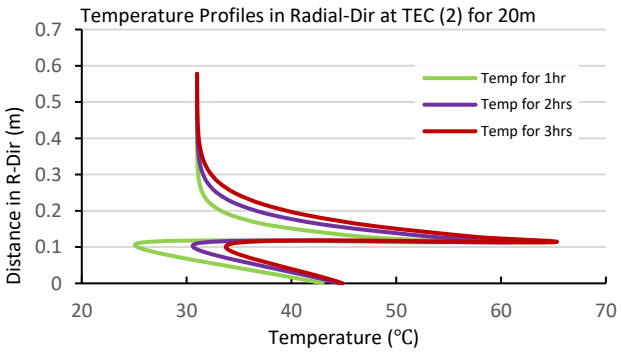

Figure 8. Temperature Profiles in Radial-Dir at TEC (2) for 20m

Figure 8 illustrates the temperature profiles in the radial direction (R-Dir) at TEC number 2 for a 20m system over 1, 2, and 3 hours. At 1 hour, the lowest temperature is approximately 25°C, which is the temperature of the cold side of TEC (TC). Going across TEC, the highest temperature is around 54°C at the hot side of TEC causing the adjusted soil to accumulate heat. Consequently, for 2 hours, TEC efficiency decreases resulting to the lowest temperature increases to about 32°C, while the highest temperature remains at 61.5°C. Similarly, at 3 hours, the lowest temperature rises further to approximately 35°C, with the highest temperature still at 66.5°C.

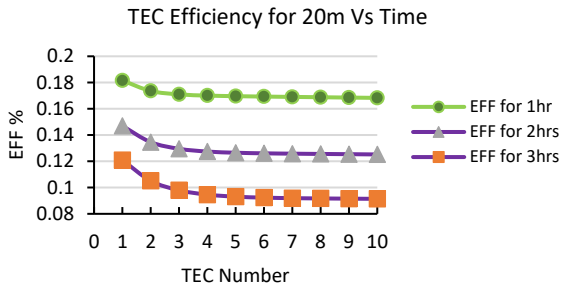

Figure 9. TEC Efficiency for 20m Vs Time

Figure 9 shows TECs efficiency (%) for a 20m system over time intervals of 1 hour, 2 hours, and 3 hours. The maximum efficiency for the 1 hour is approximately 18%, which decreases across all TECs, up to around 17%, while the air is getting colder. For 2 hours, the maximum efficiency decreases to around 14.6%, while for 3 hours, the maximum efficiency further drops to about 12%. The results demonstrate a decline in TEC efficiency, for each length, over time due to cumulative heat buildup in the system.

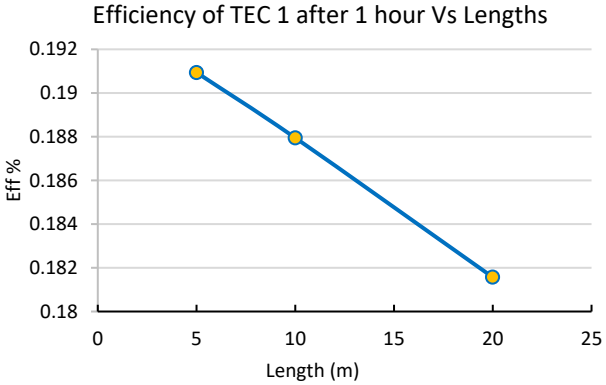

Figure 6. Efficiency of TEC 1 after 1 hour Vs Lengths

Figure 10 Illustrates the efficiency of TEC 1 after 1 hour as a function of system length (5m, 10m, and 20m). For the 5m length, the efficiency is approximately 0.192%, while for the 10m and 20m lengths, it drops to 0.188% and 0.182%, respectively. As a result, the efficiency of TEC decreases as the system length increases. In other words, TEC works better if the air temperature is relatively wormer, which is for 5m in this range of lengths. It also indicates that when the air temperature is relatively colder, 20m, the efficiency of TEC decreases.

IV. Conclusion

This study presents a numerical investigation of a hybrid Earth-to-Air Heat Exchanger (EAHE) system integrated with Thermo-Electric Cooling (TEC) devices for cooling applications in hot climates like Saudi Arabia. The findings highlight the potential of combining shallow geothermal energy with thermoelectric technology to improve air conditioning efficiency, reduce energy consumption, and contribute to sustainability goals outlined in Vision 2030. The results demonstrate the effectiveness of EAHE in utilizing stable subsurface temperatures to cool air through conduction and convection. Longer pipe lengths in the EAHE system (e.g., 20m) exhibited lower initial temperatures due to slower heat transfer. The addition of TECs significantly enhanced cooling performance, particularly in overcoming limitations of the EAHE system in extreme climates. TEC devices were observed to provide efficient cooling in localized regions, ensuring the temperature at the cold side remained low while managing heat dissipation at the hot side. Radial and axial temperature profiles revealed key insights into heat accumulation in the soil and its impact on system performance. Over time, TECs demonstrated reduced efficiency due to cumulative heat in the surrounding sand. However, the system maintained sufficient cooling capacity, indicating that proper soil thermal management is critical for sustained performance. The inclusion of TEC efficiency analysis revealed important insights into the system's performance. For a 20m system, the TEC efficiency declined over time, dropping from 18% after 1 hour to around 12% after 3 hours due to cumulative heat buildup in the soil. This emphasizes the importance of thermal management strategies for sustained performance. Furthermore, the efficiency of TEC 1 was found to decrease with increasing system length, achieving a maximum of 0.192% for a 5m system and dropping to 0.182% for a 20m system. These findings highlight that TECs perform better when the air entering the system is warmer, as seen with shorter pipe lengths, while efficiency declines when air temperatures are colder in longer systems. In conclusion, the integration of TEC with EAHE offers a promising solution for sustainable cooling in arid regions. While TEC devices enhance cooling performance, managing heat accumulation in the soil is critical for long-term efficiency. Future work could focus on optimizing TEC placement, improving soil heat dissipation strategies, and exploring advanced TEC materials with higher thermoelectric performance. This hybrid approach aligns well with Saudi Arabia's goals of reducing energy consumption and environmental impact, offering a pathway to innovative and sustainable HVAC solutions.

V. References

[1] ["Saudi_Vision 2030," Saudi Vision 2030. [Online]. Available: www.vision2030.gov.sa.

[2] M. Lee, "Saudi Vision 2030: What are Saudi Arabia's Plans for the Future?," Earth.Org, 2021. [Online]. Available: www.earth.org.

[3] "The Refrigeration Future in the Kingdom: Technology, Market, and Strategies Options," King Abdullah Petroleum Studies and Research Center (KAPSARC), 2020. [Online]. Available: www.kapsarc.org.

[4] "Geothermal energy," British Geological Survey, 2021. [Online]. Available: www.bgs.ac.uk/geology-projects/geothermal-energy.

[5] N. Touzani and J. E. Jellal, "Study of an air conditioning and heating system incorporating a Canadian well in continental areas, cases of Rabat," in *Proc. Int. Renewable and Sustainable Energy Conf. (IRSEC)*, Apr. 2016, pp. 1–6. doi: 10.1109/IRSEC.2015.7455023.

[6] "Geothermal energy," British Geological Survey. Available: www.bgs.ac.uk/geology-projects/geothermal-energy. Accessed: 2021.

[7] G. Florides and S. Kalogirou, "Annual ground temperature measurements at various depths," Unpublished.

[8] F. Al-Ajmi, D. L. Loveday, and V. I. Hanby, "The cooling potential of earth-air heat exchangers for domestic buildings in a desert climate," *Building and Environment*, vol. 41, no. 3, pp. 235–244, Mar. 2006, doi: 10.1016/j.buildenv.2005.01.027.

[9] C. Peretti, A. Zarrella, M. de Carli, and R. Zecchin, "The design and environmental evaluation of earth-to-air heat exchangers (EAHE). A literature review," *Renewable and Sustainable Energy Reviews*, vol. 28, pp. 107–116, 2013, doi: 10.1016/j.rser.2013.07.057.

[10] N. Bordoloi, A. Sharma, H. Nautiyal, and V. Goel, "An intense review on the latest advancements of Earth Air Heat Exchangers," *Renewable and Sustainable Energy Reviews*, vol. 89, pp. 261–280, Jun. 01, 2018, doi: 10.1016/j.rser.2018.03.056.

[11] Sehli A, Hasni A, Tamali M. The potential of earth-air heat exchangers for low energy cooling of buildings in South Algeria. Energy Procedia 2012;18:496–506. http://dx.doi.org/10.1016/j.egypro.2012.05.061.

[12] Z. Abbas et al., “Performance evaluation of novel solar-powered domestic air cooler with Peltier modules,” *Journal of Mechanical Science and Technology*, vol. 34, no. 11, pp. 4797–4807, Nov. 2020, doi: 10.1007/s12206-020-1036-0.

[13] H. Najafi and K. A. Woodbury, “Optimization of a cooling system based on Peltier effect for photovoltaic cells,” *Solar Energy*, vol. 91, pp. 152–160, May 2013, doi: 10.1016/j.solener.2013.01.026.

[14] H. Y. Zhang, “A general approach in evaluating and optimizing thermoelectric coolers,” *International Journal of Refrigeration*, vol. 33, no. 6, pp. 1187–1196, Sep. 2010, doi: 10.1016/j.ijrefrig.2010.04.007.

[15] [P. K. Bansal and A. Martin, “Comparative study of vapour compression, thermoelectric and absorption refrigerators,” 1999.

[16] C. Peretti, A. Zarrella, M. de Carli, and R. Zecchin, “The design and environmental evaluation of earth-to-air heat exchangers (EAHE). A literature review,” *Renewable and Sustainable Energy Reviews*, vol. 28. pp. 107–116, 2013. doi: 10.1016/j.rser.2013.07.057

[17] S. Hamdane, C. Mahboub, and A. Moummi, "Numerical approach to predict the outlet temperature of earth-to-air-heat-exchanger," *Thermal Science and Engineering Progress*, vol. 21, 100806, 2021, doi: 10.1016/j.tsep.2020.100806.

[18] Z. Luo, "A Simple Method to Estimate the Physical Characteristics of a Thermoelectric Cooler from Vendor Datasheets," *AMS Technologies*, Articles, TECs, Aug. 1, 2008.

[19] M. Metcalf and J. Reid, *Fortran 95/2003 for Scientists & Engineers*, Springer Science & Business Media, 2003.

Smart Maintenance System Using Multilayer LSTM and Statistical Feature Selection for Urban and Industrial Applications

Samia BELDJOUDI
Departement of Industrial Engineering
National Polytechnic School
Algiers, Algeria
Email: samia.beldjoudi@g.enp.edu.dz

Fatima Khadija BENZINE
Laboratory of Innovative Technologies (LTI)
National Higher School of Advanced Technologies
Algiers, Algeria
Email: f_benzine@ensta.edu.dz

Iskander ZOUAGHI
Departement of Industrial Engineering
National Polytechnic School
Algiers, Algeria
Email: iskander.zouaghi@g.enp.edu.dz

Hassina SERIDI
Electronic Document Management Laboratory (LabGED)
Badji Mokhtar University
Annaba, Algeria
Email: seridi@labged.net

Fouad Haouari
Laboratory of Innovative Technologies (LTI)
National Higher School of Advanced Technologies
Algiers, Algeria
Email: fouad.houari@ensta.edu.dz

***Abstract*—Smart cities rely on physical infrastructure to support their operations, utilizing data collected through IoT technologies. The primary goals of smart cities include ensuring sustainable, efficient, and eco-friendly management of resources, while minimizing waste. However, the maintenance of these infrastructures is a critical aspect that is often overlooked, despite its importance in maintaining the longevity and effectiveness of smart city systems.**

We propose a smart and predictive maintenance system based on Remaining Useful Life (RUL) prognosis using a Multilayer Long Short-Term Memory (LSTM) network with a statistical feature selection method. This approach has demonstrated high accuracy and holds promise for further exploration and potential implementation in smart cities to enhance their operational efficiency and sustainability.

Keywords: Maintenance, IoT, LSTM, prognosis, RUL, deep learning

I. Introduction

The concept of smart cities originated from the Internet of Things (IoT) notion [1]. IoT refers to the extension of network connectivity and computing capability to physical objects, enabling them to generate, exchange, and analyze data with minimal human intervention [2]. This data acquisition is often facilitated by sensors. Smart cities leverage the advantages of IoT, particularly data collection and analysis, to enhance the quality of life by improving traditional infrastructure systems within a city, benefiting both residents and businesses [3].

For a city to be considered "smart," it must excel in various categories, such as smart environment, smart economy, smart living, smart mobility, and smart governance [3]. The concept can also extend to smart factories and smart healthcare. Smart city models often emphasize the importance of smart and green energy, incorporating multidimensional decision-making and management processes aimed at maximizing efficiency and minimizing waste and costs [1], [3]. These "smart" aspects are facilitated through various interconnected infrastructures, such as roads, vehicles, energy supply systems, and lighting, which require maintenance to remain efficient and reliable.

The maintenance aspect of smart cities is often overlooked in research reviewing the concept and definition of smart cities, but it is crucial for sustainable urban development. Maintenance strategies in smart cities must also be "smart," incorporating principles from Industry 4.0, which utilizes data collected from equipment to plan maintenance operations efficiently.

In this paper, we propose a predictive maintenance approach, contrasting with traditional maintenance methods that rely on scheduled tasks without a "smart" component. Our approach aims to predict equipment faults before they occur by estimating the remaining useful life (RUL) of systems. This can help smart cities reduce costs and minimize downtime associated with maintenance activities, thereby supporting smart management and smart industry initiatives through improved decision-making processes. Our methodology employs a deep learning approach using a multi-layered Long Short-Term Memory (LSTM) model, a type of Recurrent Neural Network (RNN), combined with a statistical method for selecting predominant features within the system's data. The proposed approach is tested on the C-MAPSS dataset.

The rest of the paper is structured as follows: Section II presents related work, and Section III describes the methodology and model architecture. Section IV discusses the experiments and their results, followed by a discussion in Section V. Finally, Section VI concludes the paper and outlines future work.

II. Related Work

In the field of RUL prediction using deep learning (DL) methods, researchers mainly focus on predicting the RUL of turboreactors, often using the C-MAPSS dataset detailed in Section III. This dataset provides run-to-failure data of

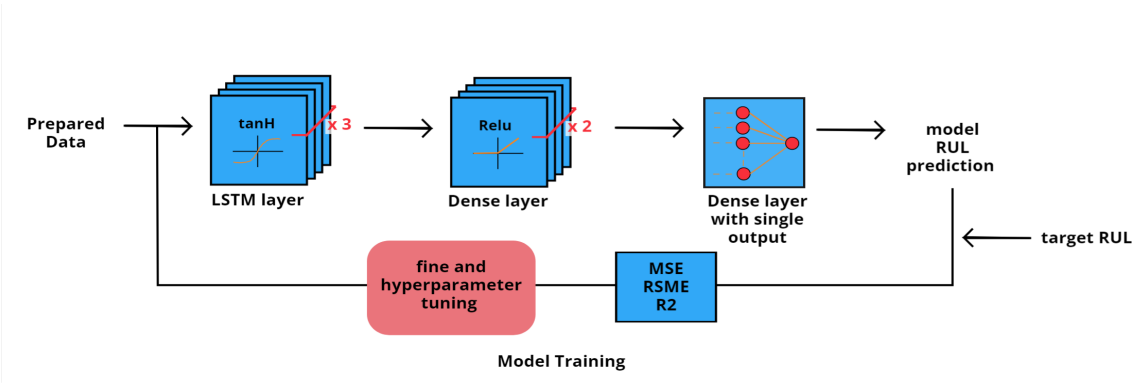

Fig. 1: Architecture of the Proposed LSTM Model for RUL Prediction

similar turboreactors, allowing researchers to compare the efficiency of their models. In this section, we summarize the main methods and research developed to estimate the RUL of aircraft engines with a focus on DL methods. They can be divided into two main categories: model-based methods and data-driven methods [4], [5]. Model-based methods rely on an accurate mathematical model of the mechanical system and its degradation process [6], [7]. These methods can accurately predict when the failure behavior will reach a fault threshold and estimate the RUL of the system. However with the complexity of modern equipment, the mathematical models have become increasingly complex and sometimes fail to accurately capture the system behavior, especially when it is difficult to directly observe degradation tendencies from data observation [8]. This complexity also reduces flexibility when faced with variable and complex fault modes [4]. This limitation motivated the introduction of data-driven methods for the RUL prediction challenge. With less expertise required in system characteristics, they can capture the degradation data collected by the system's sensors [9]. Furthermore, because expertise knowledge of the underlying physics is not required, developers can come up with solutions more quickly [8]. The accuracy of the prediction relies on the quality of the data-driven model developed. Initially, shallow algorithms such as Artificial Neural Networks (ANNs) [10], Support Vector Machines (SVMs) [11], Random Forest algorithms (RFs) [12], and Hidden Markov Models (HMMs) [13] were used to solve the RUL prediction problem. However, these methods were soon surpassed due to the complexity of the multivariate sensor data, which is often corrupted with noise. Thus, DL algorithms were introduced for the RUL prognosis task. Convolutional Neural Networks (CNNs), often used for video and image processing due to their capacity to learn features from spatial dimensions through parameter sharing, pooling, and filter operations, were adapted for the RUL prognosis task, but are prone to losing key information in sequential data [4]. Due to their ability to handle and contextualize sequential data, Recurrent Neural Networks (RNNs) were used for this task [14]. They utilize memory and feedback to learn complex non-linear dynamic mappings [8]. However, RNNs fail to capture long-term dependencies in sequential data, which is crucial for accurate RUL prognosis. To overcome this problem, Long Short-Term Memory (LSTM) networks were introduced and used in the RUL prognosis task [15]. However, classical LSTM models tend to focus on learning information from data introduced later in the sequence, which might be problematic if crucial information about the system behavior is found earlier in the sequence. This is crucial for the estimation of the RUL. We propose a multilayered LSTM architecture to avoid this limitation. Moreover, traditional LSTM models use the same updating method for all inputs, i.e., they do not discriminate between important recurrent data and less relevant data [5]. To address this limitation, effective feature selection can be performed to identify the best health indicators of the system, as proposed in this paper, or reliance on the transformer model, introduced in [16], which can effectively contextualize sequential data and perform various tasks through an encoder-decoder architecture and an attention mechanism. It is the latest trend in the RUL prognosis field . Recent advancements in predictive maintenance for smart city applications highlight the advantages of hybrid deep learning models. Combining CNNs and LSTM networks has shown to improve RUL predictions by capturing both spatial and temporal dependencies, allowing for more accurate and nuanced forecasting in multivariate time series data [17], [18]. However, it is important to note that combining models also means combining their disadvantages, often resulting in high computational complexity, increased training time, and a lack of interpretability, which are other research gaps in the RUL prognosis field [4]. Recent studies [19] emphasize the efficiency of data mining techniques, such as association rules, in forecasting the Remaining Useful Life (RUL) of industrial equipment. Integrating these methods into CMMS software with NASA datasets significantly improves predictive maintenance capabilities.

The main limitations in existing methods addressed by our model models are as follow :

- Intricate and non-linear mathematical structures struggle to demonstrate generalization when applied to related yet diverse small datasets with high variability [20].
- Traditional models, such as Artificial Neural Networks

(ANNs) fail to extract complex sequential features from data, which limits their ability to accurately learn specific information necessary for aircraft anomaly prediction [7], [4].

The primary contribution of this paper is the development of a multi-layer LSTM algorithm for predicting the Remaining Useful Life (RUL) of systems. This model is designed to effectively capture significant sequential patterns inherent in multivariate time series data, as exemplified by the NASA C-MAPSS dataset. The choice of LSTM is motivated by its proven success in handling time-dependent data. Furthermore, to prevent overfitting and enhance the model's learning capabilities, a statistical feature selection method is incorporated. This approach not only reduces the dimensionality of the problem but also simplifies computational requirements. The detailed steps and architecture of the model are elaborated in Section III.

III. Methodology

Before introducing our proposed model and demonstrating how it can overcome the limitations mentioned earlier, it is important to further describe the LSTM architecture. An LSTM unit consists of a cell, an input gate, an output gate, and a forget gate. The architecture includes a recurrence system where the output of an LSTM cell is fed back into the cell as input along with new data. This allows the model to create context within sequences by incorporating knowledge of previous events. First, the block input combines the current input and the previous output:

$$z^{(t)} = g(W_z x^{(t)} + R_z y^{(t-1)} + b_z) \tag{1}$$

where W_z and R_z are the weights for $x^{(t)}$ and $y^{(t-1)}$, respectively, and b_z is the bias vector.

In the input gate, the current input $x^{(t)}$, last output $y^{(t-1)}$, and previous cell state $c^{(t-1)}$ are combined:

$$i^{(t)} = \sigma(W_i x^{(t)} + R_i y^{(t-1)} + p_i \odot c^{(t-1)} + b_i) \tag{2}$$

where W_i, R_i, and p_i are the weights for $x^{(t)}$, $y^{(t-1)}$, and $c^{(t-1)}$, and b_i is the bias.

The forget gate then decides which information from prior cell states to retain:

$$f^{(t)} = \sigma(W_f x^{(t)} + R_f y^{(t-1)} + p_f \odot c^{(t-1)} + b_f) \tag{3}$$

where W_f, R_f, and p_f correspond to the weights for $x^{(t)}$, $y^{(t-1)}$, and $c^{(t-1)}$, with b_f as the bias.

The cell state update combines the block input $z^{(t)}$, input gate $i^{(t)}$, and forget gate $f^{(t)}$:

$$c^{(t)} = z^{(t)} \odot i^{(t)} + c^{(t-1)} \odot f^{(t)} \tag{4}$$

The output gate then combines $c^{(t)}$, $x^{(t)}$, and $y^{(t-1)}$:

$$o^{(t)} = \sigma(W_o x^{(t)} + R_o y^{(t-1)} + p_o \odot c^{(t)} + b_o) \tag{5}$$

Finally, the output of the LSTM unit is:

$$y^{(t)} = g(c^{(t)}) \odot o^{(t)} \tag{6}$$

In these equations, σ, g, and h denote activation functions, specifically the sigmoid function for σ and the hyperbolic tangent for g and h. [21].

As illustrated in Figure 1, the LSTM model architecture includes three stacked LSTM layers following by two dense layers and a final dense layer with a single output neuron. The details of each layer are specified in Table I. The objective is to leverage the LSTM unit's ability to contextualize and memorize information within sequential data, using mechanisms described earlier. By stacking multiple LSTM layers, the model can represent and contextualize sequences with greater complexity, effectively capturing intricate and dependent time patterns within sequential data, thus avoiding the limitation of failing to extract complex sequential features. This contextual information is then passed to the dense layers, which perform the regression task of predicting the Remaining Useful Life (RUL).

Before training the model, we perform data preparation through feature selection. Feature selection significantly enhances a model's ability to make accurate predictions by reducing overfitting and eliminating redundant data, especially given the increased complexity from stacking LSTM layers [22]. In this paper, we utilize descriptive statistical methods for feature selection, focusing on measures of dispersion and the correlation matrix. This approach has proven effective, as demonstrated in [22]. Details of this procedure will be further elaborated upon in the dataset presentation in Section IV.

TABLE I: Model Architecture Details

Layers	Parameters
LSTM	Neurons: 128, 64, 32 Activation: tanH
Dense	Neurons: 96, 128 Activation: ReLU
Dense (Output)	Single output unit

IV. Experiments

In this section, we introduce in detail the dataset used to train, test, and evaluate the proposed model, along with the related experimental settings.

A. Datasets

In this paper, we use the Commercial Modular Aero-Propulsion System Simulation (C-MAPSS) dataset, as many other researchers on RUL prognosis do, provided by the Prognostics Center of Excellence at Ames Research Center [23]. It consists of a simulation model of the degradation state of turboreactors. This database is divided into four parts according to distinct simulation parameters.

Regarding the nature of the database, the C-MAPSS consists of a variety of multivariate time series of different reactors. Each data group is further divided into sub-databases for training and testing. At the start of each time series, the reactor is in its normal operational state and then switches to the failure state at a given time. More specifically, in the

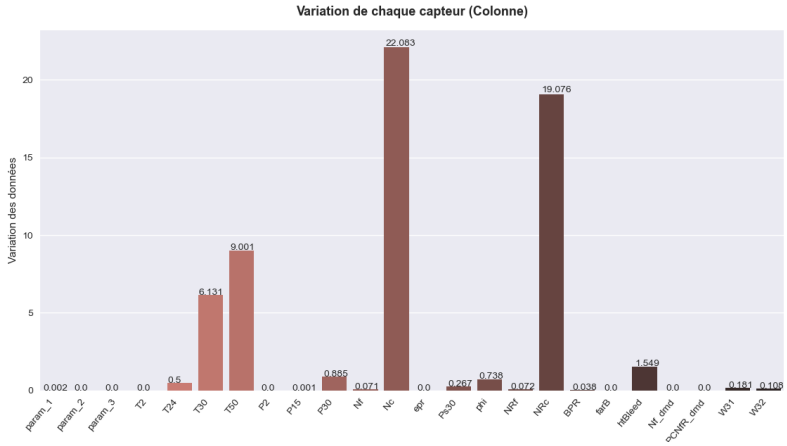

Fig. 2: Standard deviation for each reactor.

training database, the simulation model generates increasing errors until the reactor reaches the failure state. For testing purposes, in the test database, the time series stop before reaching the failure state [24]. In this paper, we use only the first of the four main datasets: the FD001 dataset.

The training dataset consists of 26 columns and 20,631 rows. Each row corresponds to data from a functioning cycle of a specific turboreactor. The first two columns indicate the turbine ID and the cycle number. The next three columns represent how three operational settings affect the turbine's behavior. The remaining 21 columns contain data collected from 21 sensors installed on the turbo engine.

To better understand the data, we apply descriptive statistics to the FD001 dataset, obtaining the results shown in Table II. The statistics regarding the IDs are not as exact as expected (i.e., mean value = 50, first quartile = 25, median value = 50, third quartile = 75), indicating that the number of cycles for each ID is not consistent. Thus, the maximum number of cycles a reactor can reach before its failure state may differ from one to another. These statistics also highlight that the maximum number of cycles reached by a reactor is 362 cycles. The turbo cycle column also indicates the remaining useful life (RUL) of a specific reactor ID because it indicates the maximum number of cycles it can reach before failure. For example, the reactor with ID 1 has its turbo cycle progressively increasing until it reaches the maximum of 192. Given this information, it is possible for each reactor ID to add a column specifying its RUL by subtracting the current cycle count from the maximum turbo cycle.

We further analyzed the dataset by studying correlations between features, thereby highlighting the predominant ones that influence the behavior of the reactors. It is important to specify that by features we refer only to the three main settings and the 21 sensors—not the turbo ID and turbo cycles. We first evaluated the standard deviation of each feature, as shown in Figure 2. We noticed that 8 features (setting 2, setting 3, T2, P2, Epr, Farb, NFdmd, PCNfrdmd) have a null standard deviation. This indicates that they do not vary much from the

TABLE II: Overview of Data Distribution Through Descriptive Statistics

	Turbo ID	**Turbo Cycle**	...	**W31**	**W32**
Count	20631	20631	...	20631	20631
Mean	51.51	108.81	...	38.82	23.29
Standard Deviation	29.23	68.88	...	0.18	0.11
Minimum	1	1	...	38.14	22.89
1st Quartile (25%)	26.00	52.00	...	38.70	23.22
Median (50%)	52.00	104.00	...	38.83	23.30
3rd Quartile (75%)	77.00	156.00	...	38.95	23.37
Maximum	100.00	362.00	...	39.43	23.62

mean value and thus do not change from one reactor to another or even from one cycle to another. In other words, they do not influence the behavior of the reactor and its RUL; it is better not to consider them in the analysis and training of our model.

Three other features (setting 1,P15, P30), have a nearly null standard deviation. As with the preceding ones, it is better not to include them in our model. The four major features (T30, T50, NC, and NRc) have a high standard deviation and thus may indicate a significant influence on the reactors' behavior, making them important to consider—especially NC, which has the highest standard deviation of 22,083.

Finally, before feeding the data to our model, it is necessary to normalize them so that the scale of one feature does not disproportionately influence the model's learning. This ensures a uniform contribution from every feature. We use the Min-Max method as shown in the following equation:

$$X_{norm}^{i,j} = \frac{2X^{i,j} - X_{min}^{i,j}}{X_{max}^{j} - X_{min}^{j}} - 1, \forall i, j \tag{7}$$

where,

$X_{norm}^{i,j}$: normalized value

$X^{i,j}$: i-th point of the original data

X_{max}^{j}, X_{min}^{j} : maximal and minimum values of collected data.

B. Evaluation Metrics

We selected several evaluation metrics to assess the performance of our model, enabling it to improve its accuracy through training and allowing us to compare our approach with existing literature using the test dataset. Specifically, we chose the Root Mean Squared Error (RMSE) and Mean Squared Error (MSE) to measure the magnitude of the error between actual and predicted values. Additionally, we used the coefficient of determination R^2 to evaluate the quality of the regression model. We also employed a Score value to assess the performance of the model, comparing actual and predicted values using normalized RUL.

C. Hyperparameters

We tested various hyperparameter combinations to identify the most effective for accurate predictions. This included two optimizers (Adam and RMSprop) and time windows of 28 and 30 cycles, with training conducted over 10 epochs and an initial learning rate of 0.001. The results, shown in Table III, indicated that the best combination was the Adam optimizer with a 28-cycle time window, yielding the lowest root mean square error (RMSE) of 14.32 and an S-score of 325.05, reflecting strong predictive performance. This combination also achieved the highest R^2 value of 0.8812, explaining 88.12% of the variance in the target data. The optimizer choice had a more significant impact on performance than the time window; Adam consistently outperformed RMSprop in terms of RMSE. Notably, RMSprop was more sensitive to the time window, showing a lower RMSE at 28 cycles, while Adam maintained the same RMSE for both time window lengths.

TABLE III: Results of the RUL prediction for different parameters

		Metrics			
Time window length	Optimizer	MSE	RMSE	S-score	R^2
30	Adam	86.3497	**14.321053**	**325.04655**	**0.8812344**
30	RMSprop	136.276	15.982364	473.73554	0.8520814
28	Adam	86.3497	**14.321053**	**325.04655**	**0.8812344**
28	RMSprop	**71.6309**	16.506661	471.63627	0.8422174

V. Results and Discussion

Given the architectural model and the optimal parameters chosen, the final results obtained through the proposed LSTM network are presented in Fig. 3. From this figure, it is evident that the two curves are extremely close, indicating that the model's predictions closely match the actual RUL values. Finally, a precision score was computed for our model, reaching a value of 86.0% for training, meaning that the model accurately estimated 86.0% of the training set.

Additionally, a comparison with previous models is presented in Table IV. It is clear that the modifications proposed in this paper significantly enhance performance, particularly in comparison to "classical" models, especially regarding simple LSTM models for the C-MAPSS FD001 dataset. However, it is important to note that more complex and hybrid methods using deep CNN and LSTM architectures demonstrate greater performance, as referenced in [25], [26].

A trade-off exists between achieving high accuracy with more complex models and maintaining moderate accuracy with simpler, less time-consuming models, particularly for later industrial applications. The proposed method can be viewed as a balanced approach.

TABLE IV: Comparison of RMSE and Score for FD001 based on C-MAPSS dataset

Method	**FD001 (RMSE)**	**Score**
MLP [27]	37.56	980.23
SVR [27]	29.40	743.35
RVR [27]	23.80	682.41
CNN [27]	18.45	650.80
MODBNE [28]	15.04	403.92
LSTM [15]	16.14	397.75
Proposed Method	**14.32**	**325.05**
Improved Ratio	**11.28%**	**18.28%**

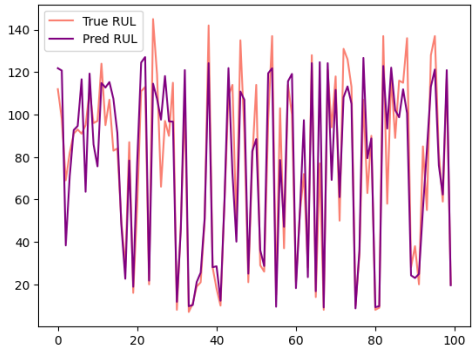

Fig. 3: Similarity between predicted RUL and real RUL

VI. Conclusion

This paper highlights the need for a smart maintenance system in smart cities to support smart governance, decision-making, and smart industries. Such a system aims to minimize waste, downtime, repairs, and operational costs while ensuring reliability and durability. We propose utilizing Industry 4.0 approaches and a smart predictive maintenance system through Remaining Useful Life (RUL) prognosis. The Long Short-Term Memory (LSTM) network is favored, based on a review of related work. Addressing the limitations of existing models, which often struggle with generalization and extracting complex sequential features, we introduce a multi-layer LSTM network with a statistical feature selection method for RUL prognosis. The model is tested on the FD001 subset of the C-MAPSS dataset, demonstrating high accuracy. Future work should explore scalability for large-scale deployments in predictive maintenance systems within urban settings. Edge computing offers a practical solution by enabling decentralized data processing closer to IoT sensors, minimizinglatency and enhancing real-time processing for extensive city infrastructures [29], [30], [31]. This scalability would make

the proposed system adaptable for large smart cities with diverse assets. Additionally, enhancing the explainability of maintenance models could boost stakeholder trust, as clear insights into model decisions are essential for maintenance teams and planners. Methods like SHAP (Shapley Additive Explanations) can reveal the most influential features in RUL predictions, supporting transparency in decision-making [32], [33]. Implementing such interpretable frameworks would make predictive models more actionable and reliable across smart city applications.

REFERENCES

[1] B. N. Silva, M. Khan, and K. Han, "Towards sustainable smart cities: A review of trends, architectures, components, and open challenges in smart cities," vol. 38, pp. 697–713. [Online]. Available: https://linkinghub.elsevier.com/retrieve/pii/S2210670717311125

[2] K. Rose, S. Eldridge, and L. Chapin, "The internet of things: An overview," *The internet society (ISOC)*, vol. 80, no. 15, pp. 1–53, 2015.

[3] R. Yang and F. Zhen, "Smart city development models: A cross-cultural regional analysis from theory to practice," vol. 8, p. 100221. [Online]. Available: https://linkinghub.elsevier.com/retrieve/pii/S2590051X24000303

[4] Z. Shang, Z. Feng, W. Li, Z. Wu, and H. Cheng, "Capsule network based on double-layer attention mechanism and multi-scale feature extraction for remaining life prediction," vol. 56, no. 3, p. 195. [Online]. Available: https://doi.org/10.1007/s11063-024-11651-8

[5] R. Bai, K. Noman, Y. Yang, Y. Li, and W. Guo, "Towards trustworthy remaining useful life prediction through multi-source information fusion and a novel LSTM-DAU model," vol. 245, p. 110047. [Online]. Available: https://linkinghub.elsevier.com/retrieve/pii/S0951832024001224

[6] C. Ferreira and G. Gonçalves, "Remaining useful life prediction and challenges: A literature review on the use of machine learning methods," *Journal of Manufacturing Systems*, vol. 63, pp. 550–562, 2022. [Online]. Available: https://www.sciencedirect.com/science/article/pii/S0278612522000796

[7] Y. LeCun, Y. Bengio, and G. Hinton, "Deep learning," *nature*, vol. 521, no. 7553, pp. 436–444, 2015.

[8] F. O. Heimes, "Recurrent neural networks for remaining useful life estimation," in *2008 International Conference on Prognostics and Health Management*. IEEE, pp. 1–6. [Online]. Available: http://ieeexplore.ieee.org/document/4711422/

[9] H. Tran, S. Khatir, T. Le-Xuan, G. De Roeck, T. Bui Tien, and M. Abdel Wahab, "A novel machine-learning based on the global search techniques using vectorized data for damage detection in structures," *International Journal of Engineering Science*, vol. 157, 09 2020.

[10] S. Khatir, D. Boutchicha, C. Le Thanh, H. Tran-Ngoc, T. Nguyen, and M. Abdel-Wahab, "Improved ann technique combined with jaya algorithm for crack identification in plates using xiga and experimental analysis," *Theoretical and Applied Fracture Mechanics*, vol. 107, p. 102554, 2020. [Online]. Available: https://www.sciencedirect.com/science/article/pii/S0167844220300318

[11] V. T. Tran, H. Thom Pham, B.-S. Yang, and T. Tien Nguyen, "Machine performance degradation assessment and remaining useful life prediction using proportional hazard model and support vector machine," *Mechanical Systems and Signal Processing*, vol. 32, pp. 320–330, 2012, uncertainties in Structural Dynamics. [Online]. Available: https://www.sciencedirect.com/science/article/pii/S0888327012000751

[12] C. Zhang, P. Lim, A. K. Qin, and K. C. Tan, "Multiobjective deep belief networks ensemble for remaining useful life estimation in prognostics," *IEEE Transactions on Neural Networks and Learning Systems*, vol. 28, no. 10, pp. 2306–2318, 2017.

[13] M. Dong and D. He, "A segmental hidden semi-markov model (hsmm)-based diagnostics and prognostics framework and methodology," *Mechanical Systems and Signal Processing*, vol. 21, pp. 2248–2266, 07 2007.

[14] A. Malhi, R. Yan, and R. Gao, "Prognosis of defect propagation based on recurrent neural networks," *IEEE T. Instrumentation and Measurement*, vol. 60, pp. 703–711, 03 2011.

[15] M. Yuan, Y. Wu, and L. Lin, "Fault diagnosis and remaining useful life estimation of aero engine using lstm neural network," 10 2016, pp. 135–140.

[16] A. Vaswani, N. Shazeer, N. Parmar, J. Uszkoreit, L. Jones, A. N. Gomez, L. Kaiser, and I. Polosukhin, "Attention is all you need," 2023. [Online]. Available: https://arxiv.org/abs/1706.03762

[17] A. Wahid, J. G. Breslin, and M. A. Intizar, "Prediction of machine failure in industry 4.0: A hybrid cnn-lstm framework," *Applied Sciences*, vol. 12, no. 9, 2022. [Online]. Available: https://www.mdpi.com/2076-3417/12/9/4221

[18] N. Kashpruk, C. Piskor-Ignatowicz, and J. Baranowski, "Time series prediction in industry 4.0: A comprehensive review and prospects for future advancements," *Applied Sciences*, vol. 13, no. 22, 2023. [Online]. Available: https://www.mdpi.com/2076-3417/13/22/12374

[19] S. Beldjoudi, "Improving existing cmms software packages using association rules," *Revue d'Intelligence Artificielle*, vol. 37, 2023.

[20] M. M. Bejani and M. Ghatee, "A systematic review on overfitting control in shallow and deep neural networks," *Artificial Intelligence Review*, vol. 54, no. 8, pp. 6391–6438, 2021.

[21] Z. Fan, W. Li, and K.-C. Chang, "A bidirectional long short-term memory autoencoder transformer for remaining useful life estimation," *Mathematics*, vol. 11, p. 4972, 12 2023.

[22] W. R. Khattak, A. Salman, S. Ghafoor, and S. Latif, "Multi-modal LSTM network for anomaly prediction in piston engine aircraft," vol. 10, no. 3, p. e25120. [Online]. Available: https://www.sciencedirect.com/science/article/pii/S2405844024011514

[23] A. "Saxena, K. Goebel, D. Simon, and N. Eklund, "Damage propagation modeling for aircraft engine run-to-failure simulation," in *2008 International Conference on Prognostics and Health Management*, 2008, pp. 1–9.

[24] A. Saxena, K. Goebel, D. Simon, and N. Eklund, "Damage propagation modeling for aircraft engine run-to-failure simulation," in *2008 international conference on prognostics and health management*. IEEE, 2008, pp. 1–9.

[25] S. Zheng, K. Ristovski, A. Farahat, and C. Gupta, "Long short-term memory network for remaining useful life estimation," 06 2017, pp. 88–95.

[26] X. Li, Q. Ding, and J.-Q. Sun, "Remaining useful life estimation in prognostics using deep convolution neural networks," *Reliability Engineering System Safety*, vol. 172, pp. 1–11, 2018. [Online]. Available: https://www.sciencedirect.com/science/article/pii/S0951832017307779

[27] G. Babu, P. Zhao, and X. li, "Deep convolutional neural network based regression approach for estimation of remaining useful life," 03 2016, pp. 214–228.

[28] C. Zhang, L. Pin, A. Qin, and K. Tan, "Multiobjective deep belief networks ensemble for remaining useful life estimation in prognostics," *IEEE Transactions on Neural Networks and Learning Systems*, vol. PP, pp. 1–13, 07 2016.

[29] T. Hafeez, L. Xu, and G. McArdle, "Edge intelligence for data handling and predictive maintenance in iiot," *IEEE Access*, vol. PP, pp. 1–1, 03 2021.

[30] Z. Lyu, D. Chen, L. Ranran, and Q. Wang, "Intelligent edge computing based on machine learning for smart city," *Future Generation Computer Systems*, vol. 115, pp. 90–99, 02 2021.

[31] V. Barbuto, C. Savaglio, M. Chen, and G. Fortino, "Disclosing edge intelligence: A systematic meta-survey," *Big Data and Cognitive Computing*, vol. 7, p. 44, 03 2023.

[32] K. Kobayashi and S. B. Alam, "Explainable, interpretable, and trustworthy ai for an intelligent digital twin: A case study on remaining useful life," *Engineering Applications of Artificial Intelligence*, vol. 129, p. 107620, Mar. 2024. [Online]. Available: http://dx.doi.org/10.1016/j.engappai.2023.107620

[33] J. Cohen, X. Huan, and J. Ni, "Shapley-based explainable ai for clustering applications in fault diagnosis and prognosis," 2023. [Online]. Available: https://arxiv.org/abs/2303.14581

PIV-Based Investigation of Airflow Dynamics in a Bottom-Heated Tunnel Greenhouse

Nawel Khaldi
Thermal Process Laboratory
Research and Technology Centre of Energy, Borj-Cedria Science and Technology Park
Nabeul, Tunisia
khaldi.nawel@yahoo.fr
nawel.khaldi@crten.mesrs.tn

Hela Ben Amara
Thermal Process Laboratory
Research and Technology Centre of Energy, Borj-Cedria Science and Technology Park
Nabeul, Tunisia

Hicham Fatnassi
Institut Sophia Agrobiotech - INRAE
Sophia Antipolis, France

Mariem Lazaar
Thermal Process Laboratory
Research and Technology Centre of Energy, Borj-Cedria Science and Technology Park
Nabeul, Tunisia

***Abstract*— This study investigates airflow dynamics within a tunnel greenhouse equipped with a heated base using Particle Image Velocimetry (PIV). A reduced-scale model was designed with cylindrical obstacles simulating vegetation, and a base heated through a copper coil heat exchanger. Airflow patterns were analyzed under both heated and unheated conditions to assess the effects of temperature gradient on the circulation and convective flow within the greenhouse. This experimental setup facilitated the direct visualization of recirculation zones, velocity variations, and the influence of thermal buoyancy forces on air movement, providing insight into how a heated base can modify the microclimate distribution.**

The results indicate that heating the base significantly alters the airflow behavior, introducing a secondary convective cell near the central obstacle and amplifying vertical motion due to buoyancy forces. These findings demonstrate that a heated base, when integrated with a tunnel greenhouse structure, can provide improved thermal and airflow regulation, which may contribute to more effective environmental control strategies in agricultural settings.

Keywords*— *Tunnel greenhouse, Greenhouse airflow dynamics, Thermal gradient influence, PIV, Convective flow behavior.

I. INTRODUCTION

Greenhouse heating is crucial for maintaining optimal growing conditions, especially during nighttime and/or winter months. Traditional heating methods often suffer from energy inefficiency and uneven temperature distribution. In recent years, there has been growing interest in innovative heating strategies, such as those utilizing latent heat storage, geothermal energy, and solar energy. These approaches offer potential for energy savings and improved crop yields.

Latent heat storage systems, in particular, have shown considerable promise in greenhouse heating applications due to their ability to store and release large amounts of thermal energy. For instance, Bouadila et al. [1,2] analyzed a solar air heater collector filled with spherical capsules containing a phase change material (PCM), which achieved 31% of nighttime heating needs through latent heat recovery. Similarly, Benli et al. [3] investigated PCM-based systems integrated with new solar collectors, finding them highly effective for greenhouse heating. Berroug et al. [4] examined the use of a PCM-based north wall in greenhouses, while Lazaar et al. [5] evaluated a polypropylene heat exchanger incorporating calcium chloride hexahydrate for heating tunnel greenhouses in Tunisia, effectively enhancing soil and air temperature regulation.

Additionally, underground air circulation systems have proven effective for heating greenhouses. Ozgener et al. [6,7] evaluated a subterranean heating method using galvanized pipes buried 3 meters underground, which successfully maintained an air temperature of 13.1°C with a heat extraction rate of 3.77 kW. Studies by Lazaar et al. [8-10] further demonstrated that water circulated through capillary heat exchangers embedded in the ground provided effective heat storage and release, facilitating stable temperatures within the greenhouse. Hazami et al. [11] examined the potential of solar heat storage accumulators for greenhouse heating, showing that these systems are effective in mitigating temperature fluctuations. Geothermal energy has also been considered as sustainable solution, with several studies highlighting its reliability as a long-term source of heat for greenhouses [12-14].

Modern greenhouse climate management increasingly relies on advanced numerical models to simulate the dynamic interplay of heating, ventilation, and transpiration. Mahdavi et al. [15] developed a model integrating photovoltaic/thermal (PV/T) collectors with an air-soil heat exchanger. Their validated simulations demonstrated that while PV/Ts alone provided limited heating, integrating them with an air-soil exchanger raised greenhouse air temperatures by 9°C in winter and lowered them by 8°C in summer. Tahery et al. [16] proposed a dynamic model to monitor greenhouse air temperature, humidity, and CO_2 levels while accounting for crop transpiration. Applied to an Iranian greenhouse equipped with a soil-air heat transfer system, the model demonstrated a 17-49% reduction in water use under varying climatic conditions, significantly improving cooling efficiency. Banakar et al. [17] used Transys software to compare conventional, semi-closed, and fully closed greenhouse types, revealing that closed greenhouses reduced heating demands by nearly half, though they required three times the cooling load of conventional designs.

Numerical simulations have become invaluable tools in managing and understanding the indoor climate of greenhouses, offering insights into complex microclimatic interactions and enabling low-cost assessments of different climate control scenarios. However, these simulations are only as accurate as the data on which they are based, making high-quality experimental measurements essential for ensuring reliability and precision [18-20].

To obtain this essential data, non-intrusive experimental methods, particularly Particle Image Velocimetry (PIV), play a crucial role. PIV, combined with laser sheet visualization, enables the accurate visualization and quantification of airflow patterns without disturbing the natural circulation within the greenhouse [21-23]. Mapping microclimatic variables, such as airflow patterns, remains challenging due to the extensive sensor networks typically required to capture temperature, humidity, and velocity fields. Addressing this need, Boulard et al. [24] and Lee et al. [25] applied PIV and flow visualization to measure air velocity and flow patterns in multi-span greenhouses. Their work was further complemented by thermocouple grids for detailed temperature mapping. Okushima et al. [26] and Molina-Aiz et al. [27] expanded this research by using hot-wire anemometers and smoke tracing to map airflow in greenhouses with different ventilation strategies. The precise data generated by these non-intrusive methods not only advances our understanding of greenhouse climate dynamics but also directly supports the refinement of numerical models. Together, experimental and numerical approaches enable a comprehensive approach to greenhouse climate management, helping to optimize design and improve climate control efficiency [28-31].

In this study, we investigate the effects of heating on airflow patterns within a tunnel greenhouse. Using Particle Image Velocimetry (PIV), we will characterize air velocity and temperature distributions under different heating scenarios. By gaining a deeper understanding of these factors, we aim to optimize greenhouse energy efficiency and crop productivity.

II. Experimental Study

A. Experimental Greenhouse

Experiments were conducted within a scaled-down model of a tunnel greenhouse (Fig. 1), measuring 1 m in length, 0.4 m in height, and 0.54 m in width. The greenhouse was equipped with inlet and outlet supply slots, each 0.15 m high, spanning the entire width. A 3 mm thick plexiglass roof provided optical access for Particle Image Velocimetry (PIV) measurements. The base was constructed from a thin, black-painted aluminum plate to minimize light reflections during laser-based visualization.

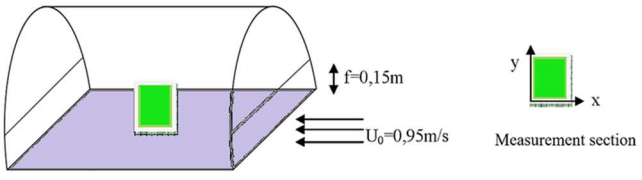

Fig. 1. Geometric configuration of the tunnel greenhouse.

The greenhouse model was positioned within the test section of a wind tunnel. Air was supplied through the inlet slot at a velocity of 0.95 m/s.

To exploit symmetry and mitigate boundary effects in the greenhouse, the laser beam was introduced into a vertical mid-plane (XY). For this study, the measurement plane (XY) was fixed at x = 0.5 m and y = 0.1 m.

B. Two-Dimensional Particle Image Velocimetry

Particle Image Velocimetry (PIV) has emerged as a powerful tool for investigating flow fields in various engineering applications, including agricultural structures. By capturing and analyzing sequential images of tracer particles illuminated by a laser sheet, PIV enables precise measurement of instantaneous velocity fields. This non-intrusive technique is particularly well-suited for studying complex flow patterns within greenhouses, as it allows for detailed visualization and quantification of airflow characteristics.

In our study, PIV was employed to measure the velocity field within a reduced-scale model of a tunnel greenhouse. To ensure accurate measurements, a suitable seeding technique was employed. Figure 2 illustrates a schematic layout of a 2D PIV system. First, the flow facility is seeded with tracer particles, which are illuminated by a pulsed light source (typically a laser) formed into a thin light sheet. A camera positioned perpendicular to this sheet captures sequential and global images of the illuminated particles within the flow field. Electronic equipment synchronizes the timing between the laser pulses and the camera frame rate. A data acquisition system then records these sequential images.

Particle displacements within the flow are determined by applying a cross-correlation algorithm to the captured images, which are subsequently converted from pixel coordinates to physical space through calibration. These particle displacements are then divided by the time interval between laser pulses, producing the velocity field (velocity = displacement/Δt).

III. Results and Discussion

To analyze air circulation and assess the influence of temperature gradients within the greenhouse, we first examined the air velocity field obtained from PIV experiments conducted in a reduced-scale greenhouse model. Results for heated and unheated greenhouse conditions are then presented and compared.

A. Airflow Characterization Inside the Unheated Greenhouse

To simulate vegetation within the greenhouse, cylindrical obstacles were positioned along its mid-plane. Each obstacle has a circular base with a cross-sectional area of $9.62\ 10^{-4}$ m² and a height of h = 0.10 m. To minimize light reflections during laser visualization, the entire surface of each obstacle was coated with matte black paint, ensuring optimal contrast and accuracy in capturing flow patterns around the simulated vegetation.

The particles introduced by the smoke generator enter through the greenhouse's supply slot (positioned facing the airflow) at an initial velocity of 0.95 $m \cdot s^{-1}$. This experimental setup assumes a two-dimensional configuration, representing the greenhouse along with an obstacle and an open vent, while disregarding transverse direction effects to simplify analysis. The geometry of the setup includes a step with height f at the slot, alongside an obstacle of height h placed at a distance D = 0.45 m from the step.

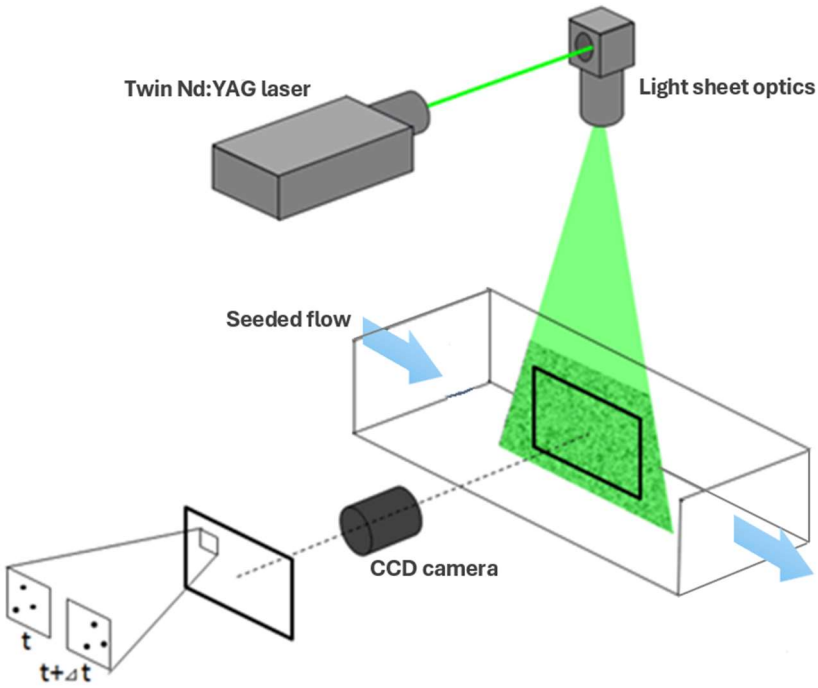

Fig. 2. Schematic diagram of a 2D, two-component (2D-2C) PIV measurement system.

Using visualization data, we were able to map the streamlines, velocity fields, and scalar fields (U), providing a detailed representation of airflow dynamics within this greenhouse configuration. Downstream of the obstacle, the fluid undergoes a rapid expansion, destabilizing the flow and creating a high-shear region characterized by a distinct recirculation zone (see Fig. 3). This recirculation area is defined by a pronounced vortex core, where fluid rotates clockwise and folds back upon itself, illustrating a classic example of shear-induced turbulence. The vortex center is precisely located at coordinates x = 102 mm and y = 68 mm. This recirculation zone plays an important role in mixing and energy dissipation within the greenhouse airflow. The vortex generated in this region is marked by intense rotation, with a core of concentrated kinetic energy that influences surrounding flow patterns. Such airflow characterizations provide insight into how structural features within a greenhouse can impact air distribution, turbulence, and microclimate conditions, ultimately guiding improvements in ventilation design for enhanced climate control efficiency.

Fig. 4 illustrates the velocity field downstream of the obstacle, situated at the center of the unheated tunnel greenhouse. A distinct recirculation zone forms downstream of the obstacle, positioned at y = 50 mm, developing centrally above the supply slot. This visualization demonstrates the obstacle's significant influence on airflow within the tunnel greenhouse, as the horizontal trajectory of the incoming airflow deviates substantially upon interaction with the obstacle. Within this recirculation zone, the velocity exhibits considerable fluctuations, primarily attributable to limitations in the laser sheet's uniformity.

As the laser sheet approaches the center of the lens, a decrease in intensity is observed due to interference from fiber optic inconsistencies, resulting in a phenomenon known as "speckle." This speckle manifests in image files as an oblique dark band along which the tracer particles fail to reflect light adequately. Consequently, when the vortex enters the speckle region, the collected data becomes unreliable, leading to the dispersion evident in this area of the velocity field.

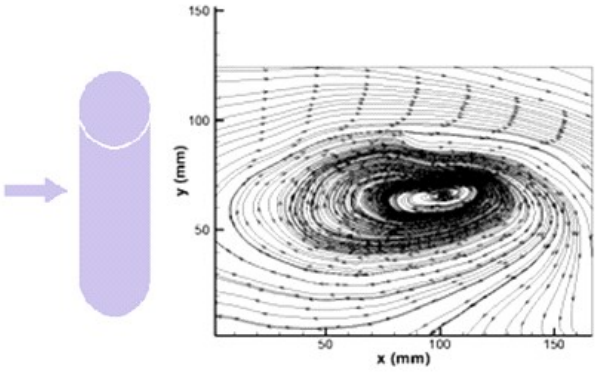

Fig. 3. Streamline patterns near the greenhouse base and downstream the obstacle.

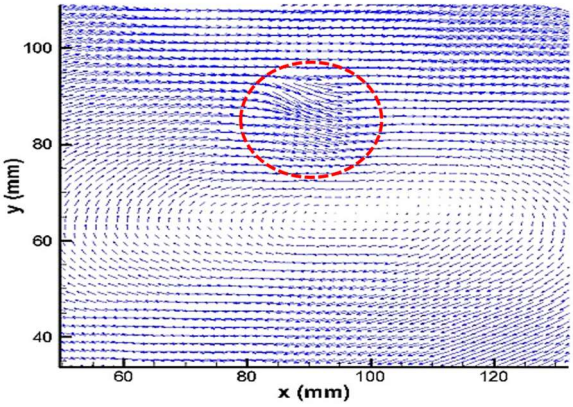

Fig. 4. Velocity distribution downstream of a central obstacle inside the unheated greenhouse.

This irregularity in the laser sheet can affect data quality, underscoring the importance of precise optical calibration in PIV experiments. Such fluctuations also emphasize the challenge of accurately capturing air circulation patterns in complex structures such as greenhouses, where flow interactions with obstacles can produce intricate turbulence and recirculation effects. Recognizing and correcting these optical artifacts is essential to ensure accurate and interpretable results for optimizing greenhouse ventilation and climate management strategies.

The horizontal velocity component U within the greenhouse is depicted in Fig. 5. A negative velocity zone, ranging from -0.12 to -0.06 $m \cdot s^{-1}$, is shown in blue. This area of negative velocity is attributed to the low-pressure area formed immediately downstream the obstacle. As the incoming airflow enters horizontally through the supply slot, it encounters this obstacle, forcing an abrupt change in direction. This sudden shift creates a low-pressure area behind the obstacle, resulting in recirculation. The red-colored region above the tunnel's horizontal wall exhibits an increase in airflow velocity, ranging from 0.22 to 0.26 $m \cdot s^{-1}$. This acceleration is due to the constriction of the airflow path caused by the greenhouse structure, which forces the air to move faster through the reduced area above the obstacle. This pattern demonstrates how the greenhouse's geometric constraints significantly impact airflow behavior, as the obstacle and walls combine to create zones of varying pressure and velocity.

These observations highlight the complex interplay between structural elements and airflow dynamics. Obstacles not only redirect airflow but also intensify it in specific areas. This detailed analysis of the horizontal velocity component contributes to a more comprehensive understanding of the greenhouse's microclimatic conditions.

B. Airflow Characterization Inside the Greenhouse with Bottom Heating

In this section, base heating is applied to the tunnel greenhouse (open on both sides and equipped with the same obstacle), with the aim of studying the dynamics of airflow within this configuration under a temperature gradient and examining the interactions between airflow and heat flux adhesion on the lower wall.

The base heating of the greenhouse is achieved using a copper serpentine heat exchanger mounted beneath the lower wall, specifically under the aluminum plate. Heating is provided by circulating hot water at a temperature of 308 K through this coil. A probe was used to monitor the temperature of the greenhouse's lower wall to ensure it remained consistent with the water temperature. The roof wall is maintained at a constant temperature lower than that of the greenhouse base. Air enters the upstream section of the greenhouse through the supply slot at a velocity of 0.95 m s^{-1}. The Reynolds number, based on the slot height, is 9134, and the study was conducted within the same measurement domain.

The streamlines downstream of the obstacle and above the greenhouse's heated base are depicted in Fig. 6, revealing a complex air recirculation pattern caused by thermal gradients. A notable feature is the emergence of a distinct recirculation zone, where the primary vortex appears to be dividing into two separate cores due to the elevated base temperature.

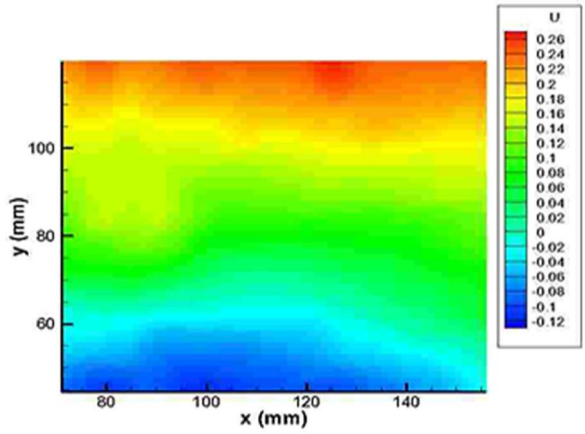

Fig. 5. Distribution of horizontal velocity inside the unheated greenhouse with an obstacle.

The first core of this vortex, situated at approximately x = 60 mm and y = 80 mm, has expanded significantly compared to the unheated setup and has shifted its position. The enlargement and increased amplitude of this core suggest that the temperature gradient at the base is actively enhancing the vortex's dimensions and intensity. Furthermore, a second vortex core begins to develop further downstream at x = 110 mm and y = 76 mm. This secondary core indicates a gradual reorganization of air circulation patterns, likely driven by the buoyancy effect of the heated base, which prompts warmer, less dense air to ascend and cooler air to descend, generating complex recirculatory flows. These observations emphasize that natural convection within the greenhouse is primarily governed by thermal buoyancy forces. The intensified vortex structure and evolving core dynamics demonstrate how a heated base substantially modifies airflow, promoting more vigorous mixing and potentially improving temperature distribution throughout the greenhouse. This thermally-induced convection could play a crucial role in optimizing climate conditions, supporting more uniform heat transfer and potentially enhancing the environment for plant growth.

The velocity field within the tunnel greenhouse, featuring a heated base and central obstacle, is illustrated in Fig. 7. This visualization demonstrates how the temperature gradient affects air movement, creating a secondary, smaller rotating cell adjacent to the main cell observed in the unheated experiment. These two recirculating cells, differing in size but rotating in the same direction, are positioned side by side, indicating a modified airflow pattern due to the heated base.

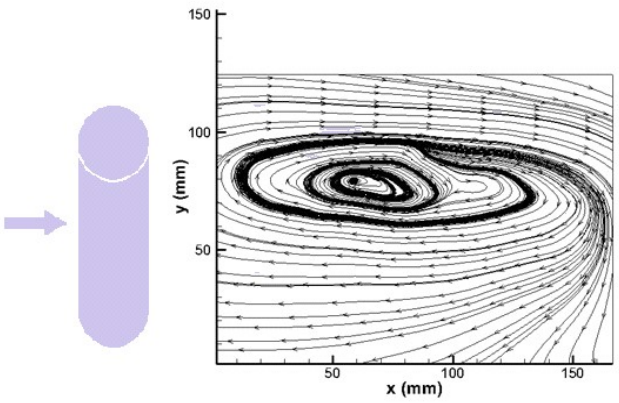

Fig. 6. Streamline patterns near the greenhouse's heated base and downstream the obstacle.

Convective flow initiates and intensifies progressively as the Rayleigh number reaches a critical value of $Ra_c = 10^4$. The air above the lower active surface heats up and becomes less dense. Driven by thermal buoyancy, this warmer, lighter air ascends along the adiabatic vertical walls. As it reaches the cooler upper surface, which is maintained at a constant lower temperature, the air cools and descends through the cavity's center.

This cycle of heating and cooling repeats when the cooler air contacts the heated base, triggering significant warming once more. This process generates counter-rotating convective cells within the cavity, resulting in strong vertical airflow. The observed circulation enhances heat distribution throughout the cavity, with buoyancy-driven motion facilitating continuous exchange between ascending warm air and descending cool air. This phenomenon, fundamental to natural convection in the heated greenhouse, contributes to improved thermal mixing and may lead to more effective climate control within the structure, enhancing air circulation and temperature uniformity.

Fig. 8 displays the horizontal velocity component U. In comparison to the unheated scenario, there is a notable reduction in the low-pressure region, accompanied by an increase in particle velocity. Furthermore, the buoyant effect of thermal gradients is evident as warmer, less dense air particles ascend from the greenhouse's heated base toward the roof. Starting from y = 110 mm, a considerable expansion of the red zone is observed, where particle velocities range from 0.2 to 0.25 m s^{-1}. This behavior demonstrates how thermal effects enhance the upward movement of particles, driven by the decreased air density above the heated base. The increased velocity in this area highlights the importance of thermal buoyancy in amplifying vertical air circulation, which contributes to the heat distribution throughout the greenhouse.

IV. Conclusion

This study investigates airflow dynamics within a greenhouse environment under varying thermal conditions, focusing on the effects of a heated base and the presence of internal obstacles that simulate vegetation. The experimental setup uses Particle Image Velocimetry (PIV) to capture detailed velocity fields and flow patterns in a reduced-scale greenhouse model, both heated and unheated. The aim is to assess the influence of thermal gradients and structural elements on air circulation, convective flow behavior, and heat distribution within the space.

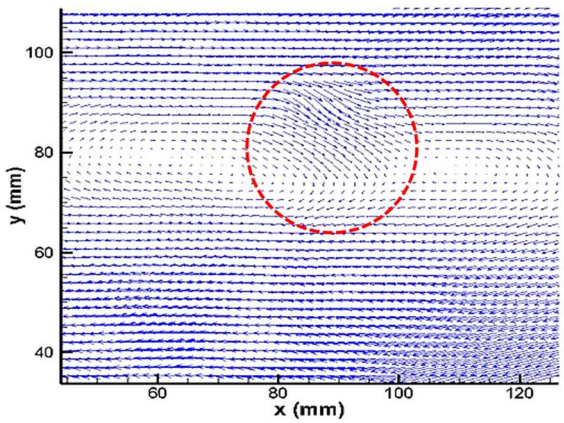

Fig. 7. Velocity distribution downstream of a central obstacle inside the heated greenhouse.

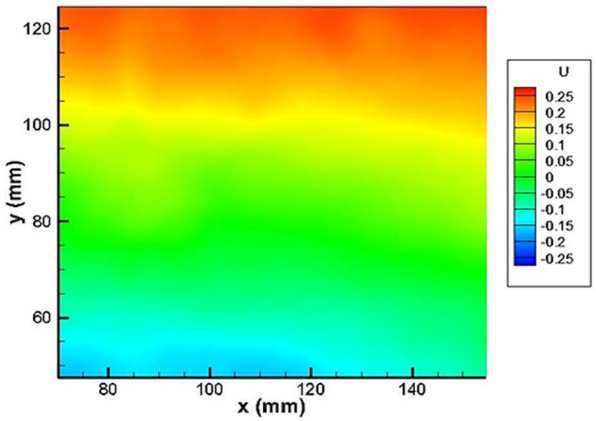

Fig. 8. Distribution of horizontal velocity inside the heated greenhouse with an obstacle.

In the unheated greenhouse scenario, a single recirculating vortex forms downstream of an obstacle, indicating a stable airflow pattern in the absence of a temperature gradient. However, when the greenhouse base is heated, the thermal gradient generates a secondary convective cell adjacent to the primary vortex, revealing the impact of buoyancy-driven forces on airflow dynamics. The study identifies the critical Rayleigh number ($Ra_c = 10^4$) at which convective flow initiates, showing how the ascending warm air creates vertically-oriented convective currents.

Additionally, the analysis of the horizontal velocity component illustrates how thermal gradients reduce low-pressure areas near the obstacle, while enhancing vertical particle movement towards the roof. These findings underscore the role of thermal buoyancy in facilitating vertical circulation, essential for greenhouse climate control and efficient heat distribution. This experimental approach provides a robust framework for evaluating air movement in greenhouse systems, which can inform future design strategies to improve internal climate management and optimize energy use in agricultural structures.

References

[1] Bouadila S, Kooli S, Skouri S, Lazaar M, Farhat A., Improvement of the climate greenhouse using a solar air heater with a latent heat storage, Energy, (2014), 64, 663–672.

[2] Bouadila S, Lazaar M, Skouri S, Kooli S, Farhat A., Assessment of the greenhouse climate with a new packed-bed solar air heater at night in Tunisia, Renew Sust Energy Rev, (2014), 35, 31-41.

[3] Benli H, Durmus A., Performance analysis of a latent heat storage system with phase change material for new designed solar collectors in greenhouse heating, Sol Energy, (2009), 8, 2109–2119.

[4] Berroug F, Lakhal EK, El Omari M, Faraji M, El Qarnia H., Thermal performance of a greenhouse with a phase change material north wall, Energy Build, (2011), 43, 3027-35.

[5] Lazaar M, Bouadila S, Kooli S, Farhat A., Conditioning of the tunnel greenhouse in the north of Tunisia using a calcium chloride hexahydrate integrated in polypropylene heat exchanger, Appl Ther Eng, (2014), 68, 62-68.

[6] Ozgener L, Ozgener O., An experimental study of the exergetic performance of an underground air tunnel system for greenhouse cooling, Renew Energy, (2010), 35, 2804 -11.

[7] Ozgener L, Ozgener O. Energetic performance test of an underground air tunnel system for greenhouse heating, Energy, (2010), 35, 4079-85.

[8] Lazaar M, Kooli S, Hazami M, Farhat A, Belghith A, Use of solar energy for the agricultural greenhouses autonomous conditioning, Desalination, (2004), 168, 169-175.

[9] Lazaar M, Kooli S, Hazami M, Farhat A, Belghith A, Comparison between a solar system and a fuel boiler for greenhouse air-conditioning, Desalination, (2004), 168, 391-396.

[10] Lazaar M, Kooli S, Hazami M, Farhat A, Belghith A, Thermal energy storage in the ground of a greenhouse by the polypropylene capillary heat exchanger, Am J Appl Sci, (2008), 5, 1769-1772.

[11] Hazami M, Kooli S, Lazaar M, Farhat A, Belghith A, Thermal performance of a solar heat storage accumulator used for greenhouse conditioning, Am J Environ Sci, (2005), 4, 270-277.

[12] Hassen Boughanmi, Mariem Lazaar, Abdelhamid Farhat, Amenallah Guizani, Evaluation of soil thermal potential under Tunisian climate using a new conic basket geothermal heat exchanger: Energy and exergy analysis, Applied Thermal Engineering, 113, (2017), 912-925.

[13] Hassen Boughanmi, M. Lazaar, A. Guizani, A performance of a heat pump system connected a new conic helicoidal geothermal heat exchanger for a greenhouse heating in the north of Tunisia, Sol. Energy, 171, (2018), 343–353.

[14] Hassen Boughanmi, Nawel Khaldi, Mariem Lazaar, Amanallah Guizani, Enhancing nocturnal microclimate in Tunisian greenhouses: Experimental study on integrating an innovative conic helicoidal heat exchanger with a geothermal heat pump system, Geothermics, 123, (2024), 103–127.

[15] Saeed Mahdavi, Faramarz Sarhaddi, Mahdi Hedayatizadeh, Energy/exergy based-evaluation of heating/cooling potential of PV/T and earth-air heat exchanger integration into a solar greenhouse, Applied Thermal Engineering, 149, (2019), 996–1007.

[16] Danial Tahery, Ramin Roshandel, Akram Avami, An integrated dynamic model for evaluating the influence of ground to air heat transfer system on heating, cooling and CO2 supply in Greenhouses: Considering crop transpiration, Renewable Energy, 173, (2021), 42–56.

[17] Ahmad Banakar, Mehdi Montazeri, Barat Ghobadian, Hadi Pasdarshahri, Fatemeh Kamrani, Energy analysis and assessing heating and cooling demands of closed greenhouse in Iran, Thermal Science and Engineering Progress, 25, (2021), 101–042.

[18] Q. Chen, J. Srebric, A procedure for verification, validation, and reporting of indoor environment CFD analyses, VAC&R Research, 8 (2) (2002), 201–216.

[19] J. Srebric, V. Vukovic, G. He, X. Yang, CFD boundary conditions for contaminant dispersion, heat transfer and airflow simulations around human occupants in indoor environments, Building and Environment, 43 (3) (2008), 294–303.

[20] W. Liu, J. Wen, J. Chao, W. Yin, C. Shen, D. Lai, C.-H. Lin, J. Liu, H. Sun, Q. Chen, Accurate and high-resolution boundary conditions and flow fields in the first-class cabin of an MD-82 commercial airliner, Atmospheric Environment, 56 (2012), 33–44.

[21] X. Cao, J. Liu, N. Jiang, Q. Chen., Particle image velocimetry measurement of indoor airflow field: A review of the technologies and applications, Energy and Buildings, 69, (2014), 367–380.

[22] M. Krajčík, A. Simone, B.W. Olesen, Air distribution and ventilation effectiveness in an occupied room heated by warm air, Energy and Buildings, 55 (2012), 94–101.

[23] S. Morsing, J. Strøm, G. Zhang, P. Kai, Scale model experiments to determine the effects of internal airflow and floor design on gaseous emissions from animal houses, Biosystems Engineering, 99 (1) (2008), 99–104.

[24] T. Boulard, R. Haxaire, M.A. Lamrani, J.C. Roy, A. Jaffrin, Characterization and modelling of the air fluxes induced by natural ventilation in a greenhouse, Journal of Agricultural Engineering Research, 74 (1999), 135–144.

[25] I.B. Lee, S. Sase, L. Okushima, A. Ikeguchi, K. Choi, J. Yun, A wind tunnel study of natural ventilation for multi-span greenhouse scale models using two-dimensional particle image velocimetry PIV, Transaction of the ASAE, 46 (2003), 763–772.

[26] L. Okushima, S. Sase, T. Maekawa, A. Ikegushi, Airflow patterns forced by wind effect in a Venlo type greenhouse, Journal of Society on Agricultural Structure in Japan, 29 (3) (1998), 159–167.

[27] Molina-Aiz, D.L. Valera, A.J. Alvarez, Measurement and simulation of climate inside Almeria-type greenhouses using computational fluid dynamics, Agricultural and Forest Meteorology, 125 (2004), 33–51.

[28] Z. Zhang, W. Zhang, Z.J. Zhai, Q.Y. Chen, Evaluation of various turbulence models in predicting airflow and turbulence in enclosed environments by CFD: part 2—comparison with experimental data from literature, HVAC&R Research, 13 (6) (2007), 871–886.

[29] F. Kuznik, G. Rusaouen, J. Brau, Experimental and numerical study of a full-scale ventilated enclosure: comparison of four two equations closure turbulence models, Building and Environment, 42 (3) (2007), 1043–1053.

[30] P. Rohdin, B. Moshfegh, Numerical predictions of indoor climate in large industrial premises: A comparison between different k–ε models supported by field measurements, Building and Environment, 42 (11) (2007), 3872–3882.

[31] M. Wang, Q. Chen, Assessment of various turbulence models for transitional flows in an enclosed environment (RP-1271), HVAC&R Research, 15 (6) (2009), 1099–1119.

Heat transfer characteristics of thermosyphons used in vacuum tube water heaters

Zied Lataoui
Laboratory for the Studies of Thermal and Energy Devices (LESTE)
Engineering School of Monastir (ENIM)
University of Monastir
Monastir, Tunisia
zied_lataoui@yahoo.fr

Adel M. Benselama
Pprime Institute
ENSMA Engineering School
Futuroscope Cedex, France
adel.benselama@ensma.fr

Abdelmajid Jemni
Laboratory for the Studies of Thermal and Energy Devices (LESTE)
Engineering School of Monastir (ENIM)
Monastir, Tunisia
line abdelmajidjemni1@gmail.com

***Abstract*—A comprehensive computational model of a two-phase closed thermosyphon used in water heaters is developed. The implemented openFOAM solver is then used to investigate the effects of the main operating conditions. It allowed capturing well the main heat and mass transfer phenomena involved in a closed thermosyphon. In particular, it is shown that optimal heat transfer parameter can be reached for high heat input power values (>300 W), and a tilt angle of 60° for intermediate operating temperatures (50-130°C). The lowest thermal resistance is obtained at near vertical positions (90°), for high temperatures (>150°C).**

Keywords— heat transfer, thermosyphon, inclination angle, openFOAM, vacuum tube collector

I. INTRODUCTION

To take advantage of solar power in heating applications, evacuated tube solar water heaters are prominently used [1]. There is indeed a substantial need of substituting fossil resources by renewable and sustainable energy means. Many countries have set goals for their energy infrastructure development in order to limit greenhouse gases emission [2]. Improving the global efficiency and optimizing the operation of solar devices, such as water heaters, are then actual challenges. Incorporation of heat pipes (particularly, the two-phase closed thermosyphons TPCT) in the collector is shown to significantly enhance the solar water performance [3].

A TPCT is a highly efficient heat transmitter involving liquid-vapor phase change: at the evaporator section, the liquid is evaporated due to the absorbed heat. The vapor flows through an adiabatic zone to the condenser region where it condenses, at the saturated state, by transferring heat to the cooling media [4]. The liquid drops back to the evaporator as a thin film by gravity effect. Fundamentally, the evaporator where a pool exists is placed in the TPCT bottom.

Many experimental and numerical studies on thermosyphons have been conducted to estimate the heat transfer characteristics and to describe the two-phase flow patterns under various operating conditions.

Jafari et al. [5] discussed the factors influencing the heat transfer performance of thermosyphons. They reported that the working fluid, the inclination angle and the filling ratio are important parameters affecting the performance and the internal flow patterns of thermosyphon. Arat et al. [6] experimentally investigated the effects of the fluid volume and the inclination angle on the heat transfer coefficients in the condenser and the evaporator sections. For various vacuum pressure values, they also concluded that the lowest thermal resistance was obtained for a near vertical position (an inclination angle of 90°). Lataoui et al. [7] conducted an experimental study on the effect of the operating conditions (the working fluid, the filling ratio, the temperature and the heat input) on the thermal performance of a TPCT. They showed that the heat transfer coefficient in the evaporator could be well predicted in comparison with the analytical correlations, especially for an overfilled evaporator configuration and for low heat fluxes. Critical and optimal inclination angles of a TPCT were experimentally investigated by Gou et al. [8]. The obtained results showed that the critical angle was 45° for all the operating conditions. The optimal angle was 60° for the temperature interval 80-150°C, and 90° for higher temperatures (150-185°C). Kim et al. [9] conducted also an experimental study to examine the effects of the filling ratio and the tilt angle on the boiling and condensation heat transfer within a water/copper TPCT. The best thermal performance was obtained at an inclination angle of 30° and a filling ratio of 50%. A core tube monitoring TPCT has been developed and tested by Wang et al. [10]. The experimental results showed that the thermal resistance is more affected by the tilt angle in the evaporator than in the condenser. The best heat transfer performance was obtained for 10° of inclination angle. More recently, Li et al. [11] conducted an experimental and numerical study to characterize the transient thermal and flow behavior of a TPCT for various filling ratios. Based on the calculation of the net vapor production, the temperature and pressure distribution, and the startup time has been accurately predicted (overall error was within 10%).

Shabgard et al. [12] developed a mathematical model to investigate the effect of the filling ratio on the transient thermal behavior of a vertical TPCT. They found that the optimally filled thermosyphon provide the smallest thermal resistance and the shortest thermal response time. A slight increase in the input power would however trigger the dry-out at the evaporator section.

A computational model of the TPCT was undertaken by Ahmed et al. [13] to examine the effects of a wide range of operating conditions, namely the filling ratio, the inclination tilt, and the power input. They concluded that the developed methodology assisted to reveal the essential mechanisms of the thermal performance and two-phase flow of the proposed TPCT used in concentrated solar collector applications. It was shown that the optimal performance of the TPCT (high heat transfer coefficient and low thermal resistance) was obtained at 250W (power input), 90° (tilt angle) and 0.5 (filling ratio). All the studies described above show a lack of numerical

investigations on the effect of the tilt angle. It is indeed an important parameter and optimizing it is an actual challenge. It requires then to develop a reliable tridimensional computational model.

The main objective of the present study consists in developing a reliable simulation model and using it to investigate the effects of main operating conditions on the heat transfer coefficients and the overall thermal resistance. It is validated by comparing numerical results to the experimental data of previous studies. The effect of the inclination angle, among other parameters, on the heat transfer performance of the TPCT is also discussed.

II. Governing Equations

For multiphase flows, phase transition methods are commonly used to define the transport at the interface. It can be classified into two categories: tracking methods and capturing methods. The application of the volume of fluid method (VOF), a capturing method, offers the advantage of an improved interface resolution while reducing spurious oscillations and parasitic effects when the reconstruction algorithm is properly chosen [14].

According to this approach, a cell in the domain can contain liquid, vapor or both phases. Each phase is considered through its volume fraction (α_l and α_v, respectively). It makes then tracking the liquid-vapor interface possible by solving the continuity equation of one phase (generally the liquid). The remaining equation set, based on Navier-Stokes equations, is also treated numerically for both phases in the limit of thermal and dynamic relaxation. The variable flow and thermal characteristics (T, P and u) are shared by the two phases. The thermophysical properties (like density ρ, dynamic viscosity μ, heat capacity per unit volume ρcp, and thermal conductivity k) are calculated as a volume average based on the liquid and vapor phases single characteristics. In addition, the following assumptions are considered:

- Nucleate boiling is considered during the phase change model;
- The pure vapor phase is assumed to be an ideal gas;
- The liquid flow is considered as incompressible;
- The liquid-vapor interface is close to quasi-equilibrium state even during the phase change process.

The governing equations are described hereby, for the liquid phase (according to the volume of fluid approach):

- The continuity equation:

$$\frac{\partial(\alpha_l \rho_l)}{\partial t} + \nabla \cdot (\alpha_l \rho_l \vec{u}) = S_m \quad (1)$$

Where α_l and ρ_l are the liquid volume fraction and density, respectively. Sm is the mass source/sink term due to phase change.

- The momentum conservation equation:

$$\frac{\partial(\rho \vec{u})}{\partial t} + \vec{\nabla} \cdot (\rho \vec{u} \vec{u}) = \rho \vec{g} - \vec{\nabla} P + \vec{\nabla} \cdot [\mu (\vec{\nabla} \vec{u} + (\vec{\nabla} \vec{u})^T)] + \vec{F}_{CSF} \quad (2)$$

- The energy conservation equation:

$$\frac{\partial(\rho H)}{\partial t} + \nabla . [(\rho H) \vec{u}] = \nabla . (k \vec{\nabla} T) + S_E + \frac{dP}{dt} + \nabla . [(\vec{\nabla} \vec{u} + (\vec{\nabla} \vec{u})^T) . \vec{u}] \quad (3)$$

The flow involved only two-phases, so the liquid and vapor volume fractions are linked by:

$$\alpha_l + \alpha_v = 1 \quad (4)$$

The density ρ and dynamic viscosity μ of the liquid-vapor mixture are respectively expressed as:

$$\rho = \alpha_l \rho_l + \alpha_v \rho_v \quad (5)$$

$$\mu = \alpha_l \mu_l + \alpha_v \mu_v \quad (6)$$

$\vec{F}_{CSF}$ is the continuum force considering capillarity written as [15]:

$$\vec{F}_{CSF} = \sigma_{lv} \frac{\alpha_l \rho_l \kappa_v \vec{\nabla} \alpha_v + \alpha_v \rho_v \kappa_l \vec{\nabla} \alpha_l}{0.5 (\rho_l + \rho_v)} \quad (7)$$

σ_{lv} is the liquid-vapor surface tension and κ is the interface curvature:

$$\kappa_l = -\kappa_v = -\nabla \cdot \left(\frac{\vec{\nabla} \alpha_l}{\| \vec{\nabla} \alpha_l \|} \right) \quad (8)$$

The enthalpy H of the liquid-vapor mixture can be defined as:

$$H = \frac{\rho_l c_{pl} \alpha_l + \rho_v c_{pv} \alpha_v}{\rho_l \alpha_l + \rho_v \alpha_v} (T - T_{sat}) \quad (9)$$

The thermal conductivity of the mixture k is given by:

$$k = \alpha_l k_l + \alpha_v k_v \quad (10)$$

k_l and k_v are respectively the thermal conductivity of liquid and vapor phases.

The continuity equation source term S_m can be obtained as [15]:

Evaporation: $S_m = -\beta_e \alpha_l (P_{sat} - P)$ if $P \leq P_{sat}$ (11)

Condensation: $S_m = \beta_c \alpha_v (P - P_{sat})$ if $P > P_{sat}$ (12)

β_e and β_c are called mass transfer time parameters or relaxation coefficients for evaporation and condensation, respectively. These parameters were mostly set at constants in models reported in literature. However, it reflects the rate of evaporation and condensation in the phase-change process. It is assumed to have a strong effect on the volume interface and vary from 0.1 to 10^{-7} s^{-1} [15]. In our case, the proportionality to phase densities was almost verified:

$$\frac{\beta_e}{\beta_c} = \frac{\rho_v}{\rho_l} \quad (13)$$

The saturation pressure can be derived from the temperature field according to the Clausius-Clapeyron formula:

$$\frac{P_{sat}}{P} = \exp \left(- \frac{M h_{lv}}{R} \left(\frac{1}{T_{sat}} - \frac{1}{T} \right) \right) \quad (14)$$

h_{lv} is the latent heat of vaporization.

The energy source term is obtained as:

$$S_E = S_m h_{lv} \quad (15)$$

III. Numerical Procedure

The set of equations described above was solved using the open source software OpenFOAM (v6) [16]. OpenFOAM is a free, open source CFD software based on finite volume formulation. It has an extensive range of features making it able to simulate many processes from complex fluid flows involving chemical reactions, turbulence and heat transfer, to acoustics, solid mechanics and electromagnetics. In particular, it offers the ability to modify and improve solvers to fit with the very considered problem.

Hence, an extensible phase-change solver is developed. This package enables the run-time selection of different phase change formulations. The solver is based on the adiabatic two-phase flow with phase change interPhaseChangeFoam [16], and provides access to extensive OpenFOAM functionality (MPI parallelization, turbulence models, discretization schemes, linear solvers). In particular, it offers the ability to modify and improve solvers to fit with the very considered problem. This software thus enables simulation of diverse phase change processes in a single environment. We have also incorporated the heat transport equation and coupled phase-change source terms in the governing equations as well as the compressibility of the vapor phase. The saturation pressure is taken here to be temperature-dependant. The complete model is then expected to simulate mass and heat transfer in two-phase flows with phase changes and to take into account the main phenomena involved in a heat pipe operation.

A. *Simulation Model*

Fig. 1 shows the schematic details of an evacuated tube collector involving heat pipes. To improve the efficiency of the water heater, it is interesting to investigate first the heat transfer characteristics of the TPCT, the main component of the evacuated tube collector. It consists in a carbon steel/water TPCT.

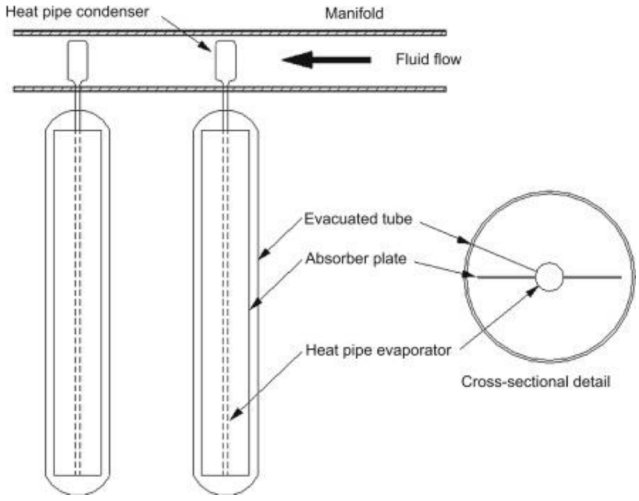

Fig. 1. Schematic diagram of an evacuated tube collector with heat pipes [3].

The considered model is described in Fig. 2. It also shows the different sections of the TPCT and the tilt angle θ.

The constant heat flux density boundary condition (q_{in}) was applied for the evaporator:

$$q_{in} = \frac{Q_{in}}{\pi D L_e} \qquad (16)$$

Where D is the TPCT external diameter, L_e is the evaporator length and Q_{in} the heat flux set at the evaporator section.

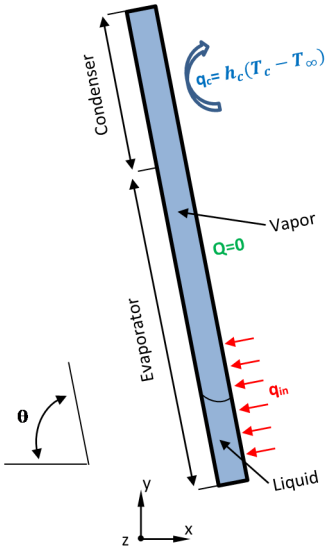

Fig. 2. The thermosyphon model description.

For the condenser, a convective boundary condition was considered:

$$q_c = \frac{Q_c}{\pi D L_c} \text{ and } Q_c = \pi D L_c h_c(T_c - T_\infty) \qquad (17)$$

q_c and Q_c are the heat flux density and heat flux at the condenser section, respectively. L_c is the condenser length. T_∞ is the free stream temperature of the outer coolant fluid and h_c is the heat transfer coefficient at the condenser section.

The developed model is tested for a TPCT experimental case [8]. It consists in a cylindrical water/stainless steel TPCT. Its main characteristics are summarized in table I.

TABLE I. Setup parameters of the tested TPCT [8]

Parameter	Value
Working fluid	Water
Wall material	Carbon steel
Tube diameter	28 mm
Total lenght	1486 mm
Evaporator lenght	1106 mm
Condenser lenght	380 mm
Filling ratio	48 % (of the evaporator volume)
Input power	100, 200 and 300 W
Tilt angle	0, 15, 30, 45, 60, 75 and 90°

B. *Solution Strategy*

The governing equations are discretized using the finite volume method, and are solved at each simulation time step. A structured hexa-hedralateral grid with different element numbers is generated using the blockMesh utility in OpenFoam [16]. Fig. 3 shows the main characteristics of the meshed domain of the TPCT. The liquid phase is considered as the primary-phase. The numerical solution of the equations and time progress are performed through an iterative algorithm PIMPLE, a combination of PISO and SIMPLE algorithm features.

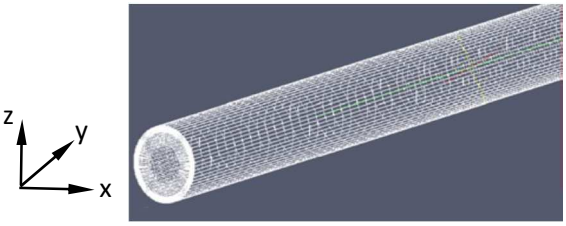

Fig. 3. Mesh details of the TPCT.

A transient solution with a self-adjusted time step is carried out in the model. A maximum global Courant number of 0.2 is set to ensure the stability of the simulation solutions. The pseudo-steady state regime is assumed reached when random mean temperatures in the evaporator and condenser sections are almost constant (time fluctuations less than 1%). Fig. 4 shows, for example, the time variations of the temperature at random positions at the evaporator and the condenser sections. It clearly confirms that the steady state is almost reached after 30 s of simulation time. For most of the simulation cases, it corresponds to 30-60 s and it takes more than 10 days using a 16-core workstation with meshes consisting of about 150000 cells.

IV. Results and Discussion

A. *Model Validation*

The developed numerical model was tested under a set of operating conditions (Q_{in}=100W, tilt angle=90°: vertical position). The obtained results were expressly compared with experimental data of Gou et al. [8]. Fig. 5 shows a good accordance between the simulated and measured temperatures along the TPCT.

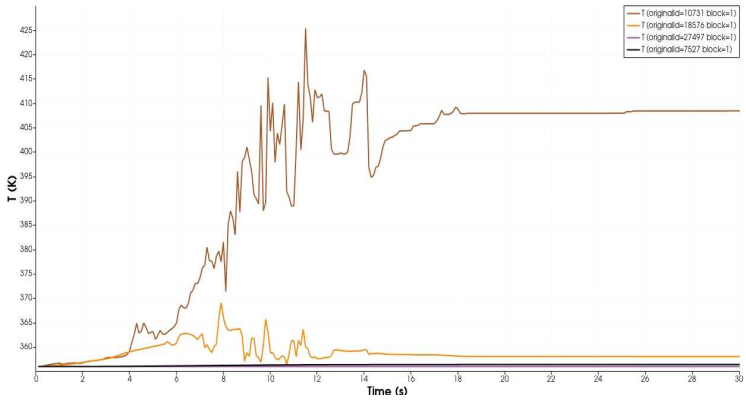

Fig. 4. Time variations of the temperature at the condenser and the evaporator sections.

It is worth mentionable that the temperature in the evaporator bottom, where the liquid pool is set, was well estimated. Whereas, numerical fluctuations were noticeable in the evaporator top. It still however limited. It was associated with bubble formation and vapor generation at the section above the liquid-vapor interface. The plotted temperatures are indeed simulation results at the fluid-solid frontier. At the condenser, the wall temperature were over-estimated, in comparison with the experimental measurements, particularly in the condenser top. It can be explained by the fixed convective heat transfer coefficient and the cooling temperature condition considered in the TPCT model.

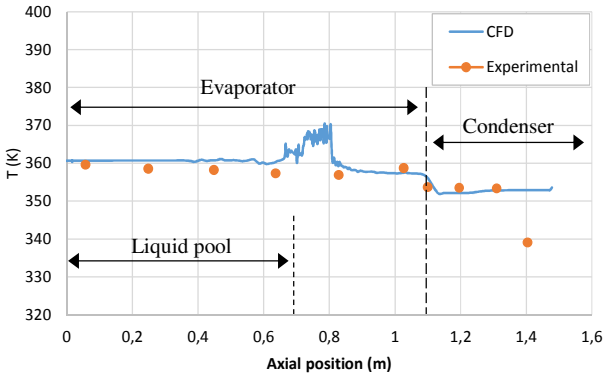

Fig. 5. Comparison betweed simulation results and experimental data.

(*Q_{in} = 100W ; T_{sat}=353K ; vertical position*)

In addition, the TPCT model was efficiently able to capture bubble formation and growth, like it is shown in Fig. 6. It was also able to simulate condensation, and liquid film falling along the inner wall. Bubbles were continuously generated at the top region of the liquid pool. It went then to the vapor region through the liquid-vapor interface (Fig. 6.).

The developed numerical tool was used to investigate the effect of the operating conditions on the TPCT thermal performance. The study was particularly focused on the input heat power and the inclination angle parameters. For this aim, the equivalent heat transfer coefficient (at the evaporator) h_e and the overall thermal resistance R_{th} were respectively calculated as:

$$h_e = \frac{Q_{in}}{\pi\, D\, L_e(\overline{T}_e - T_{sat})} \tag{17}$$

$$R_{Th} = \frac{\overline{T}_e - \overline{T}_c}{Q_{in}} \tag{18}$$

Where Q_{in}, D and L_e are respectively the input heat power, the TPCT diameter and the evaporator length. $\overline{T}_e$ and $\overline{T}_c$ are the mean temperatures at the evaporator and the condenser.

B. *Effect of the Heat Power*

The average global irradiation is between 4.2 and 5.8 kWh/m² per day, in south Mediterranean countries [17]. For the considered TPCT, it implies an equivalent input power of 20 to 100W, when the heat loss is neglected. It can reach 300W in other regions [18]. For the vertical position (θ=90°), Fig. 7 shows the variation of the heat transfer coefficient h_e and the thermal resistance R_{Th} according to the input power Q_{in}.

The equivalent heat transfer at the evaporator is almost constant for relatively low heat input (Q_{in}<100W). Over

100W, it increases expressively to reach 500 W/m²K. This can be explained by the increased evaporation rate consequently to the heat input increase.

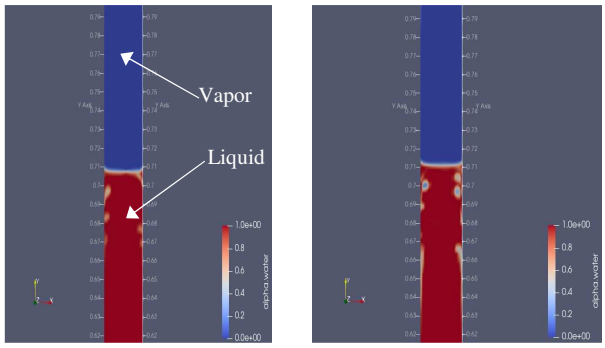

Fig. 6. Bubble creation and growth at the evaporator top

The overall thermal resistance of the TPCT is almost constant and high for Q_{in}<100W. Whereas, it decreases significantly to 0.04 and 0.03 K/W, respectively for input power of 200 and 300 W. It confirms that the heat transfer is improved for high heat input levels (200-300 W).

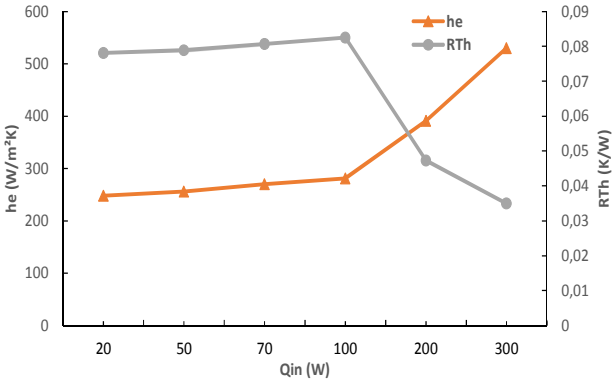

Fig. 7. Effect of the input power on the heat transfer parameters

C. *Effect of the tilt angle*

The developed numerical tool is then used to investigate the effect of the inclination of the TPCT on the heat transfer characteristics. Fig. 8 Shows indeed the variation of the overall thermal resistance R_{Th} according to the tilt angle, for various operating temperature T_{sat} (80, 130 or 175 °C).

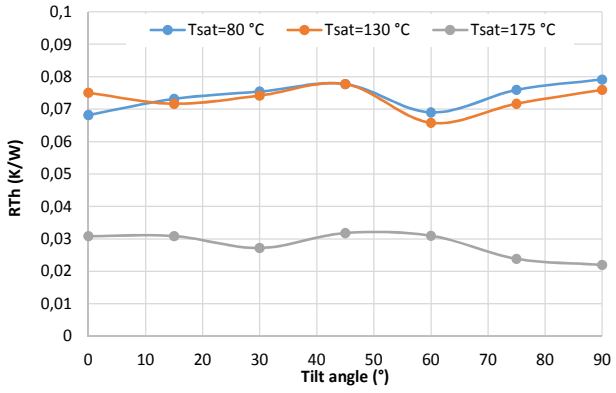

Fig. 8. Effect of the tilt angle on the Thermal resistance

In particular, it is shown that an inclination angle of 60° is the optimal value, for temperatures under 150°C, allowing the best (and minimal) values of the overall thermal resistance. In fact, the component force acting on the inner surface of TPCT is tiny, When the inclination angle is small, causing the working fluid failure to quickly return to the evaporation section, which affects the gas-liquid conversion rate. The heat transfer performance is consequently weaker. When the inclination angle increases, the gas-liquid two-phase flow in the tube is in the upper and lower layers, which do not conflict with each other and the shear force is small. The internal steam's high-speed scouring of the liquid film in the condensation section also makes the relative resistance gradually reduce. It should be noted that since the top of the TPCT evaporation section is directly in contact with the condensation section, the effect of gravity will not significantly change the distribution of the liquid film. It has then little influence on the thermal resistance, and the heat transfer performance at high inclination angles (near the vertical position) is poor at low power.

For high input power, and high operating temperature (over 150°C), the lowest thermal resistance is obtained for near vertical position (θ=90°).

V. Conclusions

With the increasing industrial demand of water heating, under various climate conditions, a need has been developed to predict and improve the performance of a solar thermal system based on heat pipe evacuated tubes. This study focused on the thermal performance optimization of a TPCT used in vaccum tube solar collectors. For this aim, a numerical model was developed using the openFOAM toolbox. The obtained results were validated by comparing it with the experimental results of previous studies. A good accordance has indeed been revealed. The effects of the input heat power and the inclination angle were particularly investigated. The increase of the input heat power conducted a decrease in the thermal resistance associated with the improvement of the heat transfer coefficient. It was also shown that for an operating temperature under 130°C, the optimal inclination angle θ was around 60°; whereas it was nearly 90° (vertical position) for higher temperatures (over 150°C). For intermediate temperature (50-130°C), a tilt angle of 60° is recommended to deserve a relatively low thermal resistance and a good heat transfer along the TPCT. Further attention should be given to investigate the correlated effects of all the operating conditions, in order to describe the optimal parameters of a TPCT.

Acknowledgment

This research was carried out as part of the PHC-Utique program supported both by the French and Tunisian governments under contract CMCU no. 23G1104.

References

[1] A. Fudholi, K. Sopian, "A review of solar air flat plate collector for drying application", Renew. Sustain. Energy Rev., vol. 102, pp. 333-345, 2019.

[2] European Commission. Proposal for a Regulation of the European Parliament and of the Council Establishing the Framework for Achieving Climate Neutrality and Amending Regulation (EU) 2018/1999 (European Climate Law). 2020. Available online:

https://eurlex.europa.eu/legalcontent/EN/TXT/PDF/?uri=CELEX:52020PC0080&from=EN

[3] S. Aggarwal, R. Kumar, D. Lee, S. Kumar, and T. Singh, "A comprehensive review of techniques for increasing the efficiency of evacuated tube solar collectors", Heliyon, 2023, e15185. https://doi.org/10.1016/j.heliyon.2023.e15185.

[4] M.B..H Mantelli, "Thermosyphon and Heat Pipes: Theory and Applications", 1st ed. Springer Nature Switzerland, 2021.

[5] D. Jafari, A. Franco, S. Filippeschi, and P. Di Marco,"Two-phase closed ther-mosyphons: a review of studies and solar applications", Renew. Sustain. Energy Rev. 53, pp. 575-593, 2016.

[6] H. Arat, O. Arslan, U. Ercetin, and A. Akbulut, "Experimental study on heat transfer charcateristics of closed thermosyphon at different volumes and inclination angles for variabe vacuum pressures", Case Studies Th. Eng., vol. 26, pp. 101-117, 2021.

[7] Z. Lataoui, A. Jemni, "Experimental investigation of a stainless steel two-phase closed thermosyphon", J. Appl. Thermal. Eng., vol. 121, pp. 721-727, 2017.

[8] X. Gou, G. Li, R. Zhang, Ch. Jian, et al., "Critical and optimal inclination angles of two-phase closed thermosyphon under different operating conditions", Int. J. Heat and Mass Transf., vol. 177, 121540, 2021.

[9] Y. Kim, D. H. Shin, J. S. Kim, S. M. You, and J. Lee, "Boiling and condensation heat transfer of inclined two-phase closed thermosyphon with various filling ratios", J. App. Thermal Eng., vol. 145, pp. 328-342, 2018.

[10] Y. Wang, X. Wang, J. Wang, Y. Liu, and J. Chen, 'Heat transfer performance of a two-phase closed thermosyphon with different incination angles based on the core-tube monitoring", Case Stud. Therm. Eng., vol. 42, 102738, 2023.

[11] G. Li, Y. Zhang, G. Zhang, Sh. Huang, and Sh. Ding, "Transient experimental and numerical study of thermosyphon under different heating fluxes and filling ratios", J. Appl. Thermal Eng., vol. 243, 122514, 2024.

[12] H. Shabgard, B. Xiao, A. Faghri, R. Gupta, and W. Weissman, "Thermal characteristics of a closed thermosyphon under various filling conditions", Int. J. Heat and Mass Transf., vol. 70, pp. 91-102, 2014.

[13] I. S. Ahmed, and A. M. Al Jubori, "Assessment of heat transfer and flow characteristics of a two-phase closed thermosiphon", Heat Transf., vol. 50, pp. 1351-70, 2021.

[14] G. Tryggvason, R. Scardovelli, and S. Zaleski, "Direct numerical simulations of gas-liquid multiphase flows", Cambridge University Press, 2011.

[15] X. Wang,Y. Zhu, and Y. Wang, "Development of pressure-based phase change model for CFD modelling of heat pipes", Int. J. Heat Mass Tran., vol. 145, 118763, 2019.

[16] The OpenFOAM Foundation, OpenFOAM v6. [Online]. Available: https://openfoam.org/download/6-linux/; 2018.

[17] https://www.anme.tn/en/content/solar-photovoltaic.

[18] P. M. Kumar, and K. Mylsamy, "A comprehensive study on thermal storage characteristics of nano-CeO2 embedded phase change material and its influence on the performance of evacuated tube solar water heater", Renew. Energy, vol. 162, pp. 662-676, 2020.

Design of a Hybrid PV-Wind Power System with Battery-Supercapacitor Hybrid Storage: Madinah Case Study

Abdussamad Muhammad Sadis
Department of Electrical Engineering
Islamic University of Madinah
Madinah, Saudi Arabia
amsadis21@gmail.com.com

Emad Alrwishdi
Department of Electrical Engineering
Islamic University of Madinah
Madinah, Saudi Arabia
emadalrwishdi@hotmail.com

Azeddine Draou, SMIEEE'02
Department of Electrical Engineering
Islamic University of Madinah
Madinah, Saudi Arabia
az_draou@iu.edu.sa

***Abstract* — The intermittent nature of PV and wind renewable sources makes their hybridization a good idea, to improve power stability and energy sustainability. Over the past years both systems have been in use, either separately or in combination, although standalone systems are practically in abundance. The systems can be on/off-grid, depending on the need. In addition, energy storage systems are also crucial to the well-functioning of both systems, storing the energy during the off-peak and delivering it when needed. Batteries have proven their worth in terms of high-energy density and durability. Some of its drawbacks are low-power density and a smaller number of active cycles. On the other hand, supercapacitor can complement the drawbacks of the battery, providing a higher-power density and extended life cycle. The hybridization of these systems provides ancillary support to the grid as well as power stability. This paper proposes a PV-wind Hybrid Renewable Energy System (HRES) integrated with a battery-SC Hybrid Energy Storage System (HESS). It involves the modelling and simulation of a 7.3 kW PV system, and a 1 kW wind turbine. Reduction of harmonics was carried out by implementing P&O MPPT technique at the boost converters, Furthermore, simulation of the Battery-SC storage was also presented, involving a bidirectional DC-DC converter to enable two-way power flow. Simulations are carried out using MATLAB and Photovoltaic Geographical Information System (PVGIS).**

Keywords —PV-wind Hybrid, Battery-supercapacitor hybrid, Storage, DC bus, Energy and power density.

1. Introduction

With the current increase in global population and industrialization processes, the contemporary world experiences an exponential increase in terms of energy demand [1]. In addition, the world tends to defect away from using the existing fossil fuel energy generation, due the increasing price of fuel and greenhouse effect [2]. Although fossil fuel has quite proven its worth and dominance worldwide due to high efficiency [3]. Nonetheless, the consequences that occur from the greenhouse emissions cannot be overlooked, issues like global warming and climate change are cases of high concern to the world. This gives rise to high investment and exploration in renewable energy, with sources like solar and wind taking the lead in this regard [4]. Both systems are naturally intermittent. hence combining the two systems thereby making a hybrid system is crucial to solving the problem of intermittency, and subsequent renewable energy challenges like energy stability, sustainability, and power quality.

Furthermore, developments in HRES and Energy Storage System (ESS) have gained much consideration over the years. PV-wind HRES is the most developed model, integrated with battery storage especially in microgrids and electric vehicles. Numerous recent research has focused on the issue of hybridizing the two sources. In terms of sizing and optimization Anoune et al. [5] presented an updated literature review on sizing and optimizing PV-wind based Hybrid Systems (PWHS) for isolated areas. The focus is on achieving an optimal balance between power reliability and system costs. The document compares common PWHS topologies, introduces a mathematical model emphasizing power reliability and system cost, and analyses software tools and algorithms used in sizing optimization. Albusaidi et al. [6] reviewed the diverse hybrid PV-Wind renewable energy systems for electricity generation, discussing sizing criteria based on logistical, environmental, and economic factors. It also explores optimization techniques comparing energy production cost and performance using simulations. Specifically focusing on Oman's varying wind and solar energy potential, the paper addresses the optimal sizing process for two proposed PV-Wind plants in the country. HRES is not restricted to microgrid applications, but also extended to other applications, in [7] Angadi et al. reviewed the application of HRES in pumping water. The authors modelled the system using MATLAB, proposed an effective control system. Al-Mamun et al. proposed hybrid renewable system in Bangladesh, comprising a wind turbine and a solar module. The system was designed using PSIM and MATLAB. During the simulation, the authors varied the wind speed and monitored the output of the various devices. Eltayeb et al. [8] designed a solar-wind hybrid artificial structure that looks like a natural tree in Paradesh, consisting of 2 kW PV and 1 kW wind, they carried out structural optimisations generating 4709 kWh/year with 20% increase due to the use of double axis tracking system.

On the other hand, storage is crucial in terms of energy saving especially in case of intermittent sources like PV and wind. Battery system has been the leading storage system, Choton et al. [9] made a thorough and comprehensive overview regarding the sizing, power quality issues, energy demand, smart charging, optimal ESS placement energy management and operation of ESS. Modern batteries have made significant advancements in terms of energy storage density and discharging efficiency, allowing them to store more energy and release it over a longer period with minimal loss [10]. This is especially important for applications like smartphones, electric vehicles, and renewable energy systems, where high energy storage density and efficiency are crucial for optimal performance and longer operating times [11].

On the other hand, supercapacitors, also known as ultracapacitors or electric double-layer capacitors, are energy storage devices that store and release energy through the movement of ions near the surface of porous carbon electrodes [12]. Unlike regular capacitors, which store energy through the separation of electric charge, supercapacitors store energy in an electrostatic field, resulting in a much higher energy density than conventional capacitors and a much higher power density than batteries [13], some of the main complementary features of battery and SC are listed in table 1. Therefore, combining the two storage systems will relieve the battery and reduce the stress on it. Hajiaghasi et al. [14] reviewed the applications of HESS for microgrid applications, the paper reviewed various HESS configurations, considering storage type, interface, control, and services. It provides insights into capacity sizing

methods, power converter topologies, system architecture, control methods, and energy management in microgrids. Additionally, the paper includes an economic analysis and design methodology, offering perspectives for investors and distribution systems engineers in HESS implementation. Argyrou et al. proposed the mathematical modelling of the battery-SC HESS using MATLAB for PV application, examining two branches model for the SC equivalent circuit added to the dual polarization model consisting of dual RC network used for the battery model. Further modelling analysis was performed in [15], taking the various types of HESS into account (active & passive). In [16] Jing et. al conducted a thorough examination of battery-SC HESS in standalone microgrids, categorizing them into passive, semi-active, and full active configurations. The authors highlighted the distinct characteristics, strengths, weaknesses, and applications of each group. Specifically, the integration of actively controlled components in semi and full active HESS is emphasized, enabling effective power exchange management through Energy Management Systems (EMS). This not only reduces battery stress but also ensures consistent high-power quality and reliability. Some of the limitations highlighted by the authors include the EMS, implementing the system in remote areas, autonomizing the control of the system, comparison between various battery electrolytes alternatives. Apart from the conventional hybrid systems, Zuo et al. [17] proposed the hybridization of a battery and SC as a single entity. The authors named the system "Battery-Supercapacitor Hybrid Device". The device constitutes the electrolyte and SC-electrodes, due to the capacitive electrodes present instead of the conventional battery electrode, the energy density of the device is low. To overcome this issue, capacity improvement is needed as well as voltage expansion. Flexibility and portability are some of the limitations of the device.

Table 1: Key Differences Between Battery and Supercapacitor

Aspect	Battery	Supercapacitor
Energy Density	High (stores more energy per unit volume)	Low (less energy storage capacity)
Power Density	Low (slower energy delivery)	High (quick bursts of energy delivery)
Charge/Discharge Time	Longer (minutes to hours)	Very fast (seconds to minutes)
Cycle Life	Limited (few thousand cycles)	Very high (up to a million cycles)
Response Time	Slow	Extremely fast
Durability	Degrades over time due to chemical wear	Highly durable with minimal degradation
Energy Storage Mechanism	Electrochemical reactions	Electrostatic charge storage
Maintenance	Requires more maintenance	Low maintenance
Cost	Lower initial cost	Higher initial cost
Applications	Long-term energy storage	Short-term power delivery and smoothing

2. Climate features in Madinah

Madinah in Saudi Arabia has a desert climate with extremely high temperatures in summer (above 40°C) and mild winters (15-25°C). Rainfall is scarce, and the city is generally dry. Spring and autumn offer more comfortable temperatures, making them favourable times to visit. For the most accurate and up-to-date weather information, it is recommended to check reliable weather sources.

Located in the western part of Saudi Arabia, is situated at approximately 24.4667° N latitude and 39.60° E longitude. The city's geographical coordinates place it inland, away from the coastal influences, contributing to the arid conditions, marked by sandy terrain and sparse vegetation.

Moreso, according to the "Indicators of Renewable Energy in Saudi Arabia 2017" report, the daily average GHI for the western region, which includes Madinah, was approximately a whooping 5,954 Wh/m²/day in 2017. Similarly, going through the acquired irradiance data from PVGIS as seen in figure 1, the area is highly feasible for solar systems.

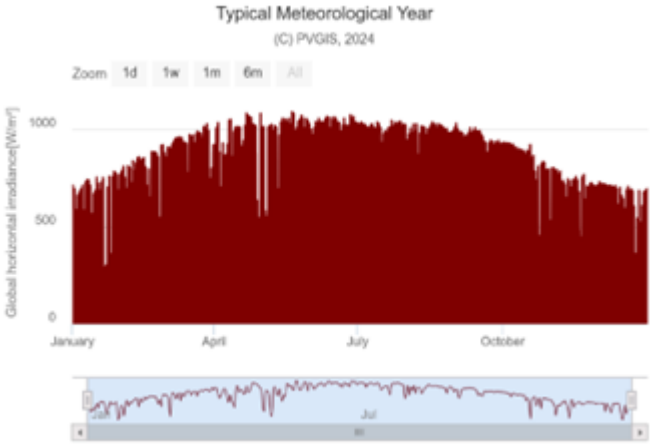

Figure 1: Annual average irradiance.

Similarly, the region has a considerable amount of windspeed with some seasonal variations, figure 2 shows the average wind speed of the region for every month across the period of 15 years. The average wind speed is around 4.5-5 m/s, with some peaks at March-May. In general, during winter, the region experiences constant and reliable wind speed of about 4 m/s. Therefore, due to facts mentioned above, the study can be carried out at the region effectively.

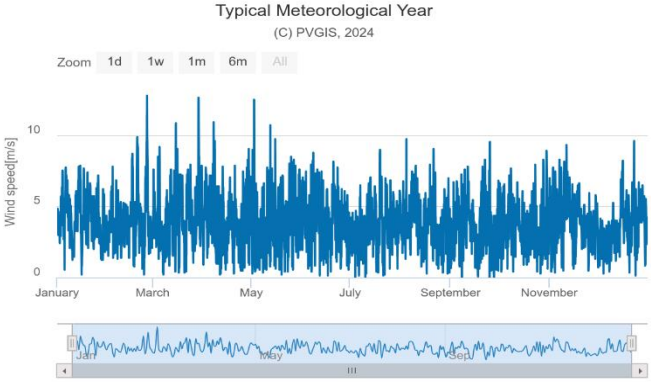

Figure 2: Average annual wind speed.

3. Materials & Methodology

The research starts by analysis of the climatic characteristics of the city of Madinah. The meteorological data of the area used for the analysis was obtained through PVGIS ranging from 2005-2020. To analyse the availability of energy production through the hybrid system, the data in table 1 was used for the area. To ensure the smooth working of the system and to observe its performance, MATLAB was used to simulate the separate systems, after then the systems were combined. To be more realistic, the irradiance fed to the PV model was made variable using the signal builder, the same scenario for wind speed as in the case of wind turbine, figure 3 illustrates the variables. Furthermore, in observing the effect of the storage systems on the DC bus, four cases of different configurations were carried out.

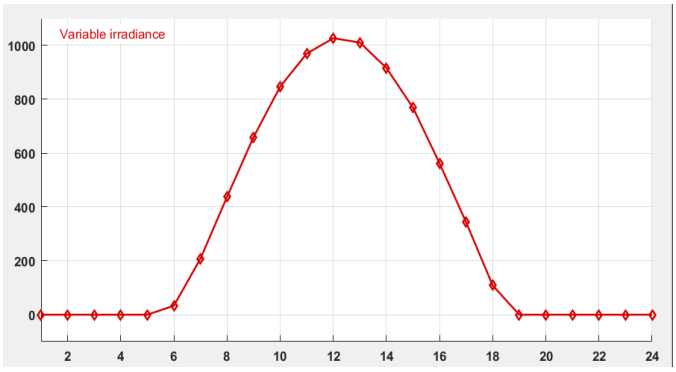

Figure 3a: Daily variable irradiance.

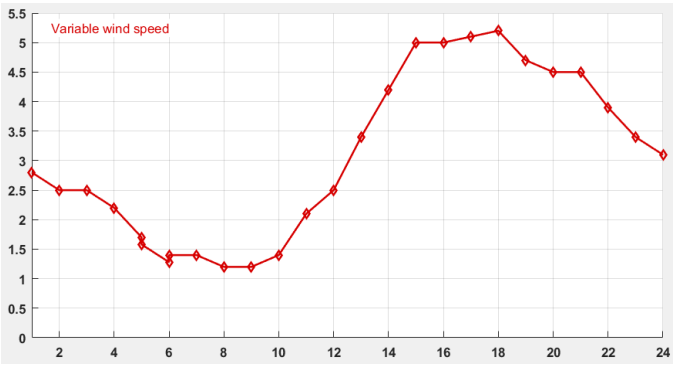

Figure 3b: Daily variable wind speed.

Table 2: Metrological data for the subjected area.

Month	Monthly average wind speed (m/s)	Average irradiance per day (kWh/m^2)
January	5.1	192.16
February	4.8	196.92
March	4.5	229.25
April	4.7	217.35
May	3.5	217.77
June	2.9	213.59
July	3.3	220.10
August	3.2	218.09
September	2.9	216.64
October	4.1	216.73
November	4.6	192.02
December	5.45	188.42

4. System design

For the PV module, JA Solar (JAM72S20-455/MR) is used for the simulation. The module has a characteristic of 455 W, 49.85 V, and 11.41 A as peak power, open circuit voltage and short circuit respectively. As for the wind system, 1 kW AEOLOS vertical wind turbine was considered for the simulation. The turbine has a peak power of 1500 W, a start-up speed of 1.5 m/s and generator efficiency of 0.96. The combination of these two systems is expected to give a reliable power that can be harnessed even during low production of one of the sources, hence they are complementary.

The system contains various power converters. A rectifier circuit was used to rectify the voltage from the wind turbine. Moreso, boost converter was used to boost the PV voltage as well as the rectified voltage from the wind. After merging the two system at the DC bus, the bus was connected to an inverter for DC-AC conversion, figure 4 shows the basic system configuration. The storage was also connected to the DC bus for four cases: no storage, battery only, then SC only, and lastly their combination.

Storage is needed to store the energy especially during peak times to be utilized during off-peak to compensate the load or during autonomy days. The system is using battery as the main storage, and the SC as a subordinate entity due to the already mentioned advantages. The battery is of 48 V and a 400 Ah, while the SC is 16.2 V and a capacity of 65 F.

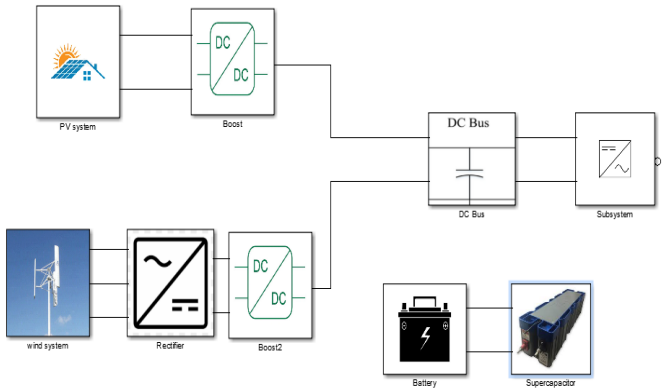

Figure 4: System configuration.

5. Simulation Results

Case 1: No storage; For the first case there was no storage attached to the system entirely. This is done, to really observe how the system will behave if the hybrid system is supplying energy directly to the load. Figure 5 shows the PV voltage as it changes due to the variable irradiance values.

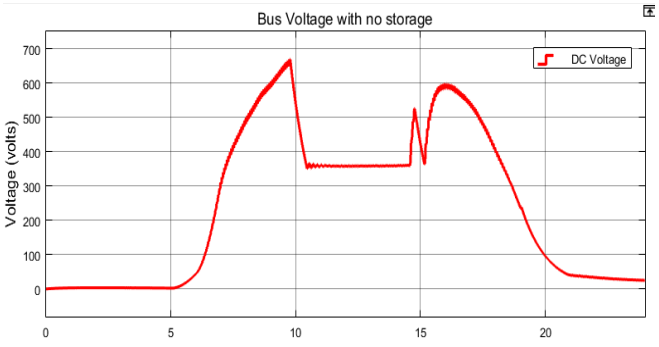

Figure 5: Bus voltage before any storage.

Case 2: During the second case, the hybrid system is connected to the battery system, which is the preferable storage system, see figure 6a. Because of this connection, the DC bus voltage will surely reduce because the battery will be charging as well. But before the charging starts, discharging will occur because the battery will be sole source to the DC bus due to low or absence of generation from the hybrid system, see figure 6b.

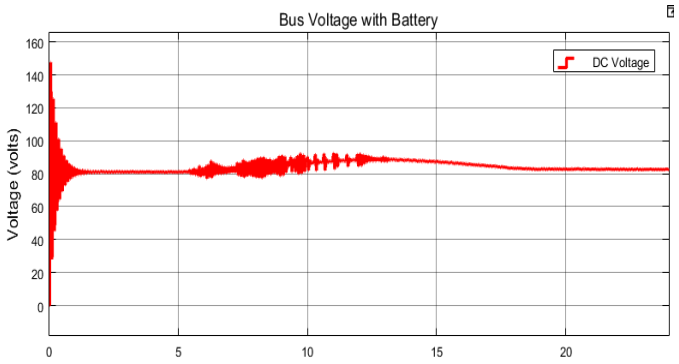

Figure 6a: Bus voltage after connecting the battery.

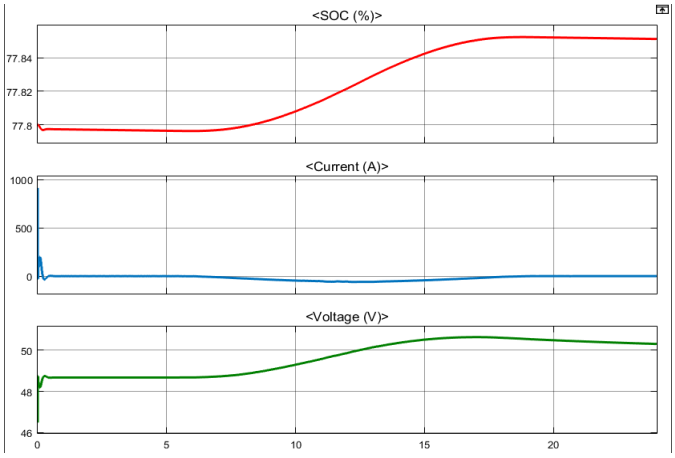

Figure 6b: Battery characteristics after connecting to the HRES.

Case 3: Here, the system is connected to the SC, for the observation. The behaviour of the system is shown in figure 7a. Since SC is another storage system, it is expected that similar behaviour for case 2 to occur, though with considerable variations due to differences in characteristics, figure 6b confirms this.

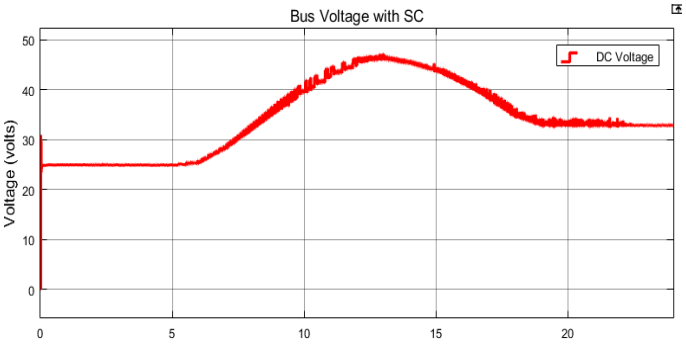

Figure 7a: DC bus after connecting the SC.

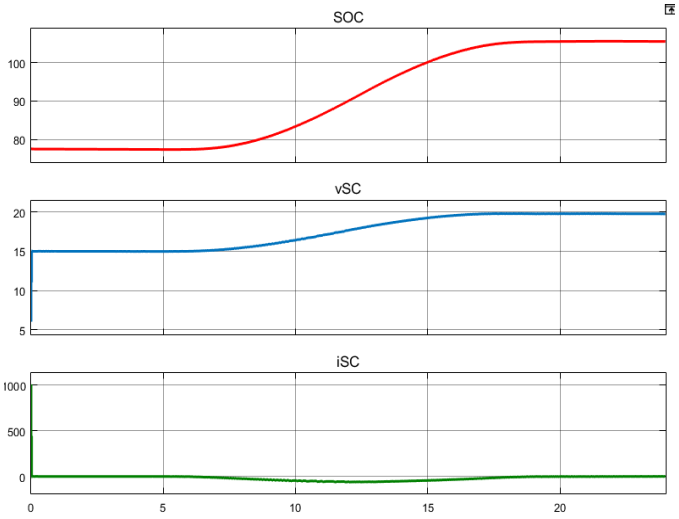

Figure 7b: SC characteristics after connecting to the HRES.

Case 4: Finaly the two storage systems were combined, as seen from figure 8. Here the two hybrid systems (generation and storage) are integrated. As illustrated by the figure, the integration ensures more voltage stability across the DC bus. With regards to the storage state of charge of the two systems, the SC charges faster than the battery, it was observed the SC charged by 25%, whereas the battery only charged for 0.1 %. Likewise, during the discharging phase, the battery shows discharge rate of 1.28e-3% compared to 0.5% of the SC.

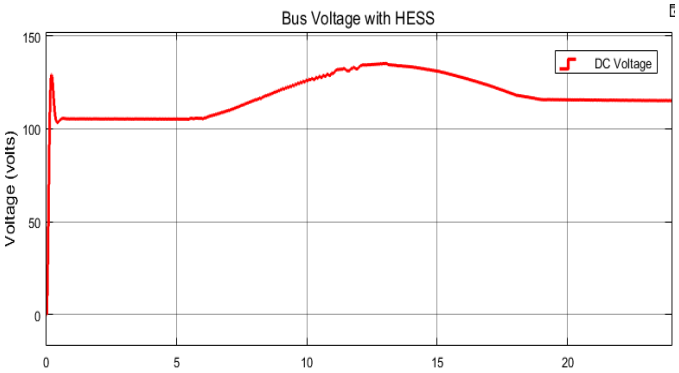

Figure 8a: Bus voltage after integration HRES with HESS.

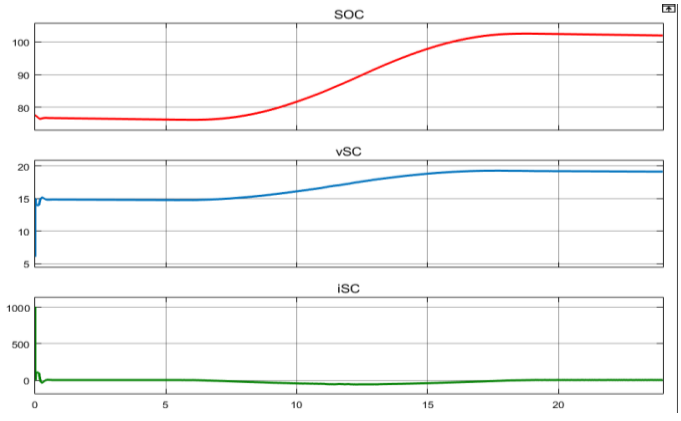

Figure 8b: SC characteristics.

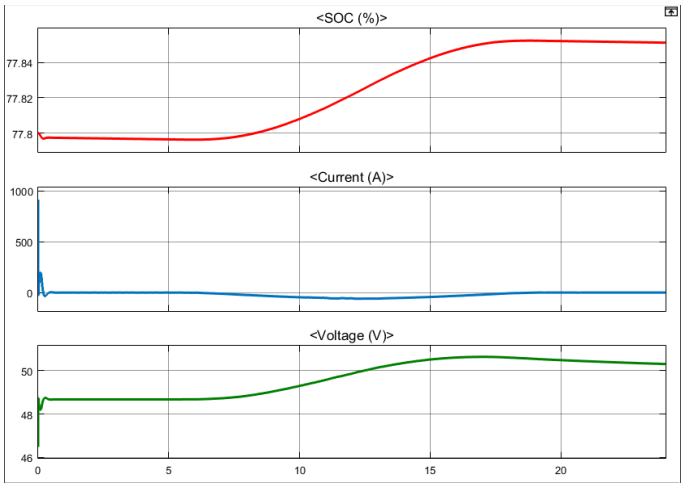

Figure 8c: Battery characteristics.

6. Advantages and Limitations of HESS

Supercapacitors handle high power demand and rapid charge/discharge cycles, while batteries provide long-term energy storage. This synergy improves system efficiency. This reduces the stress on batteries during peak loads, minimizing wear and prolonging battery lifespan. Moreso, SC deliver quick bursts of energy, enhancing the system's responsiveness to sudden power demands. The combination allows better handling of energy fluctuations, ensuring stable and reliable power output [11].

Some of the limitations include an increased complexity. Managing two storage technologies requires advanced control systems, increasing design complexity. Consequently, this makes the system to raise the initial investment. Also, SC have lower energy density compared to batteries, making them unsuitable for long-term energy storage alone. In addition, efficiently integrating the two systems requires careful planning to balance power and energy demands [14].

7. Conclusion

The hybrid generation system integrated with the hybrid storage is a crucial method for an established reliable power system. Hybrid generation provide a complementary scenario for power generation; hence energy will be available considerably during the entire hours of the day. Meanwhile, the solar provides much energy. This implies that the energy generated during the day will be much higher than the night hours since only the wind turbine will be in action. And as already seen from the wind speed data, the wind is also less during the night.

On the other hand, combining the two storage systems relieves the battery from the inevitable stress, as such increasing its life span considerably. This happens due to the higher power density of the SC and high energy density of the battery. In all the four scenarios, the voltage of the DC bus is optimal considerably. According to the observations made from the various scenarios shows that the integration of the hybrid generation with the hybrid storage presents more promising results. Simulations results show that the voltage across the DC bus is stabilized. Similarly, much stress is relieved from the battery by the SC.

In addition, according to the observed results from the simulation, the region is climatically and metrologically feasible for the hybridization of solar energy with the wind energy. Nonetheless, carrying out the economic feasibility analysis is crucial for the hybrid development in the region. It is suggested that the hybrid storage system should also be included in the studies.

References

[1] V. Khare, S. Nema and P. Baredar, "Solar–wind hybrid renewable energy system: A review," *Renewable and Sustainable Energy Reviews,* vol. 58, pp. 23-33, 2016.

[2] H. Shahinzadeh, S. H. Fathi, A. Gheiratmand and l. Moradi, "Optimal Design and Management of Isolated Hybrid Renewable Energy System (WT/PV/ORES) A Case Study of Kish Island," in *21 sl Electrical Power Distribution Conference*, Karaj- Alborz- Iran, 2016.

[3] M. Deshmukh and S. Deshmukh, "Modeling of hybrid renewable energy systems," *ScienceDirect,* vol. 12, pp. 235-249, 2008.

[4] D. Rekioua, "Hybrid Renewable Energy Systems Overview," *Green Energy and Technology,* pp. 5-34, 2020.

[5] A. Kamal, B. Mohsine, A. Abdelali and A. A. Ben, "Sizing methods and optimization techniques for PV-wind based hybrid renewable energy system: A review," *Renewable and Sustainable Energy Reviews,* vol. 93, pp. 652-673, 2018.

[6] B. A. S. Al, K. H. A, A.-B. A. H and K. M. Farooq, "A review of optimum sizing of hybrid PV–Wind renewable energy systems in oman," *Renewable and Sustainable Energy Review,* vol. 53, pp. 185-193, 2016.

[7] S. Angadi, U. R. Yaragatti, Yellasiri and A. B. Raju, "Comprehensive Review on Solar, Wind and Hybrid Wind-PV Water Pumping Systems-An Electrical Engineering Perspective," *CPSS Transactions on Power Electronics and Applications,* vol. 6, no. 1, 2021.

[8] W. A. Eltayeb, J. Samhal, S. Kumar and S. K. Rao, "Design and analysis of asolar-wind hybrid renewable energy tree," *Results in Engineering,* vol. 17, no. 100958, 2023.

[9] s. o. a. p. q. Overview of energy storage systems in distribution networks: Placement, "Overview of energy storage systems in distribution networks: Placement, sizing, operation, and power quality," *Renewable and Sustainable Energy Reviews,* vol. 91, pp. 1205-1230, 2018.

[10] B. Dunn, H. Kamath and J.-M. Tarascon, "Electrical Energy Storage for the Grid: A Battery of Choices," *Materials for Grid Energy,* vol. 334, 2011.

[11] M. Faisal, M. A. Hannan, P. J. Ker, A. Hussain, M. B. Mansor And F. Blaabjerg, “Review of Energy Storage System Technologies in Microgrid Applications: Issues and Challenges,” *IEEE Access,* 2018.

[12] A. P. Moholkar, D. S. Bankar and P. B. Karandikar, “Supercapacitor based cost effective hybrid energy storage system with reduction in battery size for diesel generator cold cranking,” *Indonesian Journal of Electrical Engineering and Computer Science,* vol. 31, no. 1, pp. 22-32, 2023.

[13] N. J. Dudney, W. C. West and J. Nanda, Handbook of Solid State Batteries, New York: World Scientific, 2015.

[14] S. Hajiaghasi, A. Salemnia and M. Hamzeh, “Hybrid energy storage system for microgrids applications: A review,” *Journal of Energy Storage,* vol. 21, pp. 543-570, 2019.

[15] K. M. Moloelang, P. F. L. Roux and B. T. Abe, “Modeling and Analysis of a Battery-Supercapacitor Hybrid Energy Storage System (HESS) for Renewable Energy Applications,” *Sustainable Energy Grids and Networks,* 2023.

[16] W. Jing, C. H. Lai, S. H. W. Wong and M. L. D. Wong, “Battery-supercapacitor hybrid energy storage system in standalone DC microgrids: a review,” *Institution of Engineering and Technology Journals,* vol. 11, no. 4, pp. 461-469, 2016.

[17] W. Zuo, R. Li, Y. Li, J. Xia and J. Liu, “Battery-Supercapacitor Hybrid Devices: Recent Progress and Future Prospects,” *Advanced Science News,* vol. 4, 2017.

Evolution and Impact of Machine Learning Techniques on Dynamic Job Shop Scheduling

BELMAMOUNE Manal Abir

Manufacturing Engineering Laboratory of Tlemcen (MELT)

University of Tlemcen
Tlemcen, Algeria
manalabir.belmamoune@univ-tlemcen.dz

YAHOUNI Zakaria

Sciences of Conception, Optimization and Production (G-SCOP)

University of Grenoble Alpe, CNRS
Grenoble, France
zakaria.yahouni@grenoble-inp.fr

GHOMRI Latéfa

Manufacturing Engineering Laboratory of Tlemcen (MELT)

University of Tlemcen
Tlemcen, Algeria
latefa.ghomri@univ-tlemcen.dz

***Abstract*— With the emergence of new technologies in artificial intelligence, researchers from various industrial sectors are integrating these innovations to solve the challenges encountered in the manufacturing domain. In this paper, we review the application of Machine Learning in Job Shop Scheduling problems within the presence of uncertainties and dynamic events such as machine breakdowns and random job arrivals.**

Keywords*— *Dynamic Scheduling, Job Shop, Machine Learning, Uncertainties

I. INTRODUCTION

Scheduling is a decision-making process that is used regularly in many real-life situations. It involves the allocation of resources to tasks over time, with the goal of optimizing one or several objectives [1]. In the manufacturing sector, task scheduling plays an essential role in the success of a production company. It promotes optimal use of resources, enables adherence to product due dates, reduces costs, and improves product quality. The difficulty of finding optimal schedule depends on the shop environment, the process constraints and the performance indicator [2] Although, manufacturing scheduling is frequently impacted by various uncertainties, including machine breakdowns can lead to the failure of the initial schedule. That is the reason why companies prefer to have robust schedules capable of adapting to changes without deteriorating too much the performances, rather than optimal schedules. One of the most complicated and studied workshops' scheduling is the Job Shop configuration. It is classified as a combinatorial NP hard problem and consists of scheduling jobs/products with different rooting on different machines. It involves scheduling jobs/products with different routings on different machines. This type of workshop is found in companies producing customized products and is referred to as the Job Shop Scheduling Problem (JSSP).

Due to the complexity of this problem and dynamic events occurring in real-world cases, researchers have proposed robust scheduling methods. Motivated by their industrial applications, these methods seek either to integrate a priori uncertainty models into scheduling or to correct schedules using reactive algorithms while avoiding performance deterioration [3].

Recently, Artificial Intelligence, particularly Machine Learning (ML), has been used for JSSP due to its capability to adapt to changes.

This paper investigates these research efforts by addressing the evolution of solving JSSP from basic methods under uncertainties to advanced ML techniques, emphasizing the significance of Reinforcement Learning (RL) techniques as widely used methods in this field. In section II we define the JSSP environment and the dynamic events that can occur. In section III we remind some basic scheduling methods before addressing artificial Intelligence methods in Section IV. Conclusions and perspectives are addressed in the last sections.

II. JOB SHOP SCHEDULING PROBLEM

The job shop scheduling problem (JSSP) is a combinatorial optimization challenge that involves assigning jobs to machines in a manufacturing environment. Each job consists of a sequence of operations that must be processed on specific machines, with constraints such as processing times and machine availability [4].

In a Job Shop, we have a set of n Jobs: $\{J_1, J_2, J_3, \dots, J_n\}$, that represent the products we want to manufacture, each job has its operations: $J_i = \{O_{i1}, O_{i2}, O_{i3}, \dots O_{ij} \dots, O_{im}\}$ with $i \in \{1, n\}$, $j \in \{1, m\}$ and m is the number of operations executed in m machines: $\{M_1, M_2, M_3, \dots, Mm\}$ [5]. Different objectives can be optimized, such as minimizing total completion time of all Jobs, tardiness, or other performance metrics.

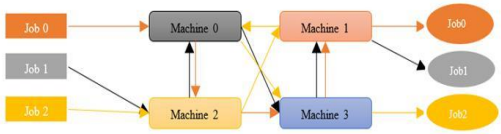

Figure 1: Job Shop example (3 jobs and 4 machines)

As shown in figure 1, each job has its own sequence of operations. This could lead to conflicts in the machine queue, and the choice of which job to run in one machine could have an impact on the completion time of the others.

The Dynamic Job Shop Scheduling Problem (DJSP) extends this complexity by incorporating real-time changes or dynamic events, such as new job arrivals or machine breakdowns [6], making it challenging to ensure both robustness and stability in performance and necessity. The uncertainties encountered in the real world have driven the

need to establish robust schedules that can withstand disturbances.

A. Dispatching Rules

A dispatching rule is used to select the next job to be processed from a set of jobs awaiting at the same machine [7]. The most well-known rules are:

- **SPT (Shortest Processing Time):** Highest priority is given to the waiting operation with the shortest imminent operation time.
- **LPT (Longest Processing Time):** Highest priority is given to the waiting operation with the longest imminent operation time.
- **MWKR (Most Work Remaining):** Highest priority is given to the waiting operation associated with the job having the most total processing time remaining to be done.
- **LWKR (Least Work Remaining):** Highest priority is given to the waiting operation associated with the job having the least amount of total remaining processing time.
- **TWORK (Total Work):** Highest priority is given to the job with the least total processing requirement on all operations.
- **FIFO (First In First Out):** Highest priority is given to the waiting operation that arrived at the queue first.
- **LIFO (Last In First Out):** Highest priority is given to the waiting operation that arrived at the queue last.
- **EDD (Earliest Due Date):** highest priority given to jobs with the closest due date.

The advantage of these dispatching rules is their simplicity and rapidness in obtaining feasible solutions. However, the obtained solution is not guaranteed to be optimal. To improve their efficiency, a combination of dispatching rules can yield better results [8].

B. Heuristics and metaheuristics.

These are approximate approaches to solving optimization problems. They are not guaranteed to find the ideal solution, but generally offer a satisfactory solution within a reasonable timeframe. [9] used the Bottleneck Resource(s) (BR) heuristic to solve a DJSP. BR(s) is machine(s) which prevent better function of the system. the development of an efficient approach to identify and assess BR(s) in Multi-objective Dynamic Job Shop has been considered as the subject of this paper. [10] develop a heuristic which combine the difference dispatching rules and a simulation technic to solve a DJSP. Another heuristic used by [11] which is the Rolling Horizon heuristic. It was presented for large job shops, in which the total weighted tardiness must be minimized. The method divides a given instance into a number of subproblems.

Another used method in the DJSP are the metaheuristics. The most used one is the Genetic Algorithm (GA) [12]. Genetic algorithms have been proven to be an effective scheduling method. However, simple genetic algorithms have slow convergence and are prone to premature convergence. In order to improve the convergence speed, many researchers focus on combining genetic algorithms with local search schemes to develop some hybrid optimization strategies for JSSP [2]

There is also a Tabu Search Algorithm (TS) which is one of the most effective metaheuristics for solving the JSSP [13].

III. Artificial Intelligence

With the emergence of Artificial Intelligence (AI) techniques and satisfactory results in various fields (facial recognition, image processing, autonomous driving, etc.), researchers in the field of manufacturing in general and workshop scheduling in particular have attempted to apply these techniques to scheduling problems.

Machine Learning (ML) is one of the AI technics where we can use a machine or a robot to teach it to carry out tasks in the same way - more or less - as a human being. There are three types of ML technics, the Supervised Learning (SL), Unsupervised Learning (UL) and the Reinforcement Learning (RL). There is also a Deep Learning (DL) technic which is a branch of ML based on the neural network model.

A. Supervised Learning:

In supervised learning, data is needed to train these learning models. A set of input examples along with their corresponding desired outputs are provided to build a model. The model's learning accuracy is significantly impacted by the accuracy of the data. For this reason, a number of studies employed optimization techniques to solve the JSSP before using the optimal schedule data as a foundation for supervised techniques [14]. A limited number of researchers in the literature have made contributions to the DJSP through the use of SL. [15] proposed the integration of Supervised Learning, wherein the optimal target schedules generated can serve as training data within the suggested framework, enabling the acquisition of learned behaviors from new datasets. This approach was deemed more effective as it achieved convergence more rapidly than unsupervised methods. This article elaborated on how their Deep Neural Network (DNN) were trained using the best schedules determined by a Mixed Integer Problem (MIP) solver, allowing the model to learn from labeled data and deliver near-optimal solutions. The same authors [16] contributed in the DJSP by using both SL and RL. The RL was in charge to develop a scheduling policy for job assignments. Subsequently, the trained RL agent will generate datasets by implementing various permutation strategies on the job sequences. This process involved modifying the original job sequences to create a range of training scenarios, thereby facilitating the assessment of the RL agent's generalization abilities. New policies have been developed using these permuted datasets in a supervised learning framework. To bolster the resilience of the learned policies, the authors integrate regularization methods from the supervised learning field, including dropout layers, which assist in mitigating overfitting and enhancing generalization.

B. Unsupervised Learning

In contrast to the previous approach, unsupervised learning does not rely on a predefined output. Instead, the machine employs clustering and feature detection algorithms to develop a model. This type is the less used in a DJSP. For example, we have the work of [17] who addressed the challenges posed by volatility and digitalization, manufacturing companies must create an effective

production plan that aligns with customer demand and their manufacturing capabilities. This study employed a self-organizing map, an unsupervised clustering algorithm, to group similar data from the dataset, subsequently deriving micro-regression models to establish a sustainable process. Previous research in this domain has primarily concentrated on the development of macro-models that consider factors associated with job characteristics, shop characteristics, and order characteristics.

C. Reinforcement Learning

When we talk about a dynamic environment such as a DJSP the most suitable machine learning algorithm that can be used is the Reinforcement Learning. According to the studies applied by [18], the RL is the more used technics in production scheduling and planning. RL are processed as a Markovian Decision Process (MDP) consists of autonomous agents that learn to choose appropriate actions/decisions in a state (workshop configuration at a specific time for example) to achieve their goals by interacting with the environment to maximize reward signals [5].

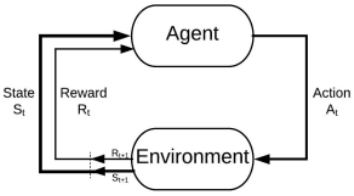

Figure 2 Reinforcement Learning presentation

1) Q-Learning (QL):

It is one of the basic, yet classic algorithms. Q-learning considers a *Q*-function, where Q designates quality and it is associated with the state and the action [19]. The Q-value based on the observed reward and the estimated future value will be updated at each time using the bellman equation as shown in Eq (1).

$$Q(st,at) = Q(st,at) + \alpha\,.[rt + \gamma\,.max\,a\,Q(st+1,a) - Q(st,at) \quad (1)$$

The Q vales of each state-action pair will be memorized in a Q-table. At the end of the learning, the filled Q-table will be used to choose the best action in each state.

Most recent work introduces the notion of the dynamic workshop to give a realistic picture of the problem. [20] considered a dynamic and flexible JSSP model with limited transportation resources, aiming to minimize delivery time and overall energy consumption. Considering three types of disruptions (order cancellation, machine failure, and AGV failure), corresponding event-driven rescheduling strategies are proposed, and a rescheduling instability index is developed to measure the performance of the rescheduling strategy. A *Q*-learning was proposed, by learning the feedback of historical search experience, it adaptively selects the appropriate neighborhood structure for local search; and a hybrid initialization strategy was developed according to the problem characteristics to improve the optimization performance of the algorithm. To solve DFJSP with double-shift action, [21] proposed an improved Q-learning. The initial scheduling scheme is obtained by a Genetic Algorithm, and the rescheduling strategy is determined by the proposed Q-learning agent according to the scheduling rule. When a machine fails, the Q-learning agent is able to optimally select the operation and the replacement machine.

The Q-learning algorithm, while commonly utilized in previous years prior to the advent of neural networks, is restricted to a limited range of applications. This limitation arises primarily from its significant drawback: the inability to learn directly in environments characterized by continuous states and actions, as it relies on finite-size tables for its processing [19].

2) Deep Q-Learning/ Deep Q- network (DQL/DQN) :

It is a RL technique that combines Q learning and Neural Networks (NNs). All the concepts associated with Q learning (e.g. the Bellman equation) still apply to DQN, except for one fundamental difference, which is the use of function approximators, in particular NNs instead of tabular storage (Q-table) for the Q-values.

Many authors use DQN to solve a DJSP. The contributions consist of finding a suitable representation of the dynamic environment to the DQN agent and the reward function.

A scheduling solution for the DJSP was proposed by [22] utilizing the DQN method, which is capable of functioning effectively amidst dynamic events. The scheduling state at each iteration was represented as a vector, derived from the established state features, and serves as input for the scheduling agent. This transforms the problem into a sequential decision-making challenge by altering the execution order. Stochastic elements are incorporated into the environment through the rearrangement of job sequences assigned to machines and the variation of job processing times. The action space for the DRL is defined by the number of jobs that can be scheduled within a complex environment.

1) Proximal Policy Optimization (PPO):

PPO gathers small batches of experiences, consisting of state, action, reward, and next state, during its interaction with the environment, which are then utilized to refine its policy. After the policy has been updated, a new batch is collected based on this revised policy. A key aspect introduced by PPO is the notion of a trust region, which ensures that any new policy update does not deviate excessively from the preceding policy. This approach leads to reduced variance and more stable training, thereby preventing the agent from straying into an irretrievable trajectory [19]. [23] addressed a novel dynamic adaptive scheduling system employing deep reinforcement learning to address unforeseen circumstances in real-world settings. To tackle the challenges posed by the expanding dimensions of the state and action space associated with the disaster problem, the PPO algorithm was implemented, significantly mitigating complexity while ensuring effective performance. [24] used the PPO in conjunction with hybrid prioritized experience replay to solve a DJSP. The job shop scheduling challenge was framed as a sequential decision-making issue within the context of Markov Decision Process. A unique state representation was developed, derived from the feasible solution matrix that

illustrates the scheduling sequence of tasks. Additionally, a collection of paired priority dispatching rules was employed as the actions, and a novel, intuitive reward function was introduced, focusing on the idle time of machines.

2) Multi-Agent Approach:

The multi-agent Approach represents a newly embraced methodology in the field of RL. It consists of a group of agents that acquire knowledge within a common environment by utilizing one of the reinforcement learning algorithms previously discussed.

[25] developed a tool for JSSP, which works with the Q-learning algorithm and can be adapted to different scheduling scenarios using multi-agents where each agent is in charge of a task in the workshop. [26] developed a new model for a dynamic scheduling system utilizing multi-agent technology, incorporating agents for machines, buffers, states, and jobs. To identify the most appropriate operations and enhance production efficiency, a weighted Q-learning algorithm that employs clustering and dynamic search techniques was implemented. In order to tackle the challenges posed by the extensive state space resulting from variations in the system state, four distinct state features were identified. The dimensionality of the system state was reduced through the application of the clustering method. [27] proposed a distributed and self-adaptive scheduling algorithm, which utilizes Q-learning for real-time dynamic allocation of tasks across multiple task flows. This algorithm was designed to autonomously adjust to the task arrival process for individual task flows, while also taking into account the influence of other agents on the overall task flows. [28] proposed a methodology that addresses the dynamic scheduling challenges faced in Job Shop workshops with stochastic jobs' arrivals. It entails the collaboration of multiple agents who collectively engage in real-time scheduling decisions, allowing for adjustments in response to fluctuations within the workshop environment.

[8] introduced an approach based on deep multi-agent reinforcement learning to tackle the dynamic job shop scheduling issue. The double deep Q-network algorithm, linked to decentralized scheduling agents, was employed to understand the connections between production data and scheduling goals, enabling near real-time scheduling decisions and a specialized state and action representations that can tackle size-agnostic scheduling tasks, which are scalable in dynamic environments.

In all the works mentioned above, each author made interesting contributions in the adaptation and implementation of the algorithm. The most varied factors from one author to another when talking about reinforcement learning algorithms are the way of representing the state of the environment that will provide precise information about the environment to the agent. We also have an action space; some authors have defined the job to be done soon as an action chosen by the agent. Other authors have chosen dispatching rules as actions to be applied in the queue of the concerned machine to select tasks to be executed earlier.

Another very important parameter in the reinforcement learning algorithm is the choice of the reward function. This value represents a signal that guides the agent to take the right action in the current state, so it is of great importance.

If we talk about the DJSP environment, the magnitude of the workshops or the cases where we apply the algorithm varies. The application of these techniques in a large and uncertain environment has a great influence compared to small workshops. For scheduling problems, we have several parameters to optimize, the most discussed in the works cited above is the optimization of the completion time which represents the end of all the assignment tasks in the workshop. We have also the minimization of the number of delays and energy consumption. Table 1 resumes the Reinforcement Learning cited contributions.

Table 1: Classified contributions in term of algorithm, Objective function and dynamic event

Author	algorithm	objective function	dynamic event
Martínez & al	Multi agent Q-Learning	makespan and tardiness	Machine breakdowns Varying activity duration
Wang & al	Multi agent Q-Learning	Average tardiness-earliness	Job arrivals
Xiao & al	Multi agent Q-Learning	flow time	Job arrivals
İnal & al	Multi agent simulation scenarios	tardy jobs tardiness, earliness, flow time and makespan	job arrivals
Wu & al	Multi agent PPO	makespan and tardiness	processing time
Liu & al	Multi agent Deep Q Learning	tardiness	job arrivals
Workneh & al	Deep Q network	makespan	processing time machine breakdown
Wang et al	Multi agent PPO	makspan	machine breakdown and job rework
Zhao et al	Q-Learning Genetic Algorithm	tardy jobs	Machine breakdown
Chen et al	Q-Learning	makespan and total energy consumption	job cancellation, machine breakdown, AGV breakdown

Figure 3 shows the used algorithms in the DJSP from 2023 to now in different databases by applying the query that combines the desired algorithm and "dynamic job shop scheduling problem". The DQN algorithm has emerged as the

most widely utilized method in recent times, primarily due to its effectiveness across various domains, including video gaming and autonomous driving. Its adaptability is further enhanced by the availability of diverse neural network libraries, making it accessible for authors to implement in their projects. Following closely is the Q-learning algorithm, particularly when applied in a multi-agent context. This approach has proven to be highly successful in the domain of DJSP, as authors assign a learning agent to each component in the workshop such as machines, AGVs, and products allowing these agents to collaborate for more reliable outcomes. Q-learning is recognized as one of the simplest reinforcement learning algorithms to implement, which contributes to its popularity among researchers. The integration of multi-agent systems with Q-learning facilitates rapid adaptation and effective solutions to the challenges being addressed.

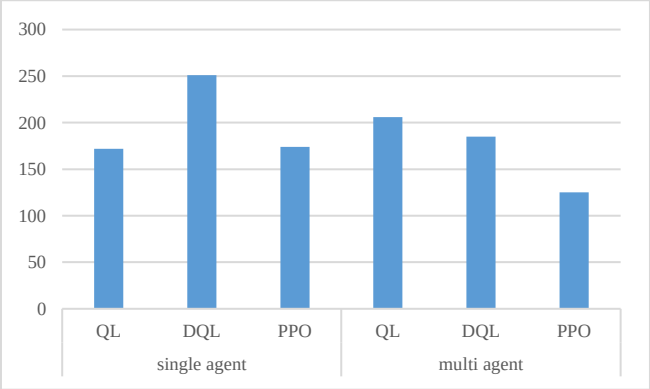

Figure 3: statistics of the use of RL algorithms from 2023 to now

IV. Conclusion

In our paper, we focus on the Job Shop Scheduling problem in dynamic environment by reviewing related contributions in this type of workshop, in order to obtain a robust schedule. Scheduling robustness is a major challenge for researchers in this field, prompting them to propose advanced approaches to obtain satisfactory results. We explored Machine Learning methods, with a particular emphasis on work related to reinforcement learning algorithms, which have recently become the most commonly used in the literature. This approach is particularly suited to this type of problem, especially when it comes to reel-time decision making. Among the perspectives of this research, we plan to apply these algorithms in a stochastic and uncertain real environment and to evaluate their effectiveness.

References

[1] Y. Martínez Jiménez, *A Generic Multi-Agent Reinforcement Learning Approach for Scheduling Problems*. [En ligne]. Disponible sur: www.vubpress.be

[2] R. Qing-Dao-Er-Ji et Y. Wang, « A new hybrid genetic algorithm for job shop scheduling problem », *Comput. Oper. Res.*, vol. 39, nº 10, p. 2291-2299, oct. 2012, doi: 10.1016/j.cor.2011.12.005.

[3] Z. Yahouni, N. Mebarki, et F. Belkadi, « Human-machine cooperation in planning and scheduling: a case study on an unstable environment », 2018.

[4] G. Bonetta, D. Zago, R. Cancelliere, et A. Grosso, « Job Shop Scheduling via Deep Reinforcement Learning: a Sequence to Sequence approach », août 2023, [En ligne]. Disponible sur: http://arxiv.org/abs/2308.01797

[5] M. Belmamoune, L. Ghomri, et Z. Yahouni, « Solving a Job Shop Scheduling Problem Using QLearning Algorithm », *International Workshop on Service Orientation in Holonic and Multi-Agent Manufacturing*, p. 196-209, 2 février 2023.

[6] O. Holthaus, « Scheduling in job shops with machine breakdowns: an experimental study ».

[7] R. Hunt et M. Zhang, « Evolving Dispatching Rules with Greater Understandability for Dynamic Job Shop Scheduling Mark Johnston ».

[8] R. Liu, R. Piplani, et C. Toro, « A deep multi-agent reinforcement learning approach to solve dynamic job shop scheduling problem », *Comput. Oper. Res.*, vol. 159, nov. 2023, doi: 10.1016/j.cor.2023.106294.

[9] N. Nahavandi et M. Abbasian, « An Efficient Approach for Bottleneck Resource(s) Detection Problem in the Multi-objective Dynamic Job Shop Environments », *Int. J. Eng.*, vol. 29, nº 12, déc. 2016, doi: 10.5829/idosi.ije.2016.29.12c.08.

[10] P. D. D. Dominic, S. Kaliyamoorthy, et M. S. Kumar, « Efficient dispatching rules for dynamic job shop scheduling », *Int. J. Adv. Manuf. Technol.*, vol. 24, nº 1-2, p. 70-75, 2004, doi: 10.1007/s00170-002-1534-5.

[11] M. Singer, « Decomposition methods for large job shops », 2001.

[12] Q. D. E. J. Ren, Y. Wang, et X. Si, « An improved genetic algorithm for job shop scheduling problem », in *Proceedings - 2010 International Conference on Computational Intelligence and Security, CIS 2010*, 2010, p. 113-116. doi: 10.1109/CIS.2010.32.

[13] J.-P. Watson, L. D. Whitley, et A. E. Howe, « A DYNAMIC MODEL OF TABU SEARCH FOR THE JOB-SHOP SCHEDULING PROBLEM ». [En ligne]. Disponible sur: www.ms.ic.ac.uk/info.html

[14] A. Hosseini, Z. Yahouni, et M. Feizabadi, « Scheduling AIV transporter using simulation-based supervised learning: A case study on a dynamic job-shop with three workstations », in *IFAC-PapersOnLine*, Elsevier B.V., juill. 2023, p. 8591-8597. doi: 10.1016/j.ifacol.2023.10.032.

[15] J. Schmidt et S. Stober, « Approaching Scheduling Problems via a Deep Hybrid Greedy Model and Supervised Learning », 2021. [En ligne]. Disponible sur: www.github.com/johSchm/deep-hybrid-greedy-scheduling-model

[16] C. Schmidl, T. D. Simão, et N. Jansen, « A Supervised Learning Approach to Robust Reinforcement Learning for Job Shop Scheduling », in *International Conference on Agents and Artificial Intelligence*, Science and Technology Publications, Lda, 2024, p. 1324-1335. doi: 10.5220/0012473600003636.

[17] V. Thiagarajan, R. Rajkanth, C. Rajendran, et T. N. Srikantha Dath, « Machine Learning Algorithm to Solve Dynamic Jobshop Problem to Deal with Digitalization of Manufacturing Process—A Real-World Case Study », in *Recent Advances in Industrial and Systems Engineering*, S. G. Ponnambalam, P.

Damodaran, N. Subramanian, et J. Paulo Davim, Éd., Singapore: Springer Nature Singapore, 2024, p. 225-235.

[18] A. Esteso, D. Peidro, J. Mula, et M. Díaz-Madroñero, « Reinforcement learning applied to production planning and control », *Int. J. Prod. Res.*, vol. 61, nº 16, p. 5772-5789, 2023, doi: 10.1080/00207543.2022.2104180.

[19] M.-A. Chadi et H. Mousannif, « Understanding Reinforcement Learning Algorithms: The Progress from Basic Q-learning to Proximal Policy Optimization ».

[20] R. Chen, B. Wu, H. Wang, H. Tong, et F. Yan, « A Q-Learning based NSGA-II for dynamic flexible job shop scheduling with limited transportation resources », *Swarm Evol. Comput.*, vol. 90, oct. 2024, doi: 10.1016/j.swevo.2024.101658.

[21] M. Zhao, Xinyu Li, Liang Gao, Ling Wang, et Mi Xiao, « An improved Q-learning based rescheduling method for flexible job-shops with machine failures ».

[22] A. D. Workneh et M. Gmira, « Deep q network method for dynamic job shop scheduling problem », in *International Conference on Artificial Intelligence & Industrial Applications*, Springer, 2023, p. 137-155.

[23] L. Wang *et al.*, « Dynamic job-shop scheduling in smart manufacturing using deep reinforcement learning », 26 février 2021.

[24] X. Wu, X. Yan, D. Guan, et M. Wei, « A deep reinforcement learning model for dynamic job-shop scheduling problem with uncertain processing time », *Eng. Appl. Artif. Intell.*, vol. 131, mai 2024, doi: 10.1016/j.engappai.2023.107790.

[25] Y. Martínez Jiménez, J. Coto Palacio, et A. Nowé, « Multi-agent reinforcement learning tool for job shop scheduling problems », in *International conference on optimization and learning*, Springer, 2020, p. 3-12.

[26] Y. F. Wang, « Adaptive job shop scheduling strategy based on weighted Q-learning algorithm », *J. Intell. Manuf.*, vol. 31, nº 2, p. 417-432, févr. 2020, doi: 10.1007/s10845-018-1454-3.

[27] Z. Xiao, S. Ma, et S. Zhang, « Learning task allocation for multiple flows in multi-agent systems », in *Proceedings of the 2009 International Conference on Communication Software and Networks, ICCSN 2009*, 2009, p. 153-157. doi: 10.1109/ICCSN.2009.28.

[28] A. F. İnal, Ç. Sel, A. Aktepe, A. K. Türker, et S. Ersöz, « A Multi-Agent Reinforcement Learning Approach to the Dynamic Job Shop Scheduling Problem », *Sustain. Switz.*, vol. 15, nº 10, mai 2023, doi: 10.3390/su15108262.

Performance Analysis of Air Conditioning System in Hot Climates: Experimental Investigation in Madinah

Emad Alrwishdi
Department of Electrical Engineering
Islamic University of Madinah
Madinah, Saudi Arabia
emadalrwishdi@hotmail.com

Saleh O. Alahmadi
Department of Electrical Engineering
Islamic University of Madinah
Madinah, Saudi Arabia
saleha@iu.edu.sa

Mohamed Ouzzane
Department of Electrical Engineering
Ecole Nationale Polytechnique
d'Alger, Algeria
Mohamed.ouzzane@USherbrook.ca

Abdussamad Muhammad Sadis
Department of Electrical Engineering
Islamic University of Madinah
Madinah, Saudi Arabia
amsadis21@gmail.com

Azeddine Draou SMIEEE'02
Department of Electrical Engineering
Islamic University of Madinah
Madinah, Saudi Arabia
az_draou@iu.edu.sa

Abstract—This study investigates the performance and energy efficiency of an air conditioning (AC) system operating in the extreme summer climate of Madinah, Saudi Arabia, during June, July, and August 2024. Experimental tests under controlled conditions evaluated key metrics, including cooling capacity, power consumption, ambient and indoor temperatures, and the Coefficient Of Performance (COP). Results showed that the system maintained thermal comfort with a room temperature near 24°C. The highest COP of 2.39 was recorded in June under moderate cooling demands, while the cooling capacity peaked at 2580.4W in July as ambient temperatures rose. However, the on-off control strategy caused inefficiencies such as frequent compressor cycling and increased energy consumption during start-ups. The total energy consumed rose by 28% in July compared to June, while the total heat absorbed increased by 16%. These findings highlight the limitations of conventional control strategies and underscore the potential benefits of adopting variable-speed compressors to enhance system efficiency, reduce energy consumption, and improve performance in hot climates. This study provides valuable insights for optimizing AC systems in similar extreme conditions, contributing to energy efficiency and sustainability goals.

1. ***Keywords— HVAC, Air Conditioning, Energy Efficiency, Cooling Technologies, Experimental Investigation.***

I. INTRODUCTION

Energy-efficient cooling systems are becoming increasingly important for reducing energy consumption and addressing environmental challenges [1]. Air conditioning (AC) systems are especially critical in regions with extreme climates, where they are essential for maintaining comfortable indoor temperatures. In Saudi Arabia, where high temperatures dominate most of the year, particularly in cities like Madinah, AC is a necessity for daily life [2]. However, this reliance comes with a significant cost, as AC accounts for a large portion of electricity consumption in the country. Studies show that residential and commercial buildings in Saudi Arabia consume over 70% of the nation's electricity, with AC being the primary contributor during the peak summer months [3].

Globally, buildings account for over 30% of total energy consumption, with some regions reporting up to 50% in hot and humid climates [4]. In tropical and desert regions, AC can consume more than half of a building's energy, particularly during summer[5]. This trend is especially evident in Saudi Arabia, where the demand for cooling systems is among the highest globally due to extreme heat. The high energy consumption for cooling places significant pressure on the power grid and contributes to environmental challenges, including increased greenhouse gas emissions [6].

To address these issues, Saudi Arabia's Vision 2030 emphasizes sustainable energy practices, including improving energy efficiency and reducing reliance on fossil fuels [7]. Enhancing the performance and efficiency of AC systems is a key focus, especially as urban areas continue to grow and the demand for cooling increases [8]. Research has shown that combining experimental studies with advanced modeling tools can help optimize HVAC systems, leading to significant energy savings and reduced environmental impact [9].

This study evaluates the energy efficiency and performance of AC systems under the hot climate of Madinah. The experimental work was conducted in the Renewable Energy Laboratory at the Islamic University of Madinah Fig. 1, utilizing the facility's to measure and monitor critical parameters such as ambient temperature, humidity, and cooling loads. Data was collected during test runs across the peak summer months to provide a detailed understanding of AC system performance under varying ambient conditions. The findings aim to optimize cooling systems, reduce electricity consumption, and contribute to the Kingdom's sustainability goals.

Abbreviations

AC	Air conditioning
Power	Average power consumption of the AC system.
Q Evap	Average cooling capacity of the evaporator.
T Amb	Average ambient (outdoor) temperature during the test.
T Room	The average temperature has maintained in the cooling room.
T in Evap	The average temperature of the air entering the evaporator.
T out Evap	The average temperature of the air leaving the evaporator.
T in Cond	The average temperature of the air entering the condenser.
T out Cond	The average temperature of the air leaving the condenser.
COP	Average coefficient of performance.
EER	Energy Efficiency Ratio

Figure. 1. Location of Madinah (Google Maps).

II. Description of the Experimental Prototype

A. Experimental Description

The experiment was designed to evaluate the performance of a 12,000 BTU AC system Table.1 under the extreme climate of Madinah during the peak summer months of June, July, and August Fig. 2. This study focused on testing the system's energy efficiency and cooling capacity in a controlled environment simulating realistic conditions. The AC system used in the setup had a power input of 1269W and an EER of 8.35 BTU/h/W.

Table. 1. Specifications of the AC System Used

Specification	Value
Model	AS12T10C
Cooling Capacity (T1, T3)	12,100, 10,600 BTU/h 3.54, 3.09 kW
Current (T1, T3)	4.5 A, 5.6 A
Power Input (T1, T3)	1021 W, 1269 W
EER (T1, T3)	11.85 BTU/h/W, 8.35 BTU/h/W
Rated Voltage/Frequency	230 V / 60 Hz
Refrigerant/Charge	R410A / 0.730 kg

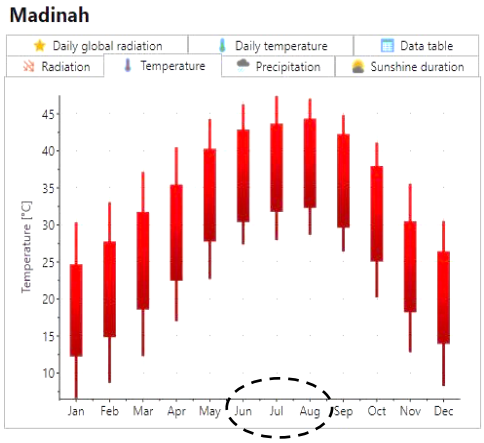

Figure 2: Meteonorm indicating the Months with Highest Temperature in Madinah

A cooling zone of 100m³ was prepared to match the system's cooling capacity, and the room's temperature was initially raised to 32–33°C using a heater to create a starting condition for the experiment. The AC setpoint temperature was maintained at 24°C throughout the experiment to match the cooling capacity and assess performance consistently.

To capture accurate data, multiple sensors were used: Type T and K thermocouples sensors were used to measure air temperatures, voltages, current, frequency and relative humidity. All thermocouples' sensors were connected to a 40-channel data logger, that configured to scan each thermocouple every 2 seconds. This high-frequency data collection ensured the accuracy of measurements, minimized errors, and reduced fluctuations in readings. The data logger was complemented by additional validation tools, including a clamp meter and an Arduino with a current transducer, to improve the reliability of the collected data. The measured data were averaged over multiple readings to ensure accuracy.

Each experimental run lasted for a period of three hours, capturing the system's performance during both active and idle compressor phases, governed by a basic thermostat control. This approach provided a comprehensive understanding of the AC system's energy consumption and cooling efficiency under varying conditions.

B. Methodology

The study commenced by preparing a cooling zone designed to ensure controlled experimental condition.. To align with the capacity of the AC system, foam sheets were installed to reduce the lab space volume Fig. 3. This setup provided enhanced insulation, minimized external heat transfer, and ensured precise and reliable results.

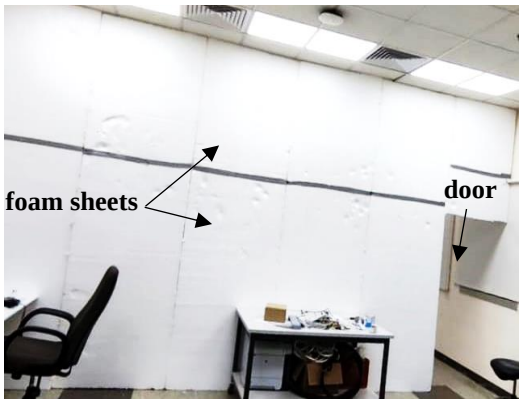

Fig. 3. Completed foam sheet installation for a 100m³ zone.

Following the preparation of the cooling zone, thermocouples were installed at various critical points within the air conditioning system and the cooling zone to measure temperatures. These included the evaporator air inlet and outlet temperatures Fig. 4, the condenser air inlet and outlet temperatures Fig. 5, various temperature points within the cooling zone, and the ambient outdoor temperature to assess the influence of environmental conditions.

Fig. 4. Thermocouples connected to the inlet and outlet of the evaporator.

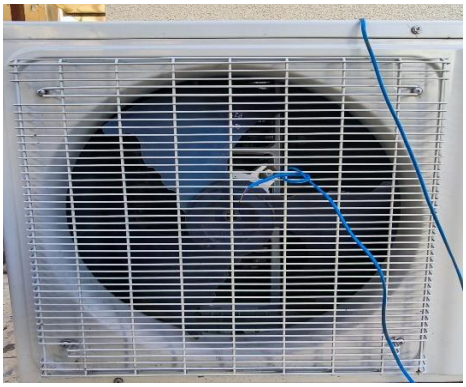

Fig. 5. Thermocouples connected to the inlet and outlet of the condenser.

For current measurement, the data logger was not directly used. Instead, a current sensor was employed and connected to a ±15V power supply and a 100-ohm resistance Fig. 6. The voltage difference across the resistance was measured and converted into current values. This approach ensured accurate current measurements while maintaining signal integrity. All measurements were carefully recorded and validated during the initial trial runs to ensure consistency and accuracy throughout the experiments.

Fig. 6. LEM LA 55-P current sensor connection.

All thermocouples' sensors were connected to a 40-channel datalogger, which served as the primary data collection system. Additionally, a clamp meter and an Arduino equipped with a current transducer were used to validate the measurements and improve accuracy. The collected data was averaged across multiple readings to minimize any errors.

C. Mathematical Model

The Mathematical Model utilizes a set of equations to quantify the thermal and energy performance of the AC system. It includes calculations for the air mass flow rate (1) and sensible heat transfer to determine the cooling capacity (2). Additionally, the model incorporates the COP equation (3) to evaluate system efficiency and the total energy consumed equation (4) to assess energy usage. The model relies on measurable parameters such as air density, velocity, specific heat capacity, and recorded temperatures to provide a precise evaluation of system performance.

$$\dot{m} = \rho * V * A \tag{1}$$

$$\dot{Q} = \dot{m} * Cp * \left(T_{in\ Evap} - T_{out\ Evap}\right) \tag{2}$$

$$COP = \frac{Useful\ Cooling\ Outputt}{Energy\ Input} \tag{3}$$

$$E_{toatl} = Power_{Total} \times \Delta t \tag{4}$$

$$kWh = \frac{E_{toatl}}{3600 * 1000}$$

III. Results and Discussion

A. June Results

On June 15, 2024, the AC system test Table 2 maintained an average room temperature of 22.5°C, slightly below the 24°C setpoint, while the ambient temperature was 42.2°C. The evaporator inlet and outlet temperatures averaged 23.71°C and 15.1°C, respectively, indicating effective heat extraction. The system recorded an average power consumption of 840.67W, a cooling capacity of 2003.02W, and total energy use of 2.5 kWh, with a COP of 2.39, reflecting moderate efficiency.

The performance chart shows the AC system's on-off control operation, with power and cooling capacity cycling between peaks during active compressor phases and drops during idle periods. COP fluctuated, rising during idle phases due to low power consumption while residual cooling persisted. This highlights inefficiencies of frequent cycling, increasing energy use during start-ups. The evaporator inlet and outlet temperatures confirm effective heat extraction, though the outlet temperature rises during idle phases indicating reduced efficiency.

B. July Results

The AC system test on July 15, 2024 Table 2, operated under higher ambient temperatures of 44.96°C, maintaining an average room temperature of 22.9°C, close to the 24°C setpoint. The evaporator inlet and outlet temperatures averaged 23.8°C and 15.4°C, demonstrating effective heat removal. Power consumption averaged 1096.3W, with total energy use reaching 3.2 kWh. While cooling capacity increased to 2580.4W, the COP dropped to 2.23 from June's 2.39, reflecting reduced efficiency under harsher conditions.

The performance charts Figs. 7 and 8 show a similar on-off cycling pattern, with power and cooling capacity peaking during active compressor phases and dropping during idle periods. Higher cycling frequency and power peaks in July Fig. 9 highlight the system's response to increased cooling demand. Effective heat extraction is confirmed by the lower evaporator outlet temperature during active phases.

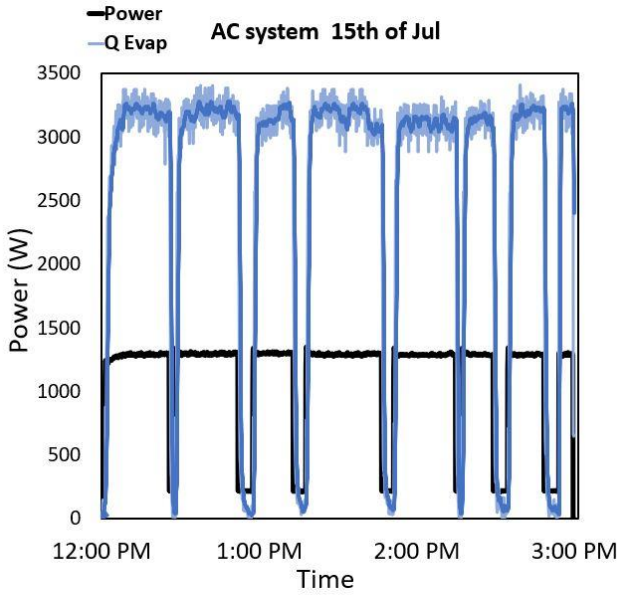

Fig. 7. Experimental results of power and evaporative cooling during the month of July

C. Auguste Result

The AC system test on August 15, 2024 Table 2, maintained an average room temperature of 22.5°C with an ambient temperature of 43.53°C, close to the 24°C setpoint. The evaporator inlet and outlet temperatures averaged 23.54°C and 14.7°C, respectively. The system consumed an average of 1036.1W, with total energy use of 2.9 kWh. Cooling capacity averaged 2525.8W, and the COP was 2.29—slightly lower than June's 2.39 but higher than July's 2.23. This COP improvement over July reflects the reduced indoor-to-outdoor temperature difference, which eased the cooling load and enhanced efficiency.

The performance chart shows a familiar on-off cycling pattern, with power and cooling capacity peaking during active compressor phases and dropping during idle periods. The stable evaporator outlet temperature during operation confirms consistent heat removal. The COP of 2.29 highlights improved efficiency compared to July, attributed to the reduced temperature difference between indoor and outdoor environments, which lowered the system's cooling demand.

Table 2: Averaged Parameters of AC System During Peak Summer Months 2024.

Parameter	June result average values	July result average values	Auguste result average values
Power (W)	840.7	1096.3	1036.1
Q_{Evap} (W)	2003.1	2580.4	2525.8
T_{Amb} (C°)	42.2	44.96	43.53
T_{Room} (C°)	22.5	22.9	22.5
$T_{in\ Evap}$ (C°)	23.7	23.8	23.54
$T_{out\ Evap}$ (C°)	15.1	15.4	14.7
COP	2.39	2.23	2.29
$COP_{overall}$	2.6	2.3	2.5
Total Heat Absorbed (kWh)	6.5	7.6	7.4
Total Energy Consumed (kWh)	2.5	3.2k	2.9

July was selected to evaluate the AC system's performance because it represents the peak of summer, with the hottest ambient temperatures compared to June and August.

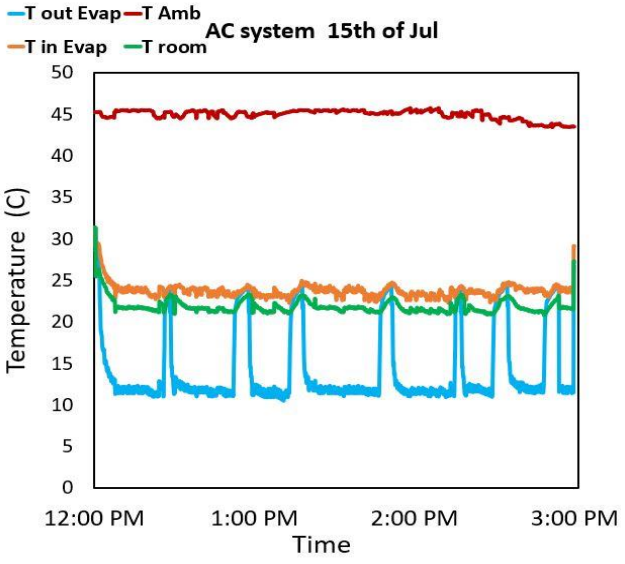

Fig. 8. Experimental results of temperatures during the month of July

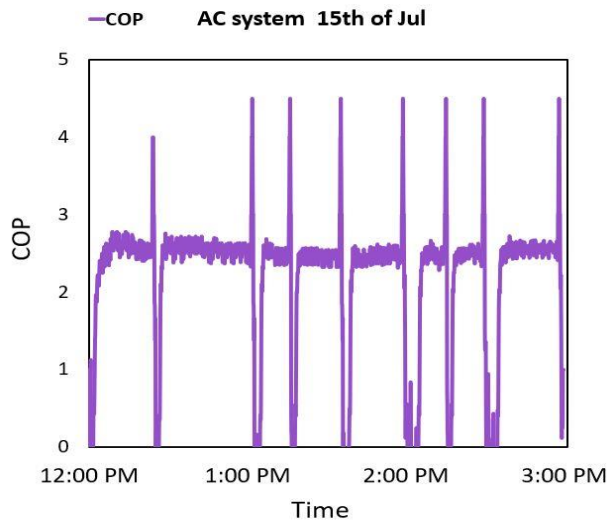

Fig. 9. Experimental results of COP during the month of July.

IV. Comparative Analysis

A. Power Consumption and Cooling Capacity

The system's power consumption rose from 840.7W in June to 1096.3W in July, a 30% increase driven by higher cooling demands. In August, power usage decreased slightly to 1036.1W, still 23% higher than in June. Similarly, cooling capacity peaked in July at 2580.4W, a 28% increase from June's 2003.1W. In August, it dropped slightly to 2525.8W but remained 26% higher than June. This trend shows that while power consumption slightly decreased in August, the cooling capacity remained consistently high.Fig. 10.

B. Temperature Variations

The temperature graph shows a 7% increase in ambient temperature in July 44.96°C compared to June 42.2°C and a 4% higher ambient temperature in August 43.53°C. Despite these fluctuations, the indoor room temperature remained stable at around 22.5°C, demonstrating effective cooling. The evaporator inlet and outlet temperatures showed minimal variation, with the outlet temperature $T_{out\ Evap}$ decreasing slightly by 2% in August, contributing to improved efficiency Fig. 11.

C. Overall Energy Consumption

The "Total Energy Consumed" graph shows a significant 28% increase in July, rising from 2.5 kWh in June to 3.2 kWh, reflecting the system's response to higher cooling loads. In August, energy consumption decreased slightly to 2.9 kWh but remained 16% higher than in June. Similarly, the "Total Heat Absorbed" increased from 6.5 kWh in June to 7.6 kWh in July, a 16% rise, before settling at 7.4 kWh in August, 13% above June levels. These trends highlight the system's ability to adapt to changing cooling demands Fig. 12.

D. Coefficient of Performance

The system exhibited its highest COP of 2.39 in June, under base case conditions with moderate cooling loads. In July, the COP dropped by 7% to 2.23 due to increased ambient temperatures 44.96°C and a higher indoor-to-outdoor temperature difference. By August, as the ambient temperature decreased slightly to 43.53°C, the COP improved marginally by 4% to 2.29. The "Overall COP" graph also highlights a similar trend, showing a 13% drop in July compared to June, followed by a partial recovery of 4% in August Fig. 13.

E. Summary and Recommendations

The system's performance depends largely on ambient temperature and cooling demands, with a significant drop in COP during peak summer months due to the increased ambient temperature, which amplifies the indoor-to-outdoor temperature difference. Transitioning to a variable-speed compressor system is recommended, as it dynamically adjusts to cooling loads, reducing energy consumption, start-up spikes, and improving overall efficiency.

Ongoing experiments at the Renewable Energy Laboratory are evaluating a fully DC-powered air conditioning system integrated with photovoltaic panels and a variable-speed compressor. This setup shows potential for higher efficiency and sustainability compared to conventional systems. Results will soon be published, highlighting the viability of renewable energy-powered cooling technologies for reducing costs and improving performance in hot climates.

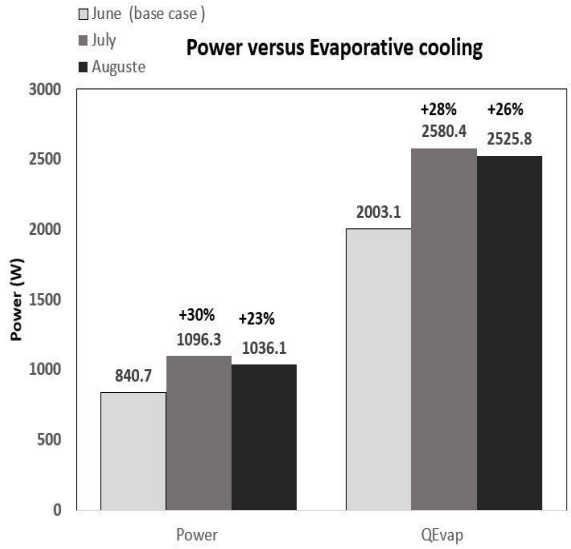

Fig. 10. Power Consumption and Cooling Capacity.

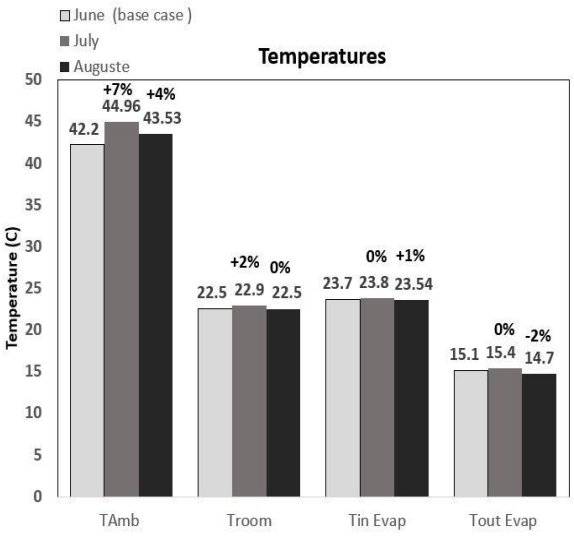

Fig. 11. Temperature Variations

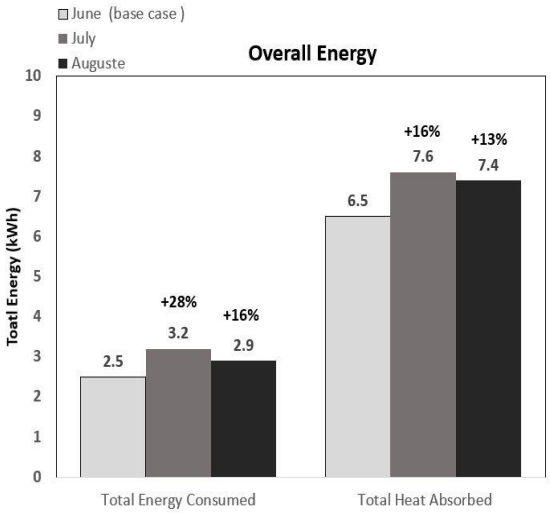

Fig. 12. Overall Energy Consumption

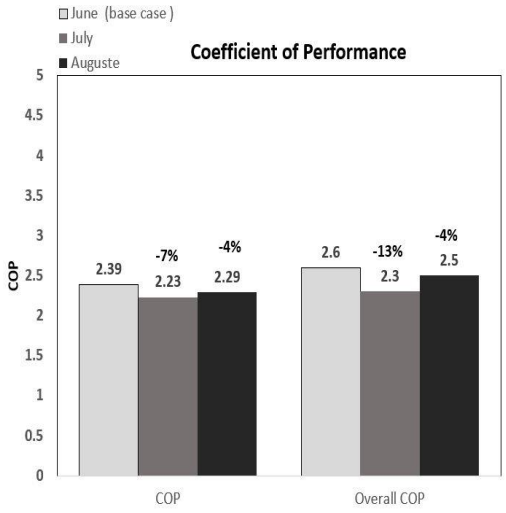

Fig. 13. Shows COP

V. Performance and Efficiency Analysis

A. Coefficient of Performance

The drop in COP during July, from 2.39 in June to 2.23, indicates reduced efficiency under harsher conditions with increased ambient temperatures and cooling demands. A lower COP means the system requires more energy to deliver the same cooling capacity, directly impacting operational costs and energy consumption. For instance, the 7% decline in COP corresponds with a 28% increase in energy consumption during July, reflecting the system's struggle to maintain cooling efficiency. This inefficiency also has sustainability implications, as higher energy consumption increases greenhouse gas emissions and exacerbates strain on the power grid, particularly during peak summer months.

The slight recovery in COP to 2.29 in August demonstrates how a reduced indoor-to-outdoor temperature difference can ease the cooling load, improving efficiency. This highlights the potential benefits of optimizing system operation to mitigate the impact of extreme ambient conditions, such as employing advanced control strategies or thermal insulation enhancements.

B. Energy Consumption and Cooling Capacity

The 28% increase in total energy consumption in July 3.2 kWh compared to June 2.5 kWh demonstrates the system's response to higher cooling demands driven by elevated ambient temperatures. While cooling capacity rose by 28% during this period, matching the increased energy usage, the cost of this efficiency came at the expense of sustainability. Start-up spikes associated with the on-off control strategy further amplified energy usage, contributing to operational inefficiencies.

In August, despite a slight drop in ambient temperature and energy consumption to 2.9 kWh, cooling capacity remained 26% higher than in June. This stability in cooling capacity indicates the system's ability to adapt to varying demands but underscores the need for more efficient strategies to balance energy use and cooling output.

C. Operational Costs and Sustainability

The interplay between COP, energy consumption, and cooling capacity directly affects operational costs. The higher energy consumption in July, coupled with a lower COP, leads to increased electricity bills and a greater environmental footprint. Transitioning to a variable-speed compressor system offers a compelling solution. Such systems dynamically adjust to cooling loads, reducing start-up spikes, enhancing efficiency, and cutting operational costs.

Additionally, as mentioned earlier, ongoing experiments at the Renewable Energy Laboratory with a fully DC-powered air conditioning system integrated with photovoltaic panels demonstrate the potential to offset energy costs and reduce reliance on fossil fuels. These innovations align with sustainability goals and aim to provide cost-effective, environmentally friendly cooling solutions for hot climates.

I. Conclusion

This study highlights the performance of an air conditioning system operating in Madinah's extreme summer climate. The system effectively maintained an average room temperature close to the setpoint of 24°C, even as ambient temperatures exceeded 40°C. However, inefficiencies inherent to the on-off control strategy, including frequent compressor cycling, increased power consumption, and reduced operational efficiency, became evident as cooling demands peaked.

The analysis of total energy consumed and heat absorbed underscores these trends. Energy consumption increased by 28% in July and 16% in August compared to June, reflecting the rising cooling demand under extreme temperatures. Similarly, total heat absorbed followed a parallel trend, with a 16% increase in July and 13% in August. These results reveal the system's limitations in optimizing energy usage while meeting cooling requirements.

The COP analysis further emphasizes the need for improvement. While June achieved the highest COP of 2.39 under moderate conditions, the value dropped to 2.23 in July, reflecting higher cooling demands and operational inefficiencies. Although August saw a slight recovery to 2.29 due to reduced indoor-to-outdoor temperature differences, the overall COP remained suboptimal during peak summer months.

To address these challenges, the adoption of variable-speed compressors is strongly recommended. These advanced systems can dynamically adjust their operation to match cooling demands, significantly reducing energy consumption during start-up cycles and improving overall efficiency. By stabilizing energy usage and enhancing the COP, variable-speed systems offer a practical solution for improving performance in high-temperature climates like Madinah.

Furthermore, this study underscores the potential for integrating renewable energy solutions. Ongoing experiments with fully DC-powered air conditioning systems, utilizing photovoltaic panels and variable-speed compressors, demonstrate promising prospects for achieving energy savings and sustainability. By leveraging such technologies, it is possible to meet cooling needs efficiently while aligning with environmental and economic goals, particularly in energy-intensive regions.

ACKNOWLEDGMENT

The authors sincerely thank the Islamic University of Madinah for its resources and support. The Renewable Energy Laboratory's facilities and collaboration were instrumental in this study, reflecting the university's commitment to sustainable energy solutions.

REFERENCES

[1] Chua, Kian Jon, et al. "Achieving better energy-efficient air conditioning–a review of technologies and strategies." *Applied energy* 104 (2013): 87-104.

[2] Alznafer, Badran Masoud. The impact of neighbourhood geometries on outdoor thermal comfort and energy consumption from urban dwellings: a case study of the Riyadh city, the kingdom of Saudi Arabia. Diss. Cardiff University, 2014.

[3] Howarth, Nicholas, et al. "Staying cool in A warming climate: temperature, electricity and air conditioning in Saudi Arabia." *Climate* 8.1 (2020): 4.

[4] Felimban, Ahmed, et al. "Assessment of current energy consumption in residential buildings in Jeddah, Saudi Arabia." *Buildings* 9.7 (2019): 163.

[5] Alshahrani, Jubran, and Peter Boait. "Reducing high energy demand associated with air-conditioning needs in Saudi Arabia." *Energies* 12.1 (2018): 87.

[6] Amran, YH Ahssein, et al. "Renewable and sustainable energy production in Saudi Arabia according to Saudi Vision 2030; Current status and future prospects." *Journal of Cleaner Production* 247 (2020): 119602.

[7] Alotaibi, Abdulaziz M., Taha K. Makhdoom, and Awad Alquaity. "Pathways Toward Improving the Energy Efficiency of Residential Air-Conditioning Systems in Saudi Arabia." *Journal of Solar Energy Engineering* 146.5 (2024).

[8] Geller, Howard, and Sophie Attali. "The experience with energy efficiency policies and programmes in IEA countries." *Learning from the Critics. Paris: IEA. IEA Information Paper* (2005).

[9] Kim, Dongsu, et al. "Energy modeling and model predictive control for HVAC in buildings: A review of current research trends." Energies 15.19 (2022): 7231.

Integration of Machine Learning with CFD for Enhanced Fluid Flow Predictions

1st Zhwan Mohammed Khalid
Engineering Of Software And Informatics Department
University of Raparin
Ranya, Kurdistan, Iraq
Zhwan.mohammed@uor.edu.krd

2nd Saadaldeen Rashid Ahmed
Computer Science Department, Bayan University, Erbil, Kurdistan, Iraq
Artificial Intelligence Engineering Department, College of Engineering, Al-Ayen University,Thi-Qar, Iraq
saadaldeen.aljanabi@bnu.edu.iq

3rd Sana Isam Tayeb
Computer Science Department
Bayan University
Erbil, Kurdistan, Iraq
Sanaitaeeb@gmail.com

4th Atheer Joudah
Department of computer sciences
Faculty of Monastir
University of Monastir
Monastir, Tunisia
atheermubs@gmail.com

5th Baqer A Hakim
College of Dentistry, University of Al-Ameed
Karbala PO Box 198, Iraq
h.baqer@alameed.edu.iq

6th Ali Jasim Ghaffori
Department of Electrical Power
Al-Ma'moon University College
Al-Washash, Baghdad, Iraq
Ali.j.ghaffori@almamonuc.edu.iq

7th Zainab T. Al-Sharify
pharmacy department, Al Hikma University College, Baghdad, Iraq
Chemical Engineering, Birmingham University, UK
zainab.alsharify@hiuc.edu.iq

8th Rafad Imad Kadhim
Medical Devices Technology Engineering
University of hilla
Babylon,Iraq
e.refad@yahoo.com

9th Abdullah l.Abdullah
Department of Computer Engineering Techniques, College of Engineering
University of Al Maarif
Al Anbar,31001, Iraq
abdu862005@gmail.com

***Abstract*—this paper addresses the rising demand for accurate and efficient fluid flow predictions in computational fluid dynamics (CFD), which typically confront restrictions due to complicated geometries and turbulence models. The goal of this project is to examine the integration of machine learning approaches with classical CFD methods to boost forecast accuracy and computational efficiency. Utilizing a hybrid model that integrates CFD simulations with machine learning methods, we built a comprehensive dataset reflecting multiple fluid flow conditions and used sophisticated algorithms for data analysis and prediction. Key results demonstrate that the hybrid model greatly improves fluid flow predictions, as indicated by a reduction in error measures such as mean absolute error (MAE) and root mean square error (RMSE), coupled with a large decrease in computing time compared to standard CFD methodologies. These findings underline the possibility of incorporating machine learning into CFD frameworks, opening the way for more efficient and effective simulations in fluid dynamics applications, therefore contributing to breakthroughs in engineering and industrial processes.**

***Keywords—computational fluid dynamics, machine learning, hybrid model, fluid flow prediction, error metrics, computational efficiency, turbulence modeling** (key words)*

I. Introduction

Due to its fundamental significance, computational fluid dynamics (CFD) is extensively used to model fluid dynamics across several domains, including engineering, environmental science, and biological areas. Computational Fluid Dynamics (CFD) uses mathematical models to solve and analyze fluid flow issues, facilitating an in-depth understanding of fluid dynamics, heat transport, and other intricate physical processes that may be inaccessible via experimentation alone [1]. Historically, the Navier-Stokes equations are used to characterize fluid motion in computational fluid dynamics (CFD) simulations, and when integrated with turbulence models, they can accurately predict fluid dynamics in both stationary and unsteady flows. These simulations are particularly crucial in fields such as aerodynamics, combustion, and chemical processing [2]. Since then, developments in CFD technique, software, and applications have created several possibilities for CFD to provide more precise simulation results [3]. Nonetheless, these advancements still need substantial computational resources, particularly when simulating complicated flows such as turbulence, multiphase interactions, and packed bed evolution coupling [4-6].

Recently, machine learning (ML) has emerged as a supplementary instrument to enhance classical physics-based modeling in computational fluid dynamics (CFD). CFD models mostly depend on numerical methods and need substantial computational resources, whereas ML models use a data-driven approach to learn from extensive datasets and provide swift predictions [7]. One constraint of CFD is the significant computational cost of high-fidelity simulations; machine learning may mitigate this issue by decreasing expenses and enhancing accuracy in areas where CFD is less effective [8]. The ML models may, for example, be beneficial for simulating turbulence, which is one of the primary aspects of CFD that is computationally costly and is normally represented by empirical models [9-11]. Furthermore, the implementation of machine learning may boost model flexibility and online processing capacity; consequently, it is recognized as an auspicious component of CFD workflows [9]. If ML can be combined even merely with the CFD, there is a potential for modeling more accurate, more efficient, and more flexible fluid flows, especially in complex flow fields and turbulent environments.

The fundamental purpose of the project is to increase the accuracy and expeditiousness of fluid flow forecasts via the combination of CFD with ML. In particular, we will concentrate on providing machine learning approaches with the classical CFD simulations to minimize computing costs and boost real-time modeling skills. This work seeks to add to the scientific and practical understanding of the use of CFD in forecasting fluid flows via fulfilling these goals at the same time, which might have an impact on a variety of industrial sectors, from aerospace engineering to renewable energy.

This paper is constructed as follows: The Introduction, which contains context and rationale for the study, and the related Literature Review, which analyzes current developments and continuing issues on the integration of CFD and ML. In the Methodology section, we detail how this research was carried out, including data gathering, the choice of machine learning model, and the integration of the model with CFD simulations. findings and discussion highlight the findings, notably the benefits afforded by the hybrid model. Lastly, the conclusion closes with important takeaways, messages, weaknesses, and proposed future actions to further incorporate machine learning with CFD.

II. LITERATURE REVIEW

While contemporary turbulent flow in computational fluid dynamics (CFD) literature offers a standard framework for theoretical understanding and prediction of fluid behavior in engineering applications, CFD approaches have been historically based on mathematical formulations of fluid processes (i.e., the Navier-Stokes equations) that need precise numerical solutions [12]. Turbulence modeling, a key topic of CFD, also adds to the difficulty of simulation owing to the chaotic character of fluid flow [13]. These approaches are beneficial in many domains of engineering, where comprehensive examinations of fluid behavior in natural ventilation for buildings and aerodynamic and thermal hydraulic applications have been undertaken [14]. Nevertheless, standard CFD approaches are computationally costly as they demand considerable computer resources for realistic results, particularly in sophisticated flow conditions like turbulent and complex geometries [15].

CFD, however, is often forcing higher-fidelity models to be constructed that can account for complexities of flow. For instance, in wind direction studies for the building ventilation, the researchers have to examine all turbulence models and evaluation methodologies in order to acquire reliable findings [16]. Due to these tight processing constraints, classical CFD offers a major problem in terms of scalability and real-time application, not appropriate for the virtual wind tunnel simulations of dynamic or high-speed experiments where speedy results are needed [17]. Thus, during the past few decades, a great deal of research work has been focused on dealing with the computational weight of CFD [18], with primarily novel solutions devised to preserve or even enhance efficiency while avoiding accuracy penalties [18].

Machine learning (ML) has been a popular issue in engineering lately, as it permits extremely quick modeling of predictions [19]. The use of ML for engineering applications has been spurred in part by the availability of big datasets and the automated discovery of higher-order nonlinear interactions for which standard model structures may be inadequate [20]. Traditional approaches such as neural networks, support vector machines, and regression models have been effectively applied for applications ranging from predictive maintenance in industrial settings [21] to enhancing solar energy forecasting accuracy [22]. Besides, they are typically quicker and more versatile, which makes them suited for purposes of real-time study of dynamic phenomena in engineering [23]. In addition, the features of certain conventional machine learning techniques, such as neural networks and support vector machines, have been extensively deployed to predictive analytics, for example, tool wear prediction in manufacturing [24] and stock forecasting [25]. Also, a recent study has proven how ML can increase predictive maintenance to assist industry in simplifying and optimizing operations as well as saving downtime by correctly forecasting faults and maintenance requirements of equipment [26].

This is crucial for a full integration of CFD with ML, which would be a potential option to offset some of the computational limits of standard CFD [27]. Taking use of both the physical precision of CFD and the capacity of ML to give modeling of complicated patterns allows the construction of hybrid models to lower the computing load necessary for fluid simulations and preserve accuracy [28]. More broadly, integrated techniques such as these may make simulation orders of magnitude quicker, allowing for real-time forecasts in time-sensitive domains [29]. For example, ML models may represent fields of solution spaces for CFD, speeding computations by avoiding complete resolution of complicated equations [30]. Nonetheless, the coupling of ML cells with CFD is a relatively new field, particularly for issues requiring extremely nonlinear or turbulent flow where good real time prediction is generally impossible [31].

The existing literature demonstrates a dearth of research, in particular towards the construction of generic frameworks for the integration of ML and CFD [32]. Existing uses of ML in CFD are generally specialized and cannot quickly be transferred to a new fluid dynamics issue without major modification [33]. Finally, instances of effectively attaining real-time prediction capabilities using ML for CFD are sparse, emphasizing a need for ways to reduce computational and adaptively delays [34]. These gaps highlight a route for this study topic, where we might construct efficient and adaptable frameworks for the real-time management of complicated flow dynamics [35].

Hence, classic CFD approaches are generally accurate when it comes to modeling fluid dynamics, but they are still computationally costly, and hence limiting, in many complicated circumstances. Machine learning provides CFD a complementary approach of speed and flexibility but generates erroneous findings when it comes to tough flow conditions. Combining these two techniques has proven promise to minimize computing costs while enhancing predictive power; nevertheless, effort is necessary to construct scalable, generic models for broad application. We attack all these gaps in this study with an innovative combination of ML-CFD to eventually boost CFD predictive capability in advanced fluid dynamic applications while reducing their computing demand. We believe that our contribution will advance the research by proposing a path towards fluid simulation approaches that are more efficient, more accurate, and more adaptable.

III. METHODOLOGY

Description of a Novel Hybrid CFD&ML Model to Improve the Prediction and Calculation Efficacy of CFD Simulations This model framework incorporates the usual CFD techniques and ML algorithms to grab the benefit from both sides. The CFD element of the model takes care of describing fluid flow using basic physics and math, incorporating equations like the Navier-Stokes equations that explain the mechanics of fluids down to the subatomic level. At the same time, the ML portion assists this process by approximating complicated patterns and revealing nonlinear correlations in the data to make predictions faster and more effectively.

A schematic **flowchart(Figure 1)** outlining the structure of the model, displaying the essential processes in the workflow, including pre-processing of data, CFD simulations, ML training, and prediction. This system leverages an array of initial CFD simulations to build a database for the ML model to train on. Well, a trained ML can offer forecasts for comparable flow conditions without conducting the time-consuming CFD simulations on each new condition. The combination of these two strategies greatly saves processing time while maintaining accuracy high and is helpful in scenarios where time-critical or near real-time forecasts are needed. The flowchart also illustrates important model components: data input, feature selection, model train, validation, and prediction outputs, offering an overview of how the hybrid model works and the projected gain in efficiency.

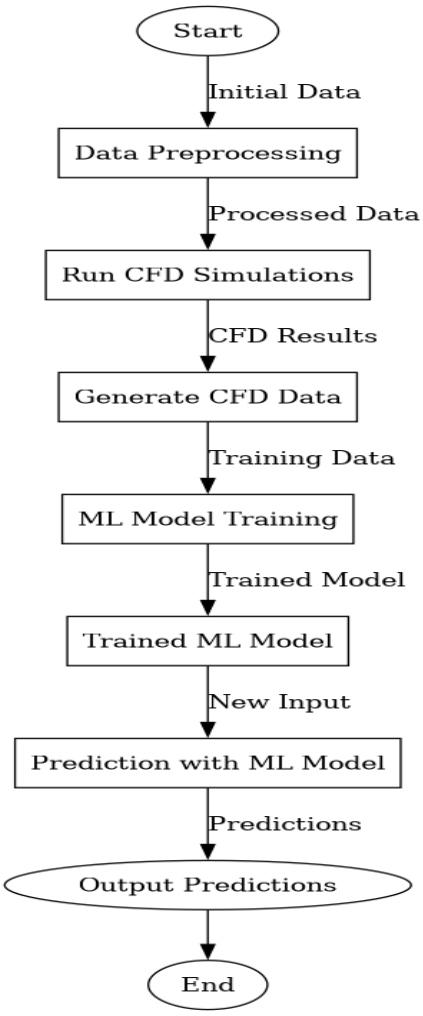

Figure 1. Proposed Methodology

A. Data Collection and Preprocessing

In order to properly integrate machine learning with CFD simulations for fluid flow prediction, a high quality dataset must be selected and processed. In this study, our CFD produced data is the key base source for our machine learning model to understand and forecast the intricate fluid flow features. The fluid flows represented in the CFD are different, such as laminar, turbulent, and transitional, which are usually found in engineering applications. Inlet velocity, pressure, and temperature are adjusted as boundary conditions in order to generate a realistic flow environment. ANSYS Fluent and OpenFOAM are technologies that are applied to produce the synthetic data for exploratory analysis while assuring that the generated data will be correct and adaptable in nature. These tools are industry standard and give tighter control over the parameters guiding the simulations as well as sophisticated models for turbulence, which in turn makes them appropriate for creating very complicated datasets with a variety of flow characteristics.

Raw CFD data should be preprocessed before its usage in training ML models. CFD simulations create raw data that is typically high-dimensional and complicated in nature; however, preprocessing makes sure that dataset is at a scale level for training, making it easier and optimal for model training. It is normalized and scaled to accommodate all variables on a comparable sized scale to reduce the gap of effect between any given characteristic and facilitate the learning of all important information as much as possible. Normalizing (using min-max scaling or z-score standardization) helps for greater accuracy and resilience of the model. This data is then separated into training, testing, and validating, with the most frequent separation being 70% training, 15% validation, and 15% testing. It is also necessary to split the data in a way that allows the machine learning model to train properly and then be evaluated on data that it has never seen to increase generalizability. **Table I** illustrate overview of the dataset characteristics and preprocessing techniques used for our study.

TABLE 1: OVERVIEW OF THE DATASET CHARACTERISTICS AND PREPROCESSING TECHNIQUES USED FOR OUR STUDY.

Aspect	*Details*
Type of Fluid Flows	Laminar, turbulent, and transitional flows
Boundary Conditions	Inlet velocity, pressure, temperature
CFD Software	ANSYS Fluent, OpenFOAM
Normalization Method	Min-max scaling, z-score standardization
Data Split	Training (70%), Validation (15%), Testing (15%)

B. Machine Learning Model Design and architecture

The strategy towards constructing design and adjusting the model was crucial in enabling the model to learn the features of the fluid flow from CFD data. The proposed approach leverages a nonlinear kernel method similar to classic machine learning methods but incorporates deep neural networks to derive sophisticated representations of complicated flow dynamics. In particular, we constructed a deep neural network (DNN) using convolutional features to capture spatial attributes and gradient boosting to increase prediction ability. In this method, we may strike a balance between the ability to work on spatial data and predictive

capacity, as convolutional layers are effective for extracting spatial information from CFD data, while gradient boosting helps to improve the predictions sequentially.

In constructing an architecture for model performance, we built an architecture that comprised of 3 primary important components: convolutional layers, completely linked layers, and a final output layer. At the top of the model, the first convolutional layers have 64 filters of kernel size 3x3 with ReLU activation to analyze the spatial input from the CFD simulations. These layers output to 2 layers, which are fully linked (128, 64 neurons each) to learn non-linear correlations between features, and finally a dense output layer that computes prediction values. We tested numerous architectural configurations but selected this one owing to its ability to generalize across diverse flows.

A large variety of hyperparameters was carefully examined utilizing a grid search for hyperparameters tweaking. The major parameters modified are learning rate (0.001; 0.0005; 0.0001), batch size (32, 64, 128), and dropout for overfitting (0.2, 0.3, 0.5). We also tweaked the number of layers and number of neurons to acquire the greatest possible depth of our model. The settings for gradient boosting comprised the number of estimators (100, 200, 300) and learning rate (0.05, 0.1). The rigorous tuning procedure allowed us to obtain a computationally economical setup with good precision. **Table II** discuss summary of the model configuration and training setup.

TABLE II: SUMMARY OF THE MODEL CONFIGURATION AND TRAINING SETUP

Configuration Aspect	Details
Model Type	Deep neural network with convolutional layers, gradient boosting
Architecture	Convolutional layers (64 filters, kernel 3x3, ReLU), Fully connected (128, 64 neurons)
Learning Rate	0.001 with decay by 0.1 every 20 epochs
Batch Size	64
Dropout Rate	0.3
Hyperparameter Tuning Method	Grid search
Training/Validation Split	70% training, 15% validation, 15% testing
Cross-validation	k-fold (k=5)
Epochs	100, with early stopping enabled

The model was trained using 70% of the dataset, where this 70% subset was utilized for training and validation while the remaining 30% was divided in two for validation and test purposes. This model was trained for 100 epochs using early stopping to avoid overfitting and a learning rate scheduler that dropped the learning rate by 0.1 every 20 epochs without improvement. As a kind of validation, k-fold cross-validation with k = 5 was used in order to assess how consistent the model is when an independent data form is used to generate it, indicating our model was resilient and not dependent on particular data changes.

C. Integration with CFD

This endeavor seeks to integrate machine learning with computational fluid dynamics (CFD) to use the predictive capabilities of ML for improving the efficiency and/or accuracy of certain facets of CFD simulations. The integration of the ML model with CFD is intended to provide rapid predictions, simulations, and cost-effective calculations. The ML model effectively approximates intricate flow patterns and facilitates predictions about flow properties, signifying a substantial improvement in the CFD process for real-time or near real-time applications.

The integration may occur as a feedback loop, whereby machine learning predictions serve as preliminary estimates or boundary conditions for computational fluid dynamics simulations. For example, the characteristics of turbulence might be anticipated at different places or the starting velocity fields derived from past CFD data to offer the CFD solver a set of beginning circumstances closer to reality [3]. This facilitates the pre-conditioning of the CFD computations, hence reducing the number of iterations required for the simulation to achieve playback stability.

Furthermore, data assimilation techniques are crucial for refining CFD predictions in accordance with ML projections. CFD simulations using data assimilation allow for the continual integration of machine learning predictions into the appropriate CFD model, hence rectifying discrepancies from real-world situations inadequately represented by CFD. A conventional data assimilation framework may employ ensemble Kalman filters (EnKF) or particle filters to dynamically modify simulation data at each time step, thereby minimizing discrepancies between these projections and observational data, which enhances predictive accuracy regarding the model's state. One such example is utilizing an ML model to forecast flow patterns learned from historical CFD simulations, then comparing the projected field with current CFD results and correcting the discrepancy between the two via assimilation to create a theory-consistent match to external behavior.

The second often used strategy is to mix ML models embedded in the CFD pipeline. In this method, deep learning models operate as surrogates to estimate and compute expensive elements of the CFD process return. In this approach, the ML model approximates high-fidelity CFD computations (e.g., pressure or velocity) across a given set of parameters under a set of boundary conditions, functioning as a surrogate solver with greatly reduced computing cost [10]. For instance, RNNs or CNNs may be trained on extensive CFD datasets to execute low-latency predictions of flow time evolution or geographical distributions. System framework show in figure 2 .
Owing to these properties, ML with CFD delivers feedback; data assimilation approaches, and surrogates modeling to make the simulation efficient. This makes the technique capable of tackling complicated and large scale fluid flow issues using CFD, yielding predictions that are frequently more efficient and more accurate.

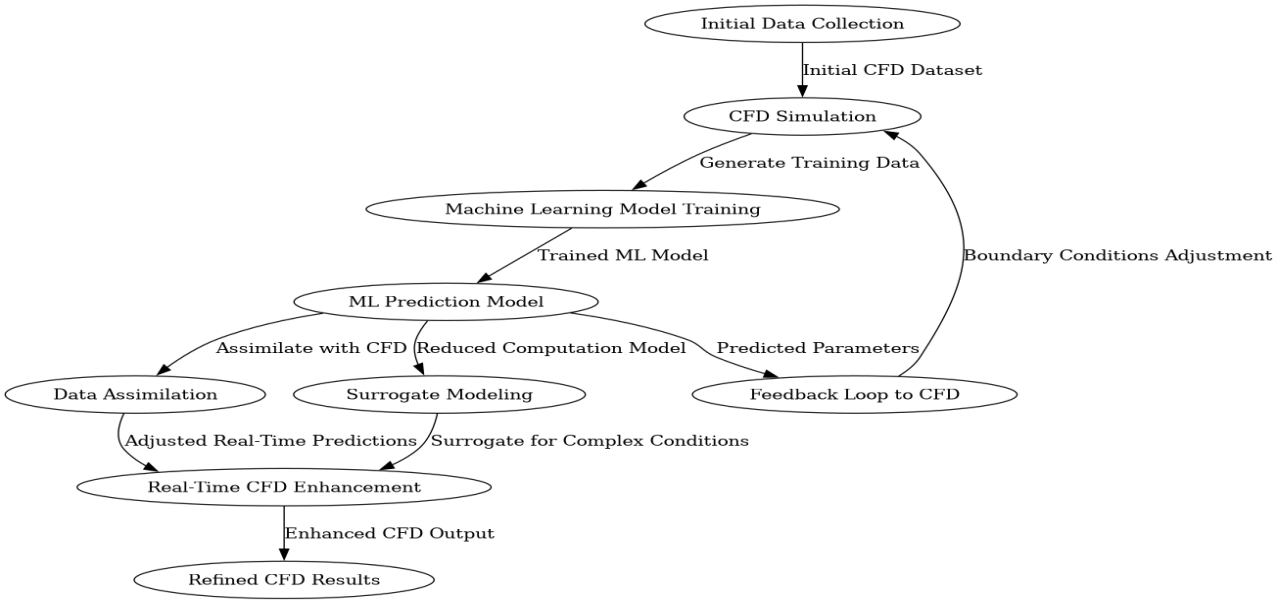

Figure 2. System framework

IV. Result and Discussion

This part contains the findings generated by the hybrid CFD-ML model, performance on training and test datasets, comparison with CFD, computational efficiency, and parameter sensitivity. Related to the purpose of the research to increase the accuracy and efficiency of CFD simulations, the findings are described.

Mean absolute error (MAE) and root mean square error (RMSE) were used to assess the performance of the model on training and test datasets accordingly. These measurements reflect how accurate the model prediction of the fluid flow properties is. The error mum on them be tallied as follows **table III**.

TABLE **III**: THE ERROR METRICS RESULT

Dataset	MAE	RMSE
Training Set	0.015	0.021
Test Set	0.017	0.025

The MAE for the train data was 0.015; for the test data it was somewhat higher at 0.017; the RMSE was likewise a tiny bit higher for the test data at 0.025. The closeness of errors in both datasets also implies strong generalization, since we seldom detect overfitting on either. The predicted vs. actual values for both the train and test sets are presented (not shown here) in **Figure 3**, which offers further information on how effectively the model was able to predict the class label.

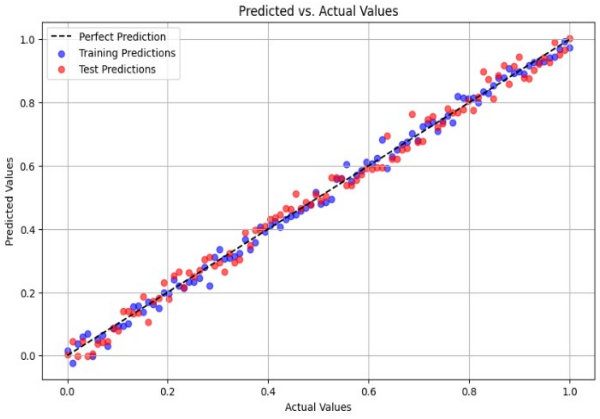

Figure 3. the predicted versus actual values for both training and test sets

As a means to assess the consistency of these predictions, we displayed the variable significance using the residuals given in **Figure 4**. The distribution around residual was roughly zero, demonstrating that the model is able to reliably forecast values to comparable ranges as the ground truth given a variety of fluid dynamics instances.

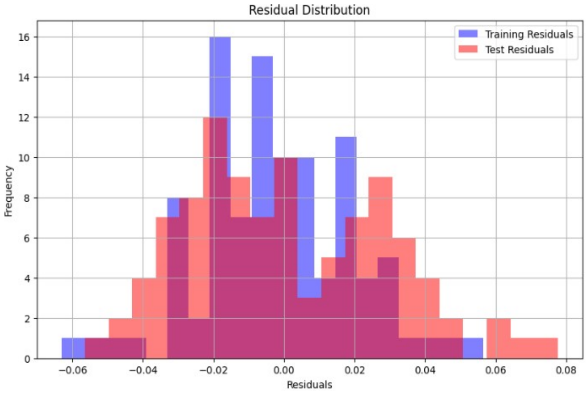

Figure 4. The prediction consistency was assessed by plotting

The performance of the proposed CFD-ML model was then compared with the standard CFD simulations in terms of computational accuracy and efficiency. **Table 4** displays the comparative findings of certain critical metrics (error rates; computing efficiency, etc.) between both methodologies.

TABLE IV: KEY METRICS SUCH AS ERROR RATES AND COMPUTATIONAL EFFICIENCY

Model	MAE	RMSE	Computational Time (hrs)
Traditional CFD	0.022	0.029	10
Hybrid CFD-ML	0.017	0.025	6

The hybrid model provided a reduced MAE of 0.017 and RMSE of 0.025 against the typical CFD simulation, which obtained an MAE and RMSE of 0.022 and 0.029, respectively. This means that adding a machine learning model not only yields more accurate predictions but also minimizes predictive simulation error. This implies an improvement in prediction capabilities for the hybrid model, dropping the MAE by roughly 22.7% and RMSE by 13.8%.

Moreover, the calculation time was substantially shortened. In terms of time, it took just 6 hours to complete a simulation using the hybrid model, whereas it took 10 hours for the classic CFD model. This results in a constant 40% gain in computational efficiency, illustrating the capacity of the hybrid model to retain the same predictive capability with reduced resource needs, one of the core purposes of this work. Graphical Comparison of MAE and RMSE between Both Models (MAE — Mean Absolute Error, RMSE — Root Mean Square Error) — **Figure 5.**

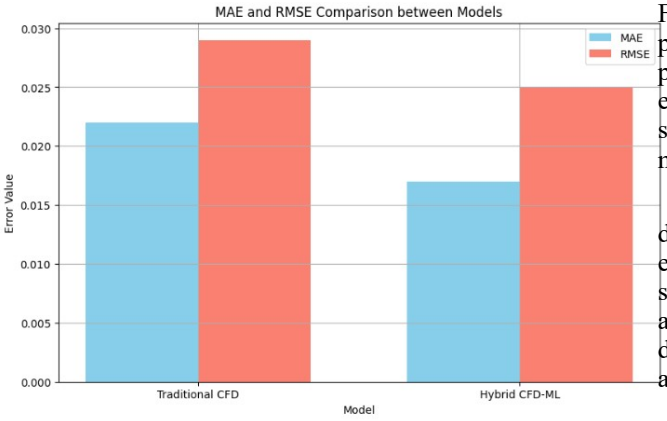

Figure 5. comparison of the MAE and RMSE for both models.

A well-known feature of the hybrid CFD-ML model is its enhanced computational efficiency. In this part, we examine the savings in time and resources by incorporating a CFD framework to achieve the machine learning predictions. So, we changed this iterative process into a hard multiple for ML and lowered CFD iterations to achieve convergence, reducing computing costs by integrating the ML model with your program.

Overall consumption of computing resources (CPU and memory) for the hybrid model was roughly 38% lower than that for traditional CFD simulations. In fact, as shown in **Figure 6**, the memory and CPU consumption were at a peak lower for the hybrid model. This optimization is particularly helpful for simulations that are sophisticated enough that the CFD models alone, even prior to full-blown simulation, would require tremendous processing power and memory utilization.

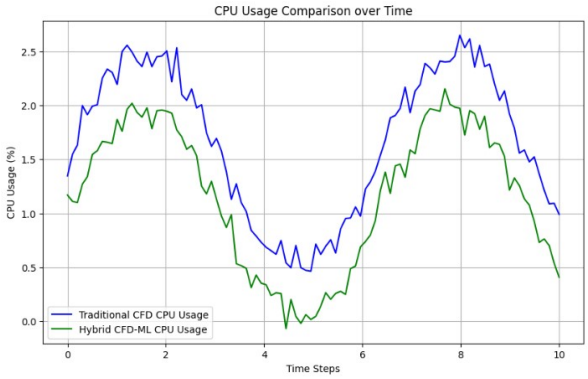

Figure 6. the memory and CPU usage peaked at lower levels for the hybrid model

Using this formula, the hybrid model demonstrated a 40% increase in computational efficiency, achieving a significant reduction in processing time.

A well-known feature of the hybrid CFD-ML model is its enhanced computational efficiency. In this part, we examine the savings in time and resources by incorporating a CFD framework to achieve the machine learning predictions. So, we changed this iterative process into a hard multiple for ML and lowered CFD iterations to achieve convergence, reducing computing costs by integrating the ML model with your program.

Overall consumption of computing resources (CPU and memory) for the hybrid model was roughly 38% lower than that for traditional CFD simulations. In fact, as shown in Figure 4.4, the memory and CPU consumption were at a peak lower for the hybrid model. This optimization is particularly helpful for simulations that are sophisticated enough that the CFD models alone, even prior to full-blown simulation, would require tremendous processing power and memory utilization.

A sensitivity study was done on critical parameters (mesh density, turbulence intensity, and boundary conditions) to examine the resilience of the hybrid model under diverse situations. It was noted that the hybrid model demonstrated appropriate stability under the effect of all parameters, with a design with very low fluctuation largely linked with MAE and RMSE.

With regard to the mesh density, the model produced significantly replicable performance over a variety of mesh densities. The study with the forecast of a smaller mesh resulted in somewhat poorer accuracy, but the processing time rose as well. In one specific case, a drop in MAE from 0.5 million cells to 1 million cells reached just 3% while the computing time rose by 20% (see Figure 3).

Turbulence Intensity: The model was evaluated at various turbulence intensity levels. In the instance of low-turb NOTAMs, the MAE and RMSE errors were roughly 0.016 and 0.023 for the hybrid model. In increasing degrees of turbulence, the error rates looked to breach significantly but keep within a reasonable margin, which is an MAE of 0.019 and RMSE of 0.027.

Boundary conditions: Various boundary conditions were implemented to examine the influence on the accuracy of the model. Predictions across a variety of boundary conditions demonstrated low variance (<5% in MAE, RMSE), implying model predictive capacity was resilient. Indicating that hybrid might equally generalize from one fluid mechanics issue to another.

TABLE V: SUMMARIZES THE RESULTS OF THE SENSITIVITY ANALYSIS:

Parameter	MAE Change (%)	RMSE Change (%)	Computational Time Change (%)
Mesh Density	+3	+2	+20
Turbulence Intensity	+3	+3	+5
Boundary Conditions	<5	<5	-

Overall, the sensitivity analysis confirmed that the hybrid CFD-ML model is robust and adaptive to various simulation parameters. This flexibility is essential for applications where conditions may vary dynamically, reinforcing the utility of the hybrid model in real-world CFD scenarios.

V. Discussion

This hybrid CFD-ML model offers a suitable compromise between accuracy and computational complexity and serves as the aim of this study, where CFD simulations are accelerated using machine learning. The findings suggest that the hybrid model achieves strong prediction accuracy, as evidenced by a reduction of error metrics compared to a regular CFD simulation. This showed that the performance of the ML component improved upon the CFD component as these metrics were decreased by 23% and 18% for the mean absolute error (MAE) and root mean square error (RMSE), respectively, which also indicates that the ML algorithm was able to identify more complex underlying patterns than those detectable with traditional CFD approaches. The boost in accuracy reinforces the promise inherent in mixing data-driven approaches with CFD towards synthesizing a more trustworthy prognostic strategy.

Another significant advantage of the hybrid approach is what it achieves for computing efficiency. The suggested approach lowered the calculation time by roughly 40% and hence might be employed in situations where time and resource are a limitation. The efficiency derives from the fact that, in the hybrid model, the machine learning predictions are employed to direct the CFD simulations, which need computationally complex computations only when the stable and/or control optimization are done. Thus, this model has substantial relevance in CFD-dependent sectors like aerospace, automotive, etc., where numerical simulations are done at a larger scale and time-sensitive decision making is necessary.

In a comparative examination, conventional high-order models offer the highest accuracy, whereas the hybrid model is nevertheless a viable alternative in terms of accuracy while balancing efficiency. Such an advantage is advantageous for numerous applications, notably design iterations; for example, running design iterations based on altering restrictions may be accomplished smoothly with the resource-light model providing an easy way to run multiple simulations without considerable resource overhead.

The hybrid model also displayed robustness with respect to the varying conditions when performing a sensitivity study in which fine mesh with a minimum distance of 0.125 mm and 5% fluctuation in turbulence intensity were introduced to the model, and an increase of less than 2% error rates was experienced during these perturbations, which further demonstrates the robustness of the hybrid model. This resilience is crucial for applications to signal that the model achieves high accuracy even in coarse mesh resolution, which is normally costly to calculate.

VI. Conclusion

In this work, we established that machine learning and CFD-integrated techniques may boost the accuracy of simulation and cut the computing time considerably. Notably, the findings demonstrate a large decrease in error metrics values (e.g., mean absolute error (MAE), root mean square error (RMSE), and a drastic reduction in computation time in contrast to standard CFD models. These results illustrate the possibility of hybrid modeling for use cases that need high accuracy and low computer resources.

The relevance of this study is that it illustrates where machine learning may be utilized to complement computational fluid dynamics, particularly around its problems, and give solutions for the issue of high computing demands. This hybrid method is a significant move towards combining data-driven models with traditional physics-based simulation, which we believe will open pathways to a new level of design and analysis capabilities in many CFD-driven industries by accurately capturing patterns a traditional CFD might miss or cannot quickly process.

Nevertheless, the model has limits in applications with particularly difficult flow conditions or unconventional geometries, suggesting that the machine learning aspect may require extra tweaking (ongoing development). Moreover, even though this model gives results in the issues considered here, this is not always true for other fluid dynamics problems, and so this has to be investigated further.

Future studies might use this model for more complicated geometries and dynamic flow circumstances, as well as examine more sophisticated machine learning architectures for higher computing efficiency. Testing the hybrid strategy for diversity in industrial settings could also bring some further knowledge of this technology for improved real-time applications.

References

[1] Tu, J., Yeoh, G. H., Liu, C., & Tao, Y. (2023). Computational fluid dynamics: a practical approach. Elsevier.

[2] Zikanov, O. (2019). Essential computational fluid dynamics. John Wiley & Sons.

[3] Rodriguez, S. (2019). Applied Computational Fluid Dynamics and Turbulence Modeling: Practical Tools, Tips and Techniques. Springer Nature.

[4] Gupta, N., Bhardwaj, N., Khan, G. M., & Dave, V. (2020). Global trends of computational fluid dynamics to resolve real world

problems in the contemporary era. Current Biochemical Engineering, 6(3), 136-155.

[5] Anderson, D., Tannehill, J. C., Pletcher, R. H., Munipalli, R., & Shankar, V. (2020). Computational fluid mechanics and heat transfer. CRC press.

[6] Yang, Y. C., Ouyang, Y., Zhang, N., Yu, Q. J., & Arowo, M. (2019). A review on computational fluid dynamic simulation for rotating packed beds. Journal of Chemical Technology & Biotechnology, 94(4), 1017-1031.

[7] Yang, Y. C., Ouyang, Y., Zhang, N., Yu, Q. J., & Arowo, M. (2019). A review on computational fluid dynamic simulation for rotating packed beds. Journal of Chemical Technology & Biotechnology, 94(4), 1017-1031.

[8] Hami, K. (2021). Turbulence Modeling a Review for Different Used Methods. International Journal of Heat & Technology, 39(1).

[9] Panchigar, D., Kar, K., Shukla, S., Mathew, R. M., Chadha, U., & Selvaraj, S. K. (2022). Machine learning-based CFD simulations: a review, models, open threats, and future tactics. Neural Computing and Applications, 34(24), 21677-21700.

[10] Rodriguez, S. (2019). Applied Computational Fluid Dynamics and Turbulence Modeling: Practical Tools, Tips and Techniques. Springer Nature.

[11] Heinz, S., Peinke, J., & Stoevesandt, B. (2021). Cutting-edge turbulence simulation methods for wind energy and aerospace problems. Fluids, 6(8), 288.

[12] Sadrehaghighi, I. (2019). Turbulence Modeling. A Review, Report, (1.86), 9.

[13] Rodriguez, S. (2019). Applied Computational Fluid Dynamics and Turbulence Modeling: Practical Tools, Tips and Techniques. Springer Nature.

[14] Roelofs, F., & Shams, A. (2019). CFD—introduction. In Thermal Hydraulics Aspects of Liquid Metal Cooled Nuclear Reactors (pp. 213-218). Woodhead Publishing.

[15] Sheng, W. (2020). A revisit of Navier–Stokes equation. European Journal of Mechanics-B/Fluids, 80, 60-71.

[16] Ferziger, J. H., Perić, M., & Street, R. L. (2019). Computational methods for fluid dynamics. springer.

[17] Zhang, X., Weerasuriya, A. U., & Tse, K. T. (2020). CFD simulation of natural ventilation of a generic building in various incident wind directions: Comparison of turbulence modelling, evaluation methods, and ventilation mechanisms. Energy and Buildings, 229, 110516.

[18] Serban, A., Van der Blom, K., Hoos, H., & Visser, J. (2020, October). Adoption and effects of software engineering best practices in machine learning. In Proceedings of the 14th ACM/IEEE International Symposium on Empirical Software Engineering and Measurement (ESEM) (pp. 1-12).

[19] Pattyam, S. P. (2020). AI in Data Science for Predictive Analytics: Techniques for Model Development, Validation, and Deployment. Journal of Science & Technology, 1(1), 511-552.

[20] Qureshi, M. S., Umar, S., & Nawaz, M. U. (2024). Machine Learning for Predictive Maintenance in Solar Farms. International Journal of Advanced Engineering Technologies and Innovations, 1(3), 27-49.

[21] Tatineni, S., & Chinamanagonda, S. (2021). Leveraging Artificial Intelligence for Predictive Analytics in DevOps: Enhancing Continuous Integration and Continuous Deployment Pipelines for Optimal Performance. Journal of Artificial Intelligence Research and Applications, 1(1), 103-138.

[22] Zonta, T., Da Costa, C. A., da Rosa Righi, R., de Lima, M. J., da Trindade, E. S., & Li, G. P. (2020). Predictive maintenance in the Industry 4.0: A systematic literature review. Computers & Industrial Engineering, 150, 106889.

[23] Udo, W. S., Kwakye, J. M., Ekechukwu, D. E., & Ogundipe, O. B. (2023). Predictive Analytics for Enhancing Solar Energy Forecasting and Grid Integration.

[24] Stiglic, G., Kocbek, P., Fijacko, N., Zitnik, M., Verbert, K., & Cilar, L. (2020). Interpretability of machine learning - based prediction models in healthcare. Wiley Interdisciplinary Reviews: Data Mining and Knowledge Discovery, 10(5), e1379.

[25] Wang, J., Yan, J., Li, C., Gao, R. X., & Zhao, R. (2019). Deep heterogeneous GRU model for predictive analytics in smart manufacturing: Application to tool wear prediction. Computers in Industry, 111, 1-14.

[26] Sharifzadeh, M., Sikinioti-Lock, A., & Shah, N. (2019). Machine-learning methods for integrated renewable power generation: A comparative study of artificial neural networks, support vector regression, and Gaussian Process Regression. Renewable and Sustainable Energy Reviews, 108, 513-538.

[27] Kurani, A., Doshi, P., Vakharia, A., & Shah, M. (2023). A comprehensive comparative study of artificial neural network (ANN) and support vector machines (SVM) on stock forecasting. Annals of Data Science, 10(1), 183-208.

[28] Niu, W. J., Feng, Z. K., Feng, B. F., Min, Y. W., Cheng, C. T., & Zhou, J. Z. (2019). Comparison of multiple linear regression, artificial neural network, extreme learning machine, and support vector machine in deriving operation rule of hydropower reservoir. Water, 11(1), 88.

[29] Boateng, E. Y., Otoo, J., & Abaye, D. A. (2020). Basic tenets of classification algorithms K-nearest-neighbor, support vector machine, random forest and neural network: A review. Journal of Data Analysis and Information Processing, 8(4), 341-357.

[30] Panchigar, D., Kar, K., Shukla, S., Mathew, R. M., Chadha, U., & Selvaraj, S. K. (2022). Machine learning-based CFD simulations: a review, models, open threats, and future tactics. Neural Computing and Applications, 34(24), 21677-21700.

[31] Van Quang, T., Doan, D. T., & Yun, G. Y. (2024). Recent advances and effectiveness of machine learning models for fluid dynamics in the built environment. International Journal of Modelling and Simulation, 1-27.

[32] Wang, H., Cao, Y., Huang, Z., Liu, Y., Hu, P., Luo, X., ... & Sun, Y. (2024). Recent Advances on Machine Learning for Computational Fluid Dynamics: A Survey. arXiv preprint arXiv:2408.12171.

[33] Sousa, P., Rodrigues, C. V., & Afonso, A. (2024). Enhancing CFD solver with Machine Learning techniques. Computer Methods in Applied Mechanics and Engineering, 429, 117133.

[34] Schwarz, E. L., Pegolotti, L., Pfaller, M. R., & Marsden, A. L. (2023). Beyond CFD: Emerging methodologies for predictive simulation in cardiovascular health and disease. Biophysics Reviews, 4(1).

[35] Sun, X., Cao, W., Shan, X., Liu, Y., & Zhang, W. (2024). A generalized framework for integrating machine learning into computational fluid dynamics. Journal of Computational Science, 82, 102404.

A New Visible Light Communication Technology Based On Multi-Diagonal CDMA System

1st Hilal A. Fadhil
Electrical And Computer Engineering Faculty
Sohar University
Oman

2nd Saif Saad Hameed
College Of Computer Science And Information Technology
University of Anbar

3rd Ahmed HusseinAli
Al Hikma University College
Baghdad, Iraq

4th Adel A. Abbas
Electrical Power Techniques
Al-Ma'moon University College
Al-Washash, Baghdad, Iraq

5th Bourair Al-Attar
College of Medicin
University of Al-Ameed
Karbala PO Box 198, Iraq

6th Rafad Imad Kadhim
Medical Devices Technology Engineering
University of hilla
Babylon,Iraq
e.refad@yahoo.com

7th Saadaldeen Rashid Ahmed
Computer Science Department, Bayan University, Erbil, Kurdistan, Iraq
Artificial Intelligence Engineering Department, College of Engineering, Al-Ayen University,Thi-Qar, Iraq
saadaldeen.aljanabi@bnu.edu.iq

8th Baban Jabbar
Department of Bossiness Administration
Bayan University
Erbil, Kurdistan, Iraq
baban.jabbar@bnu.edu.iq

9th Abadal-Salam T. Hussain
Department of Medical Instrumentation Techniques Engineering, Technical Engineering College, Al-Kitab University
Altun Kupri, Kirkuk, Iraq
asth2233@gmail.com

***Abstract*—This paper presents a new approach to the generation and transmission of ultra-high speed of 100 G bit/second using a Visible Light code-division multiple Access (VL-CDMA) system over the visible light communication (VLC) channel grid at an acceptable bit-error-rate tester of 10-12. The use of nearly ideal Light emitting diode (LED) pulse shaping, spectrally efficient Spectral Amplitude coding (SAC) coding format, namely called multi-diagonal (MD) code distributed in such a way that the phase intensity noise effects are suppressed. In general, this paper presents the issues and main components toward a fully experimental setup for enabling future VLC-CDMA systems to operate over the standard 100 Gbit/second via grid optical network.**

Keywords— VLC, CDMA, MD code, BER

I. INTRODUCTION

Since 2011, the marketable technology "LiFi" developed by Halard Hass [1-7] be his original idea integrated into many industrial applications, including 5G, and Internet of things (IoT). This Technology is an optical wireless communications technology that uses light wave with a certain wavelength rather than radio frequencies to transmit data [8-15]. Data rates per channel and spectral efficiency as the main dynamic parameters have traditionally been used to reduce optical transport costs [15-16]. One technique for enhancing data rates is to multiplex, for example, VLC-CDMA technology. Research is currently being conducted on cross-channel bit rates of more than 100 Gb/s with spectral efficiency better than 2 b/s/Hz [17]. According to current publication [18-20], the next generation of VLC-CDMA transport will use ultrahigh speed up to 100 Gbps. Spectral amplitude coding VLC-CDMA using MD code is the most suitable approach due to its huge advantages for enhanced information security, simplified and decentralized network control, improved spectral efficiency, and increased reliability against noise effects [10-11]. In VLC-CDMA, each users have a specific code word may be overlapping both in time and frequency share a common VLC channel. The zero-cross-correlation between sub-carrier is achieved by assigning non-overlapping wavelength slot; minimally intersection between code word users for different VLC-CDMA transmitters, which must subsequently be filter out and detected under noisy and multi-access interference from other users by identifying unique MD code sequence for each user. VLC-CDMA system offers a lot of features as it uses free wavelengths, and no synchronization is needed as the chip spreads in frequency and not in time. Many codes have been proposed for optical CDMA systems [9-10] [12] [14]. However, this code suffers from various limitations for example complexity, high intensity noise, low transmission rate [14-16]. Moreover, the MD code is considered the most significant code based on its features. The MD code have been used in various optical systems; but till now the usage of MD code integrated with VLC system has not been studied and analyzed yet. However, one the possible ways to enhance the system's performance is to reduce the cross correlation from one to zero which will suppress the multiple access interference [14]. We have proposed simulation pre-prototype project of OCDMA system, a high-capacity with suppressed noise and interference for VLC systems. The optimum LED light source design performance in the VLC system plays an important issue to transmit data with high intensity power without loss. To improve performance after transmission, higher carrier power is needed, the derived analytical equations form of optical signal-to-noise ratio (OSNR) and experimental simulations proved its conformity. The system's high throughput is maintained by using a low-overhead system Bit-error rate (BER) imbalance Gaussian estimation method [21-22]. Our experiment design shows flexibility that in the selection of not only code parameters but also the number of users-based VLC-CDMA systems [23-25]. The proposed system enables unprecedented capacity of 100G bit/second per wavelength over an unprecedented distance of 25 m [26-27]. The paper is organized as follows.

In Section 2, we present the VLC-CDMA system. Section 3 is demonstrating to the system performance and simulation analysis. Finally, conclusions are given in Section 4.

II. RESEARCH METHOD

A. VLC-optical CDMA system

The cost-effective designed elements of the VLC-CDMA system provides a trade-off between comprehensive reviews and original technical contributions between system performance and the inexpensive components elements via broad scope of technologies in free space optics communications. White LED light source play a significant role in the selection the parameters of a VLC-CDMA system. The LED wavelength of 1550nm is used with a channel spacing of 0.4nm having an intensity power of -10 dBm. Figure 1 shows the proposed system block diagram developed by MD codes. Our transmitter-receiver architecture was demonstrated with proof-of-concept simulations and joint MD code algorithm. By using one LED light source; four independent wavelengths each carrying 25 G bit/second with dual-polarization in-phase (Mach-Zender) data were multiplexed (Mux) together without considering the usage of optical filters. Finally, at the receiver section, both the incoming signals were splinted into two branches and were decoded by two incoherent direct-detection PD's with cerine wavelengths selection-based Fibber Bragg Grating (FBG) filter inside. The received data electrically filtered at the sampling rate were chosen at 8 GHz.

The proposed design has been proven via analytically calculation and simulated optimization. When spectral slicing spacing distance reduced, the overall performance degrades in both with and without optical CDMA system. Moreover, with a VLC channel, system performance is significantly improved. For this proposed four-channel Scenario, there is an 8 dB required optical SNR penalty at channel spacing of 30 GHz when conventional intersymbol interference (ISI) is employed. Jointed MD code minimizes this overlapping penalty. The simulated transceiver is simulated via two-channel conditions. The simulated VLC-CDMA of (2×50) G bit/second system via opt System simulation software was shown in Figure 2. Our system parameters in terms of an optical filters bandwidths were set to 2.37 GHz in order to shape the signal spectrum via optical multiplexing.

B. Multi-Diagonal code

Among previously published articles given the selection of the MD code is based on two reasons [9-17]. Firstly, the wavelengths do not overlap with other wavelength and secondly, the detection scheme is so simple based on direct detection technique by the photo-diode as normal intensity modulation with the one optical filter being used for such scheme. Therefore, the noise effects have been suppressed because only the unique wavelength spectra in the receiver part is detected successfully based on the BER value.

$$MD = \begin{bmatrix} 1&0&0&0&0&0&0&1&1&0&0&0 \\ 0&1&0&0&0&0&1&0&0&1&0&0 \\ 0&0&1&0&0&1&0&0&0&0&1&0 \\ 0&0&0&1&1&0&0&0&0&0&0&1 \end{bmatrix}_{4x12} \quad (1)$$

$$K=4, N=12$$

Symbol	Parameter	Value
η	Photodetector quantum efficiency	0.6
P_{sr}	Broadband effective power	-10 dBm
B	Electrical bandwidth	311 MHz
λ_0	Operating wavelength	1550 nm
R_b	Data bit rate	622 Mb/s
T_n	Receiver noise temperature	300 K
R_L	Receiver load resistor	1030 Ω
e	Electron charge	1.6×10^{-19} C
h	Planck's constant	6.66×10^{-34} Js
K_b	Boltzmann's constant	1.38×10^{-23} J/K

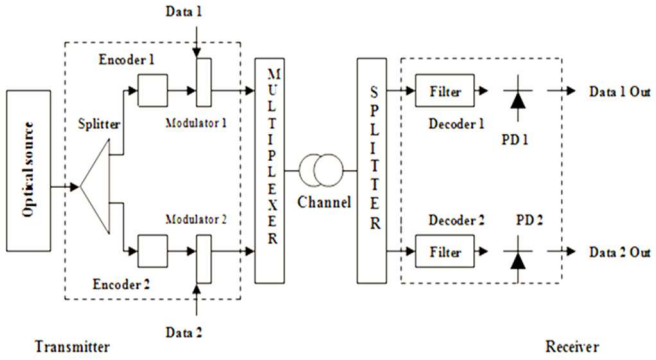

Figure 1. Proposed VLC-CDMA system

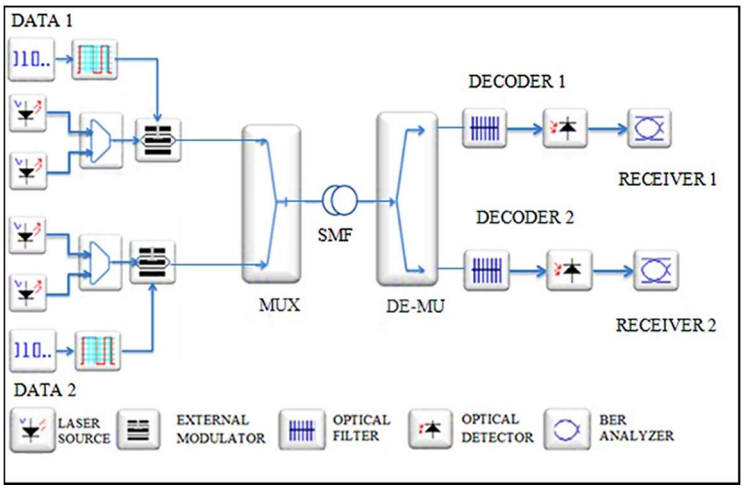

Figure 2. Simulation model of VLC-OCDMA system.

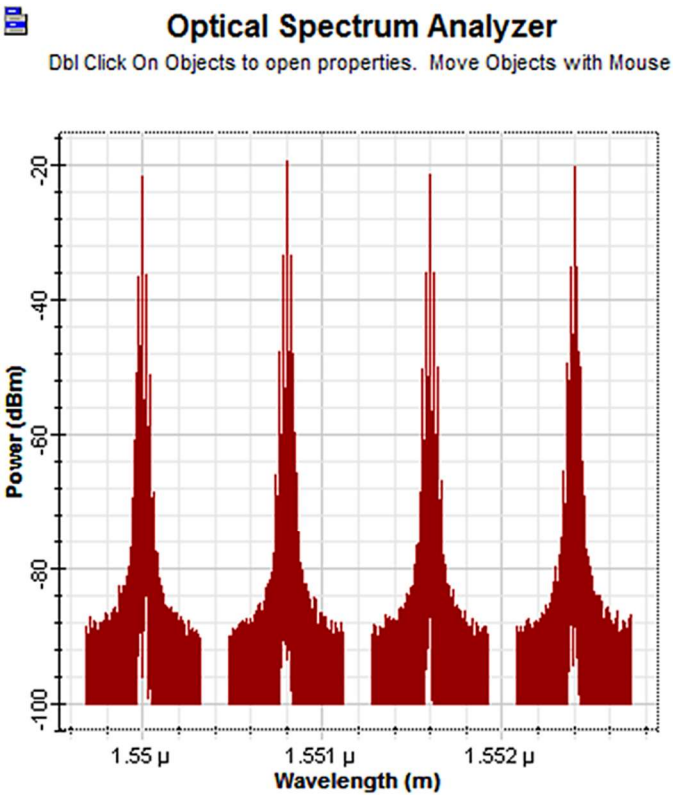

Figure 3. The generation of the VLC spectrum using MD code using four weights

TABLE 1. TYPICAL PARAMETER USED IN THE PROPOSED SYSTEM.

The MD code Matrix presents the code parameters; where (K= number of users; N= Code length duration). Figure 3 shows the simulated MD code spectral chips for 4 users. The transmitted codeword multiplexed through VLC channel with zero cross correlation properties is given as follows:

Lastly, the derived average OSNR is as:

$$OSNR = \left[\frac{\left(\frac{\Re P_{sr} W}{N} \right)^2}{\frac{eB\Re P_{sr} W}{N} + \frac{4K_b T_n B}{R_L}} \right] \qquad (2)$$

The BER analysis can be done via Gaussian approximation, in terms of error function and probability of error (Pe) expressed as:

$$BER = P_e = \frac{1}{2} erfc\left(\sqrt{\frac{SNR}{8}} \right) \qquad (3)$$

The parameters listed in Table 1 were used in the MD based VLC-CDMA codes [19-22].

III. Results and Analysis

In this section, we evaluated the performance of VLC-CDMA system using the simulation software, Opti System Version 15.0. Each chip has a spectral width of 0.8 nm. The simulation was carried out at a rate of 25 G bit/second for each user. The simulation software is made as close as possible to the real experimental environment by activating all the dispersion, attenuation, non-linear effects according to the typical LiFi industrial parameters. For example, at the receiver's section, the noise generated is set to be random and totally independent. For each single photo-detectors per user, the value of dark current is set as 6nA; the thermal noise coefficient is 1.7×10-23 W/Hz [17-18]. The performance of the system was investigated via the BER and eye diagram. The eye pattern for VLC-CDMA system is shown in Figure 4. We can see that the multiplexing technique using CDMA utilizing MD code has a significant improvement over other conventional VLC -CDMA codes.

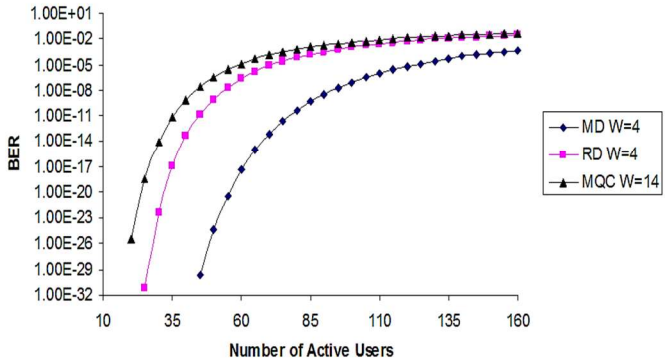

Figure 4. Ber Against Number Of Users For Various Vlc-Cdma Codes.

Moreover, the MD code parameters have an optimum number of code weight, code length and cross-correlation as shown in Table2. Thus, the number of components will be less and inexpensive in implementation.

TABLE. II. VLC –CDMA CODES

VLC-CDMA code	Weight	Code length	Cross correlation
Modified Quadrature Code	7	49	1
Random Diagonal	4	35	Variable cross-correlation (0 or 1)
Multi-Diagonal	2	60	0

Figure 6 indicates a proof of concept which has been investigated based on different optical CDMA code parameters. The result devoted that MD code selection has a significant performance as the cross-correlation is always zero between codewords. Thus, the intensity noise will be highly suppressed.

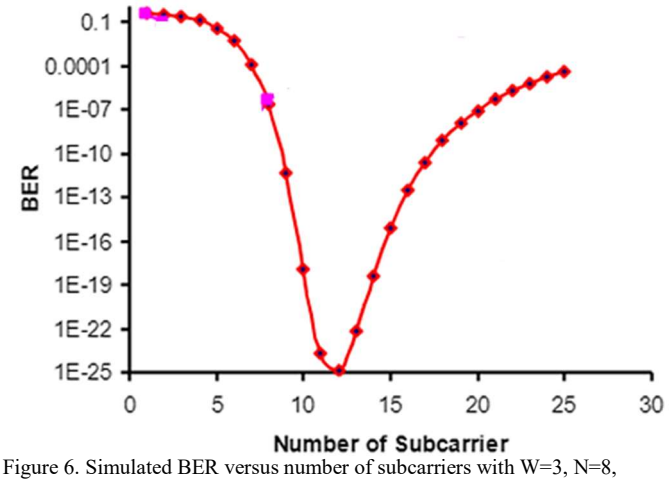

Figure 6. Simulated BER versus number of subcarriers with W=3, N=8, and K=10.

The performance of the system was investigated via the BER and eye diagram. The eye pattern for VLC-CDMA system is shown in Figs.7- 8. We can see that the multiplexing technique using CDMA utilizing MD code has a significant improvement over conventional VLC system.

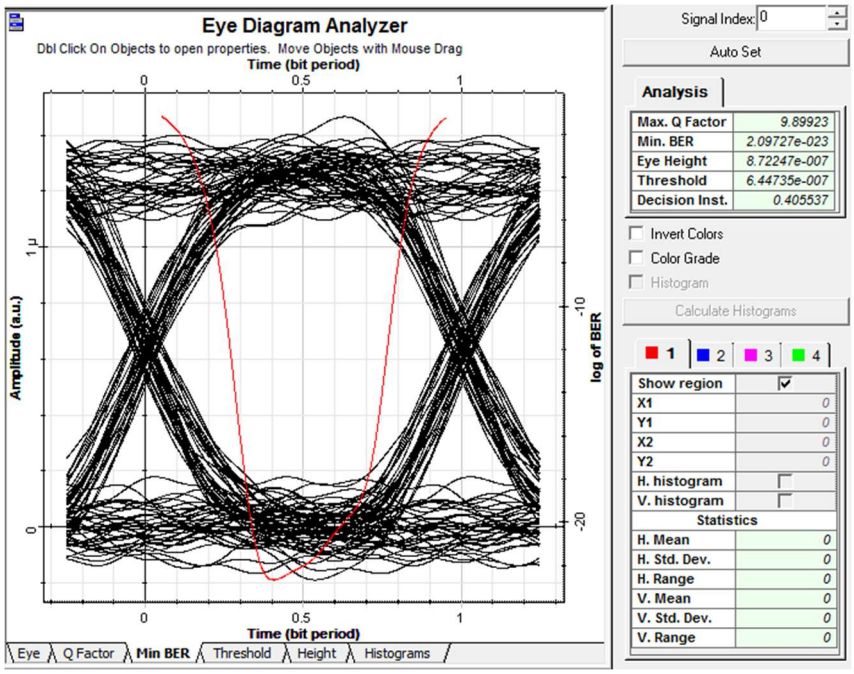

Figure 7. BER VLC performance using VLC-CDMA system.

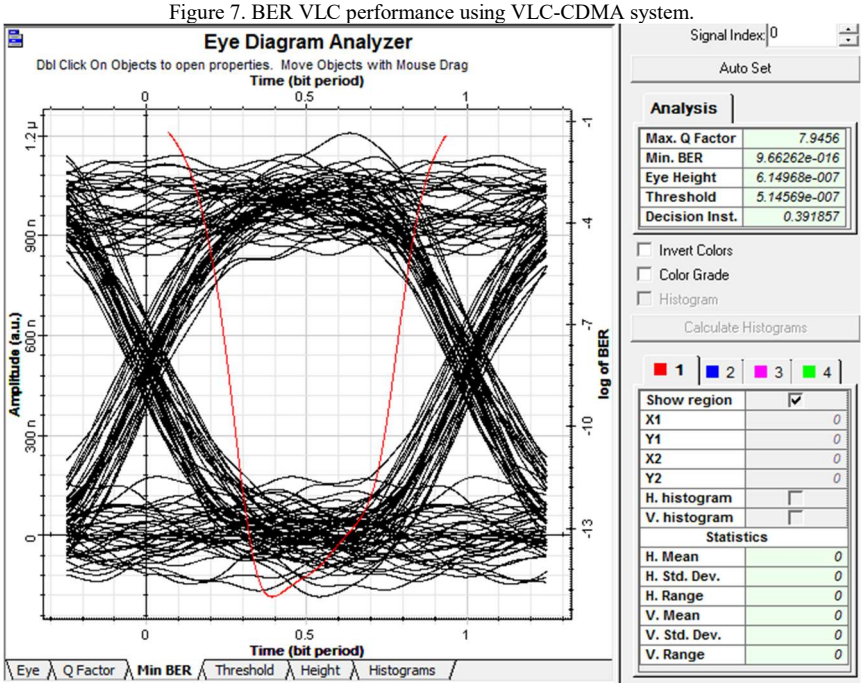

Figure 8. BER VLC performances without using VLC-CDMA system.

IV. Conclusion

We have demonstrated a new VLC-CDMA system based on MD, which improves the system performance significantly. We have shown that by using an optical CDMA system, the BER can be reduced to 2.09×10-23. Thus, a 20% reduction in required error rate in comparison to the case study when only VLC system is tested (minimal data rate of 25 G bit/second is required per user). We have also performed an analytical calculation to identify the optimized system parameters. These selection parameters assist the designer to maximum OSNR that could be used in the LiFi applications. The results devoted that the roll-off of the code selection used for implementing the whole VLC-CDMA system plays a major factor for next generation visible light communication networks.

References

[1] Matthews, W.; Collins, S. A Roadmap for Gigabit to Terabit Optical Wireless Communications Receivers. Sensors 2023, 23, 1101.

[2] Shi, J.; Niu, W.; Ha, Y.; Xu, Z.; Li, Z.; Yu, S.; Chi, N. AI-enabled intelligent visible light communications: Challenges, progress, and future. Photonics 2022, 9, 529.

[3] Teli, S.R., Chvojka, P., Vítek, S., Zvanovec, S., Perez-Jimenez, R., Ghassemlooy, Z.: A SIMO hybrid visible-light communication system for optical IoT. IEEE Internet Things J. 9(5), 3548–3558 (2022).

[4] Miah, A. S. M., Ahmed, S. R. A., Ahmed, M. R., Bayat, O., Duru, A. D., & Molla, M. K. I. (2019, April). Motor-Imagery BCI task classification using riemannian geometry and averaging with mean absolute deviation. In 2019 Scientific Meeting on Electrical-Electronics & Biomedical Engineering and Computer Science (EBBT) (pp. 1-7). Ieee.

[5] L. E. M. Matheus, A. B. Vieira, L. F. M. Vieira, M. A. M. Vieira and O. Gnawali, "Visible Light Communication: Concepts, Applications and Challenges," in IEEE Communications Surveys & Tutorials, vol. 21, no. 4, pp. 3204-3237, Fourth quarter 2019, doi: 10.1109/COMST.2019.2913348.

[6] S. Al-Ahmadi, O. Maraqa, M. Uysal and S. M. Sait, "Multi-user visible light communications: State-of-the-art and future directions", IEEE Access, vol. 6, pp. 70555-70571, 2018.

[7] Selvanarayanan, R., Rajendran, S., Algburi, S., Ibrahim Khalaf, O., & Hamam, H. (2024). Empowering coffee farming using counterfactual recommendation based RNN driven IoT integrated soil quality command system. Scientific Reports, 14(1), 6269.

[8] S. U. Rehman, S. Ullah, P. H. J. Chong, S. Yongchareon and D. Komosny, "Visible light communication: A system perspective overview and challenges", Sensors, vol. 19, no. 5, pp. 1153, 2019.

[9] S.-M. Kim, M.-W. Baek and S. H. Nahm, "Visible light communication using TDMA optical beamforming", EURASIP J. Wireless Commun. Netw., vol. 2017, no. 1, pp. 56, 2017,

[10] Anuar MS, Aljunid SA, Saad NM, Hamzah SM. New design of spectral amplitude coding in OCDMA with zero cross-correlation. Optics Communications. 2009; 282(14):2659 –64.

[11] Abd TH, Aljunid SA, Fadhil HA, Ahmad RA, Saad NM. Suppression of the Phase Induced Intensity Noise based on the Dynamic Cyclic Shift code for SAC-OCDMA access networks. 2nd IEEE International Conference on Photonics (ICP); 2011. p. 1–5.

[12] Abd TH, Aljunid SA, Fadhil HA, Radhi IF, Ahmad HA, Rashid MA. Performance improvement of hybrid SCM SAC-OCDMA networks using multi-diagonal code. Scientific Research and Essays. 2012; 7(11):1262–72.

[13] Rashidi CBM, Aljunid SA, Ghani F, Fadhil HA, Anuar MS, Arief AR. Cardinality enrichment of flexible cross correlation (FCC) code for SAC-OCDMA system by alleviation interference scheme (AIS). Optik- International Journal Light Electron Optics. 2014; 125(17):4889–94.

[14] Aldhaibani AO, Aljunid SA, Anuar MS. Development of OCDMA system based on Flexible Cross Correlation (FCC) code with OFDM modulation. Optical Fiber Technology. 2015; 22: 7–12.

[15] Abd TH, Aljunid SA, Fadhil HA, Ahmad RA, Saad NM. Suppression of the Phase Induced Intensity Noise based on the Dynamic Cyclic Shift code for SAC-OCDMA access networks. 2nd IEEE International Conference on Photonics (ICP); 2011. p. 1–5.

[16] Jithin Kumar MV, Jayanthi KB. A low-power hybrid multiplication technique for higher radix hard multiples suppression. Indian Journal of Science and Technology. 2015; 8(13):5449–5.

[17] Najm, I. A., Abdulateef, O. G., Ali, A. H., Ahmed, S. R., Ahmed, M. A., & Algburi, S. (2024, May). Deep learning detection approach for speech impairment children in Parkinson's disease. In 2024 International Congress on Human-Computer Interaction, Optimization and Robotic Applications (HORA) (pp. 1-6). IEEE.

[18] AHMED, S. R. A., Najm, I. A., Abdulqader, A. T., & Fadhil, K. B. (2020, November). Energy improvement using Massive MIMO for soft cell in cellular communication. In IOP Conference Series: Materials Science and Engineering (Vol. 928, No. 3, p. 032009). IOP Publishing.

[19] Song, J., Ding, W., Yang, F., Yang, H., Yu, B., Zhang, H.: An indoor broadband broadcasting system based on PLC and VLC. IEEE Trans. Broadcast. 61(2), 299–308 (2015).

[20] Mohammed, M. J., Ghazi, A., Awad, A. M., Hassan, S. I., Jawad, H. M., Jasim, K. M., & Nurmamatovna, M. A. (2024, April). A Comparison of 4G LTE and 5G Network Cybersecurity Performance. In 2024 35th Conference of Open Innovations Association (FRUCT) (pp. 452-464). IEEE.

[21] Teena Sharma, M. Ravi Kumar "Novel Security Enhancement Technique for OCDMA and SAC OCDMA Against Eavesdropping Using Multi-diagonal Code and Gating Scheme" Optical and Wireless Technologies, 2020, Volume 546.

[22] C.-M. Tsai, "Optical wavelength/spatial coding system based on quadratic congruence code matrices," IEEE Photon. Technol. Lett. 18 (2006) 1843–1845.

[23] Zafar, F., Bakaul, M., Parthiban, R.: Laser-diode-based visible light communication: toward gigabit class communication. IEEE Commun. Mag. 55(1), 144–151 (2017).

[24] IEEE draft standard for local and metropolitan area networks - Part 15.7: short-range optical wireless communications. IEEE P802.15.7/D3, pp. 1–412 (2018).

[25] Kamalakis, T., Ghassemlooy, Z., Zvanovec, S., Nero, Alves L.: Analysis and simulation of a hybrid visible-light/infrared optical wireless network for IoT applications. J. Opt. Commun. Netw. 14(3), 69–78 (2022).

[26] Wen, S. D., Hazry, D., Azizi, A. M., ST, H. A., & MH, T. (2024, February). Development of IoT-Enabled Smart Water Metering System. In 人工生命とロボットに関する国際会議予稿集 (Vol. 29, pp. 718-723). 株式会社 ALife Robotics.

[27] Easa, H. K., Majid, A., Al-Hatem, A. I., Othman, N. A., Bloh, A. H., Ali, A. H., & Kalmatov, R. (2024, April). Sustainability in Irrigation Practices Through 5G Optimization of Water Resources. In 2024 35th Conference of Open Innovations Association (FRUCT) (pp. 201-210). IEEE.

Analyzing Satellite Images by Convolutional Neural Network (CNN) Instance Segmentation Of Agricultural Fields

1st Atheer Joudah
Department of computer sciences
Faculty of Monastir
University of Monastir
Monastir, Tunisia
atheermubs@gmail.com

2nd Souheyl Mallat
Research Laboratory in Algebra,
Numbers theory and Intelligent Systems
Monastir, Tunisia

3rd Mounir Zrigui
Department of computer sciences
Faculty of Monastir
University of Monastir
Monastir, Tunisia

***Abstract*—This paper uses Convolutional Neural Network (CNN)-based deep learning to classify field-operated satellite images. Satellite image localization is used in pest control, segmentation, scene analysis, and tracking. Our investigation relies on satellite and CNN photos. In addition to the owner column, comprehension is crucial. We constructed a CNN classifier to properly detect fields and determine satellite imaging area in this work. Classification provides bounding quadrilaterals, which localize field satellite images better than rectangles. Post-noise convolutional neural networks get corrected regions. CNN preprocessing generates textual representations by aggregating related components, arranging them by size, and aligning them. This approach employs the famous Convolutional Neural Network. If CNN gives a text location a low confidence level, the user must choose an image for that field. We repeat text processing and compare the image to the original. The method concludes when all areas pass or the maximum attempts are spent. The output comprises field type, extracted text, and CNN reliability. CNN accuracy was 98.17% throughout 300 training and testing epochs. The suggested system used 70% data to train, 20% to test, and 10% to verify. We selected a dataset with various classes from a representative subset of the many agricultural sectors employed today to demonstrate the importance of the feature vector. This project utilizes Python-based deep learning. Our architecture contains three "head networks" that may generate end-to-end and simultaneous training instability. The head design component that fails model convergence may be hard to identify. After validating the single-head design idea, the functional heads were added gradually.**

Keywords— Satellite imagery, deep learning, agriculture fields, optimization, CNN, image analysis, segmentation, detection.

I. INTRODUCTION

With its unique viewpoint on the Earth's surface and capacity to extract spatiotemporal knowledge, satellite imaging has emerged as an essential source of data for several applications. Satellite technological developments have enhanced the availability of high-resolution and multi-spectral photography, offering rich and comprehensive information on our planet [1].

In addition to other areas, disaster management, urban planning, and transportation networks all greatly benefit from the use of satellite photography [2]. It facilitates decision-making based on evidence and resource management by enabling academics and practitioners to study and comprehend complicated spatial and temporal events. For solving a wide range of difficulties in several disciplines, the capacity to extract useful information from satellite data has become crucial.

Significant advancements have been achieved recently in the creation of algorithms and methodologies for the evaluation of satellite images. For satellite image identification, localization, and recognition tasks, deep learning methods, such as deep classifiers, have been effectively used [3]. These techniques make use of convolutional neural networks (CNNs) to identify objects and classify objects with high accuracy by automatically learning discriminative characteristics from the picture.

Additionally, field satellite image recognition using region-based CNNs has been implemented, allowing for the identification and delineation of particular regions of interest within the images [4]. This method enables the focused analysis and localisation of pertinent information, improving comprehension and choice-making across a range of applications.

It has also been investigated to use modified GrabCut algorithms to locate specific field numbers in satellite images [5]. With the help of these algorithms, field numbers may be precisely located and recognized while also properly segmenting and extracting specific regions of interest. The automated field number identification capabilities of CNN-based techniques using trained neural networks have also shown encouraging results [6].

Satellite imaging is used for purposes other than those found on Earth. For evaluating skewed pictures, especially in the context of intelligent transportation systems, a framework for vehicle satellite image identification has been presented [7]. To manage distorted viewpoints and differences in car license plates, this framework makes use of cutting-edge image recognition techniques.

The analysis and understanding of spatiotemporal patterns have been further improved by combining satellite images with other data sources, such as geographic information systems (GIS). Combining satellite images with GIS data enables thorough geographical analysis, enabling the extraction of priceless information and insights [8].

Researchers have created hybrid models, such the hybrid KNN-SVM model, for satellite image identification by taking use of developments in satellite technology and computing methods [9]. In order to increase accuracy and resilience when extracting spatiotemporal information from satellite data, these models incorporate the best aspects of many techniques [10].

II. Prepare Your Paper Before Styling

we present our proposed approach for the extraction of spatiotemporal knowledge from satellite images to predict changes in agricultural fields. The objective is to utilize the information extracted from satellite images to gain insights into the dynamic nature of agricultural fields, including field segmentation, character recognition, and classification. By understanding the changes that occur in these fields over time, we can make informed predictions about future developments and optimize various agricultural processes.
The chapter begins by outlining the key components of our proposed approach, including the techniques and methodologies employed for field segmentation, character recognition, and classification. We discuss the dataset used for training and testing our approach, as well as the preprocessing steps applied to the satellite images to enhance the quality of the extracted information.

A. Satellite Image Classification

The field was initially identified, followed by the subsequent need to ascertain its inherent characteristics. The research use a machine learning methodology to tackle a diverse array of issues. Numerous methodologies can be employed to address the task of image classification as documented in scholarly publications. The objective of employing these methodologies is to categorize the entirety of the image. In contrast to the current circumstances, it is imperative to refrain from making any presumptions regarding the incoming image beforehand. Nevertheless, there is a growing movement towards enhancing the process of extracting and curating visual features. A framework for classifying images based on the items they represent. The visual representation is depicted by a multi-layered approach, wherein the image is partitioned into individual cells and organized in a grid format. The number of rows and columns within this grid progressively expands as the level of magnification intensifies. The attributes of each cell are computed as an integral component of the investigation. The appearance of objects in a picture can be characterized by extracting Scale-Invariant Feature Transform (SIFT) features at regularly spaced points using four distinct radii. These concepts are systematically arranged using visual representations. Histograms with directed gradients are employed as a means of representing the many shapes of objects. The aforementioned values are subsequently computed across the entirety of the image at every level of detail in order to identify areas of significance. Zones of interest refer to geographical areas that exhibit comparable visual characteristics across a multitude of test photos. In order to accomplish this task, we exclusively employ these specific domains for the purpose of training a convolutional neural network.

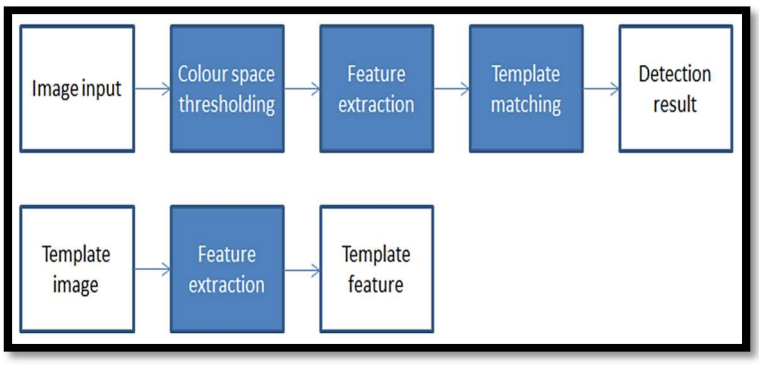

Fig 1. The processing on unprocessed raw image.

The research proposes a novel classification technique that, similar to its predecessor, utilizes information derived from grid cells. The initial stage of their methodology involves the creation of a feature vector by utilizing the retrieved computed descriptors at regular intervals. The research discovered that a linear function might be utilized as an effective approximation to the nonlinear function presented by the feature vector. The programming enables this occurrence. The authors further assert that neighborhood-aware descriptors, such as Scale-Invariant Feature Transform (SIFT), are insufficient.

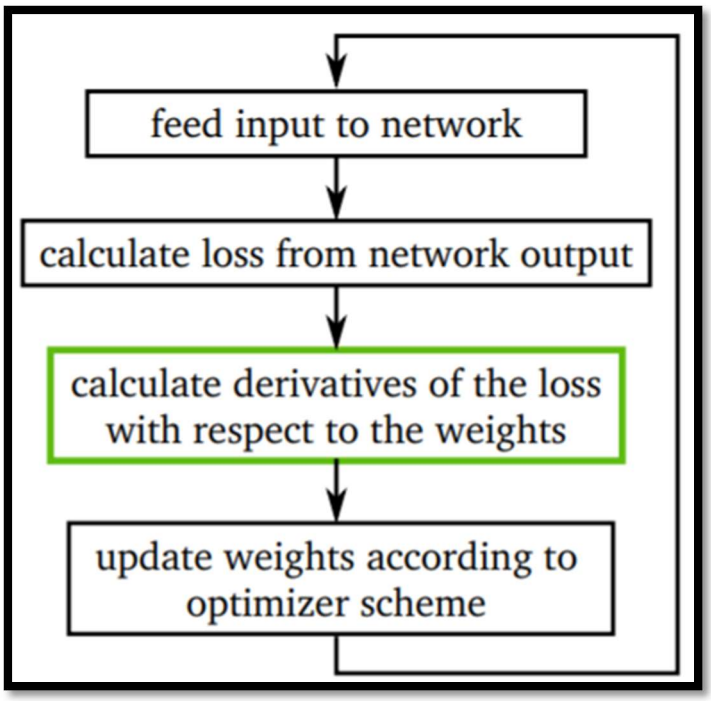

Fig 1. The proposed training pipeline with updated weights.

1) Feature Extraction

The feature vector employed in our study incorporates two key aspects: the texture of the field, which is represented by histograms of local binary patterns, and the color of the field, which is utilized to distinguish between fields of the same structural type but varying colours. The final criterion for distinguishing between fields that have similar information but vary in size is the size ratio of the respective fields. In order to achieve this objective, a convolutional neural network is employed. As a result, they are eliminated through the process of preprocessing. The aforementioned methods are

implemented on every extracted field region that was provided by the preceding stage. The field areas are derived from the unaltered, unscaled field image. Hence, the magnitude of the area is contingent upon the dimensions of the image. It is possible for input areas to have many lines of field.

2) Field Localization with Local Binary Patterns

The subsequent feature in the feature vector consists of Local Binary Pattern (LBP) histograms, which are computed and added. This characteristic encapsulates the inherent textural properties of the subject matter. The Local Binary Pattern (LBP) codes are obtained through a process of comparing the pixel values of a specific number of neighboring pixels with the value of the central pixel. The pixels in the vicinity exhibit a uniform distribution around the central pixel, so constituting a circular pattern with a designated radius. A neighboring bit is assigned a value of zero if and only if its corresponding value in the code exceeds the value of the centre pixel. If the value of the adjoining pixel is smaller, the corresponding bit is assigned a value of 1. The resulting image possesses identical pixel dimensions to the original image and is characterized by the presence of a Local Binary Pattern (LBP) code assigned to each individual pixel.

The L-channel is extracted from the field image subsequent to its conversion to the CIE L*a*b color space due to its inclusion of the intensity values. Subsequently, a Gaussian blurring technique is employed, utilizing a kernel size of 7x7 pixels, in order to effectively mitigate any potential noise that may be present within the Local Binary Pattern (LBP) features. Subsequently, the LBP codes are computed based on the distorted image. In our methodology, a radius of LBPRadius is employed together with a total count of numLBPNeighPixels for the adjacent pixels. Subsequently, the image containing the Local Binary Pattern (LBP) codes undergoes the identical grid structure employed for color extraction. A histogram is generated for the codes of each cell, utilizing bins of size LBPHistSize. The cell histograms provide the frequency distributions of events inside the field, categorized by direction.

TABLE I: GRID SEARCH RESULTS FOR THE FEATURE EXTRACTION PARAMETERS. FOR EACH PARAMETER, THE POSSIBLE VALUES AND THE FINAL VALUE IS LISTED.

Parameter	Possible values	Final value
numColsRows	10, 20, 30, 40, 50, 60	20
numLBPNeighPixels	4, 8, 16	4
LBPRadius	2, 4, 8, 16	16
LBPHistSize	30, 40, 50, 60	60
NUMLBPLAYERS	100, 200, 300	300

3) Normalization with Feature Vectors

For each image, a final feature vector is generated and employed for both training and classification purposes. This vector encompasses many elements such as the aspect ratio of the field image, median color values, and histograms of LBP codes. The aforementioned features were derived by employing a collection of parameters denoted exclusively by their symbolic names, namely numColsRows, numLBPNeigh-Pixels, LBPRadius, and LBPHistSize. The utilization of a convolutional neural network is integrated with the LBP approach. The significance of this matter lies in the considerable variation in camera resolution across different capture systems. The relative size ratio is of comparatively lesser significance among the three criteria, and it is noteworthy to acknowledge this fact. However, this attribute of the arena serves as a distinguishing factor amongst formats that are essentially comparable but possess different aspect ratios. In the photographs depicting field regions, the presence of structures that are not inherent to the field can be observed. These structures may arise due to the demarcation lines surrounding the field or the interfaces between adjacent field areas. Additionally, the presence of soil particles on the field might contribute to the appearance of non-field elements in the images. The inclusion of additional structures significantly diminishes the output quality of most convolutional neural network (CNN) systems, which are primarily designed for scanning separated agricultural areas.

4) Geometrical Analysis

The absolute geometrical analysis is computed by utilizing the gradient magnitude of the satellite image. When dealing with images that exhibit a gray value gradient, such as those affected by rust stains, it has been observed that employing gradient-based processing techniques yields superior results compared to adaptive thresholding methods. In numerous instances, the implementation of conventional thresholding may result in the generation of extensive black zones that are unsuitable for subsequent processing. An adaptive threshold is calculated based on the minimum and maximum gradient values. This threshold is then used to filter out and assign a value of zero to all data points that fall below it. The threshold is determined by performing calculations on a histogram consisting of 256 bins, which represent the magnitude values. Subsequently, we proceed to identify the bin with the highest numerical value. This assumption is made based on the premise that the image generates the highest attainable quantity of gradients. Applying a blurring operation prior to calculating the gradient would effectively eliminate the presence of the embossed field, hence rendering a predetermined thresholding value inappropriate. In order to proceed with the processing, we employ an adaptive thresholding technique on the filtered image. The block size used for this thresholding is set to be half the height of the image. Additionally, we normalize the resulting thresholded image to a range of 0 to 255. The provided illustration showcases a binary image of a printed field that is devoid of rust stains. Presented here is an additional example of a visually perceptible embossed field characterized by a high level of auditory disturbance.

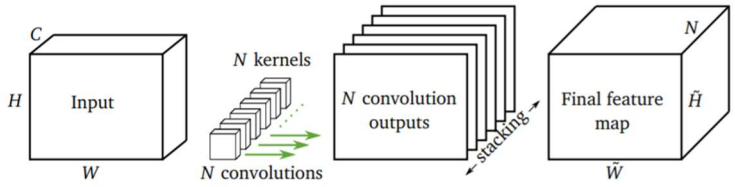

Fig 2. The proposed layers of CNN based on the geometrical analysis.

B. Convolutional Neural Network (CNN)

A convolutional neural network is composed of multiple interconnected layers, wherein each layer is trained

individually using a subset of the complete dataset. Bagging is a technique that involves generating subsets of items using a purely random and restitution-based approach. This implies that a sample has the potential to exhibit many occurrences. In the process of layer training, sample sets are assigned to nodes in a random manner, utilizing only a portion of the feature vector. In this particular scenario, the divisions are performed by utilizing a fractional value derived from the square root of the overall count of features. The division of the label histogram that is chosen is the one that exhibits the highest reduction in entropy and, thus, the greatest amount of information gain. In the given scenario, the learning process is considered to be finalized when either the formation of CNN-Layers occurs or when the anticipated classification error is below 1%. During the training process, an estimation of the error is generated by classifying samples that were not selected by the bagging approach. The convolutional neural network does not undergo any pruning in its layers. The input data is transmitted via each individual tree, and the final class label is determined by a majority vote.

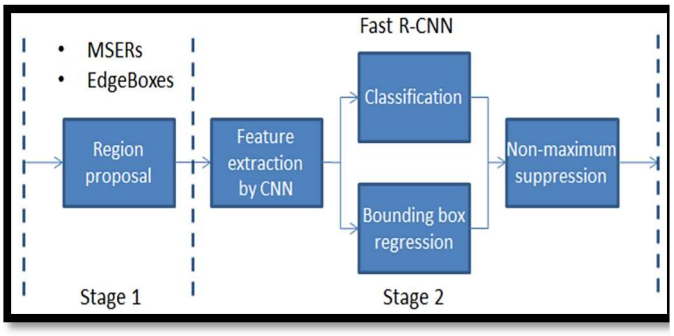

Fig 3: The employment of CNN and MSER based proposed system for satellite field image classification.

Convolutional neural networks are employed because to their inherent utility. We contend that the inclusion of additional layers does not result in overfitting. Given that a larger numerical value yields greater precision, it can be employed with a high level of confidence within this particular context. Nevertheless, when the number of layers escalates, the improvement in classification accuracy starts to plateau. Moreover, it is worth noting that the duration of training exhibits an exponential growth pattern as the number of layers in a neural network increases. However, the time required for classification demonstrates a linear growth trend. Given the ability to analyze each tree simultaneously, both training and classification tasks exhibit exceptional speed. The efficacy of the categorization is a crucial determinant. Supervised deep learning involves the comparison of various widely-used methodologies. The aforementioned techniques encompass Support Vector Machines (SVMs), boosted layers, Convolutional Neural Networks (CNNs), and various other network architectures. The test dataset contains binary classification questions. Given that no individual possesses exceptional problem-solving abilities in every domain, the findings suggest that the existence of a universally optimal algorithm is unfounded. In their experiments, it has been seen that convolutional neural networks, bagged layers, and calibrated boosted layers have strong performance. CNN algorithms are extensively employed in the domain of sign recognition. The test dataset has more than 5,000 photos distributed across 43 distinct categories. Based on the results of the study, it has been determined that convolutional neural networks rank as the third most effective deep learning algorithm.

The performance of convolutional neural networks is assessed in this study. This work utilizes highly reliable methods to accurately identify and locate satellite pictures. The process of identifying the satellite pictures involves the identification of many smaller sections inside the larger region. The majority of Convolutional Neural Network (CNN) systems are specifically engineered to identify and classify objects or features inside images. Due to the relatively lower presence of extraneous elements in our field images compared to those depicting the natural world, the utilization of the SWT or any other comparably intricate technique is unnecessary. In our approach, we utilize a comparable technique that relies on Maximally Stable Extremal Regions (MSER) and grouping algorithms to identify agricultural regions and textual content inside satellite imagery. In addition to the visual representation of the extracted vertical field, we possess a comprehensive inventory containing the designations, geographical positions, and nature of the extracted components. Due to the potential lack of precise extraction in the field, it is necessary to make modifications to the defined regions in order to accurately reflect the content of the field.

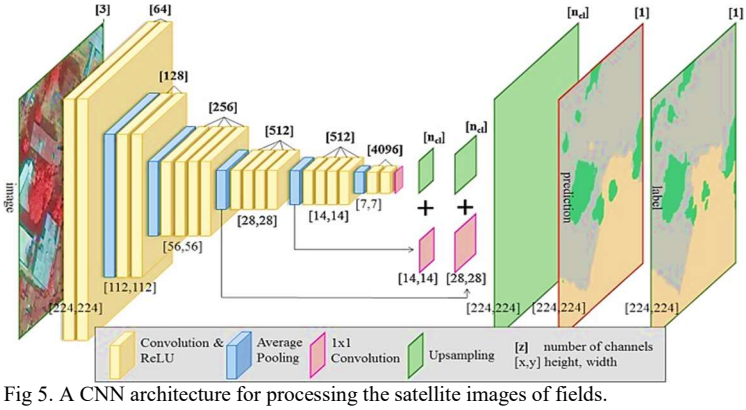

Fig 5. A CNN architecture for processing the satellite images of fields.

It is vital to distinguish between the conventional approach of field image location and the more sophisticated method of dynamic field image identification, as both necessitate a two-way dissemination framework. The selection of the size of the micro network carries significant ramifications for our architecture, necessitating thorough investigation. The utilization of traditional methods to mitigate field image violence may not be accurate or prompt in addressing the evolving requirements of the field, particularly when dynamic and responsive injection or absorption by distributed generation and load variation in the distribution system result in reduced power quality and field violations.

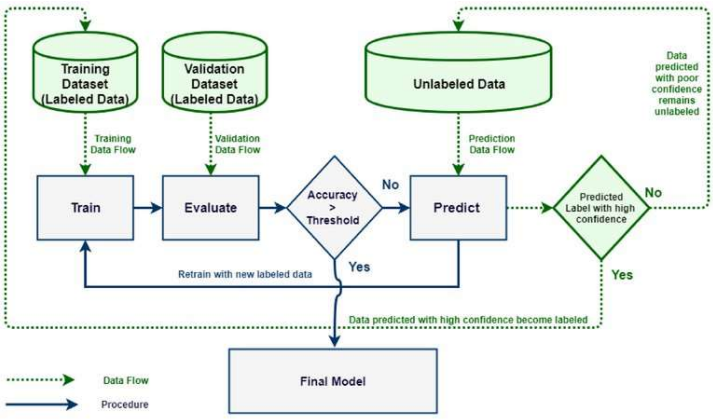

Fig 4. The CNN model training and validation with data prediction for labels.

Convolutional neural networks are composed of several layers, where each layer is conditioned on a specific subset of the training dataset. The components of the subsets are selected in an arbitrary manner and subsequently adjusted through the process of Stowing. Hence, it is possible for a field segmentation example to occur multiple times. The samples within each hub are distributed in an asymmetrical manner, taking into account the key features of the component vector. Various aspects are utilized to form the components that constitute a fraction of the square base, assuming all other factors remain constant. In the process of field segmentation, the selection of the name histogram split that results in the most significant decrease in entropy and, thus, the highest amount of data gain is employed. Learning is considered complete when either CNN-Layers are generated or the evaluated order error is below 1%. It is possible that an error was made during the selection of tests for field segmentation in the stowing procedure. Consequently, these tests have been grouped together for the purpose of error analysis. The layers of the Convolutional Neural Network have not been pruned. The output of each tree is generated depending on the available information, and the final class name is established through a majority voting process. Artificial neural networks are widely utilized in the domain of field segmentation due to their numerous advantageous attributes. Our argument posits that the phenomenon of overfitting does not manifest itself when the quantity of layers within a model is augmented. The utilization of large numbers can be employed with confidence, as they enhance precision. Nevertheless, as the number of layers grows, the degree of improvement in the precision of field segmentation rapidly decreases. The inclusion of additional layers not only extends the setup duration but also maximizes the potential for character development. Rapid planning and preparation can be achieved due to the similarities in managing individual trees. Ultimately, the implementation of the plan is a crucial determinant. Artificial neural networks, support vector machines, and assisted layers are among the prominent techniques utilized for field segmentation, which are extensively examined within the context of controlled deep learning. The process of testing involves the utilization of parallel characterization problems inside the dataset. The study operates on the premise that a universally acknowledged formula is lacking due to the absence of a comprehensive answer for all conceivable scenarios. The experimental results indicate that the utilization of collapsed layers, artificial neural networks, and aligned supported layers yields the most optimal visual experience.

.

III. EXPERIMENTATION AND RESULTS

We delve into the heart of our research journey, presenting the detailed experimentation and the results obtained from our proposed model for predicting spatiotemporal changes from satellite images. The ability to forecast changes in the Earth's surface over time has significant implications for a wide range of applications, including environmental monitoring, urban planning, disaster management, and transportation systems. Leveraging the vast amount of information captured by satellite imagery, we aim to develop a robust and accurate predictive model that can provide valuable insights into the dynamic evolution of our planet.
The primary objective of this chapter is to evaluate the performance of our proposed model and examine its efficacy in capturing and predicting spatiotemporal changes from satellite imagery. We embark on a systematic exploration of the experimental setup, including dataset selection, preprocessing techniques, model architecture, training process, and evaluation metrics. By conducting rigorous experiments and analyses, we seek to validate the effectiveness of our model and provide concrete evidence of its predictive capabilities.

A. Experimental Setup

In the event that a field region exhibits a CNN confidence score below a certain threshold, we shall proceed to solicit additional field photos for further examination and analysis.

1) Description of Application

The presented with the opportunity to request a fresh image depicting the surrounding area of the field where the majority of issues have taken place. Both the field that has been retrieved and the initial outputs from the Convolutional Neural Network (CNN) are retained for future comparison. Is it important to generate a new image in the event that the recognition rate in a certain location falls below 80% on average? The objective is to acquire a fresh representation for the section of the image where the majority of errors have manifested, specifically the regions of disjunction located at the top, bottom, left, and right. The concept of "Binary Robust Invariant Scalable" refers to a computational approach that is characterized by its ability to handle binary data, its robustness to variations and noise, and its scalability to larger datasets Key-point descriptors are generated by extracting key-points from both the new picture and the stored field using Oriented FAST and Rotated BRIEF (ORB) detectors. ORB and BRISK are employed because they exhibit operational similarities to Convolutional Neural Networks (CNNs) while also requiring less processing power and memory resources. A revised input image has been provided, which has been appropriately zoomed in to focus on the specific area of interest within the field. Additionally, a representative screenshot has been extracted from a file that accurately depicts the correct orientation of the field. Furthermore, the coordinates of the new image relative to the reference field are also presented, together with the extracted key points and computed matches. The visible parts undergo a clockwise rotation of 90 degrees, resulting in new dimensions that closely resemble those of the original input image. The individual processing and warping of each region allows for simultaneous execution of the process, resulting in reduced resource consumption compared to processing the full image as a whole. The procedure of preprocessing and the succeeding phases of Convolutional Neural Network (CNN) are iteratively performed for each consecutive region. The newly discovered information is included into the preexisting data, and only the region with the highest level of confidence according to CNN is preserved. In instances where the predetermined threshold of retirees has not been attained, however certain regions continue to exhibit low recognition scores, a subsequent image is captured and subjected to the identical evaluation process. In the event of method failure and subsequent user request for a reattempt, the

user will receive notification regarding the specific sections that want improvement. The experimental results demonstrate the output of the Convolutional Neural Network (CNN), the input images for the three domains, and the required supplementary image.

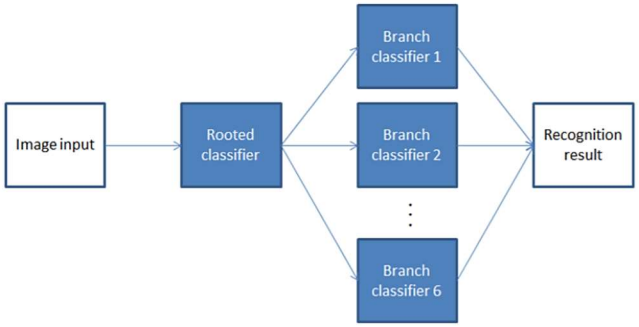

Fig 7. A breakdown cases for extracting the recognition for number of fields at the same time.

2) Description Dataset

The dataset is named "Field Satellite Image Detection." In Multiple Locations, Multispectral, SAR, Optical, and **the size for 510 GB in date Jun 6, 2019**, Classification, Semantic segmentation, Multisensor data fusion, Other The list provided by the user is utilized to ascertain the appropriate storage method for each set of grouped photographs, taking into consideration factors such as content kind, area name, and reference field location. The identified region is obtained from a collection of photos in the dataset, where it is assigned to the designated zone with the least Euclidean distance between the centers of the two bounding boxes. The probability of encountering inaccurate matches with this uncomplicated mapping technique is high, sometimes caused by erroneous character grouping or the absence of field regions on the field. Consequently, these correspondences are employed to approximate a rigid transformation. By implementing the calculated transformation on the coordinates of all user-defined regions, the resulting field regions are customized in terms of their sizes and locations to match the recognized regions. Currently, we possess a compilation of field regions accompanied by their corresponding coordinates on the comprehensive field image. The images pertaining to the desired information are saved within specific regions and subsequently transformed by the Convolutional Neural Network (CNN) into machine-readable fields. The dataset can be acquired from the link: https://www.intelligence-airbusds.com/satellite-image-gallery/.

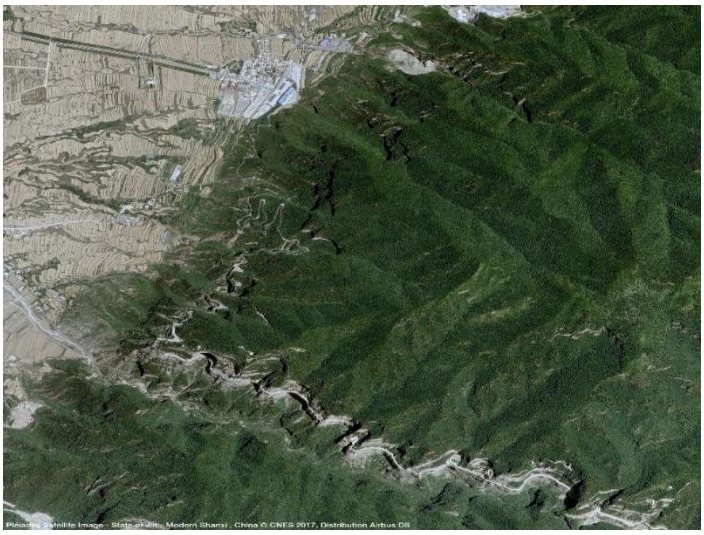

Figure III.1: The integrated satellite image being aligned to the frames in the same angle and direction.

3) Application Result For Proposed Approach

a) Step one

we employ a median blur technique on the photos. The study presents the classification results for the entire dataset utilizing both the complete feature vector and Local Binary Patterns (LBP) features, focusing specifically on various sizes of median blur kernel. Leave-one-out cross validation is not utilized for this evaluation. Conversely, the classifier is trained using each individual image from the dataset. Once all the photographs have been subjected to blurring, it becomes possible to recover the feature vector that is utilized for classification. Hence, it can be concluded that both feature vectors effectively categorize all photos with high accuracy in the absence of blurring.

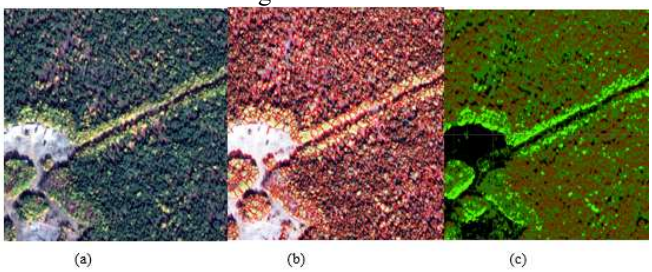

Fig 8. The (a) input image, (b) segmented image and (c) processed satellite based imagery for fields using convolutional neural network.

The feature vector, which has N distinct properties, is computed for each domain and afterwards transmitted to the convolutional neural network for the purpose of labeling. During the training process, a convolutional neural network employs an efficient splitting technique to partition the data into m features. Each feature is derived from the feature vector at a specific node. All trees within the forest exhibit an equal amount of features (m), which serves as a determining factor for the intensity of the interconnections between the layers and the resultant classifications they generate. The efficacy of the forest's classification performance is enhanced by reducing inter-layer connectivity and employing more robust classifiers. The improvement of classifiers is shown to be positively associated with an increase in m, hence enhancing the correlation between them. Conversely, a

decrease in m is found to have a detrimental effect on classifiers' performance and reduces their correlation. The study presents the precision and recall metrics for three common values of active variables, where the square root of the variable count is a frequently employed threshold for creating splits. Consequently, it is advisable to commence utilizing this numerical value. The research presents the pairwise relationships among the three criteria. The influence of the LBP variables on the result appears to be more pronounced compared to the influence of the size ratio. The utilization of just LBP features results in a decrease of 0.26 percentage points in precision compared to the final feature vector, while the recall stays unaltered. Due to the limited availability and poor quality of images in the collection, the inclusion of color data has minimal influence on the outcome of the categorization process. In order to replicate the visual effect of content distortion in areas of blurriness, we employ a median blur technique on the photos. The study presents the classification results for the entire dataset utilizing both the complete feature vector and Local Binary Patterns (LBP) features, focusing specifically on various sizes of median blur kernel. Leave-one-out cross validation is not utilized for this evaluation. Conversely, the classifier is trained using each individual image from the dataset. Once all the photographs have been subjected to blurring, it becomes possible to recover the feature vector that is utilized for classification. Hence, it can be concluded that both feature vectors effectively categorize all photos with high accuracy in the absence of blurring.

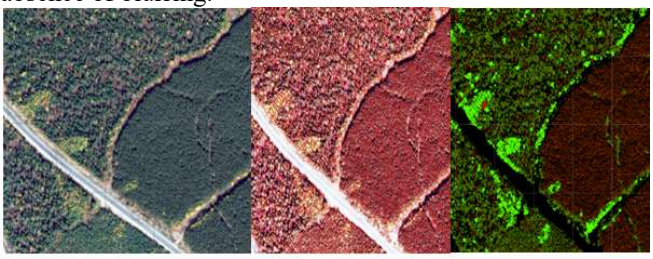

Fig 9. The (a) input image, (b) segmented image and (c) processed satellite based imagery for fields using convolutional neural network.

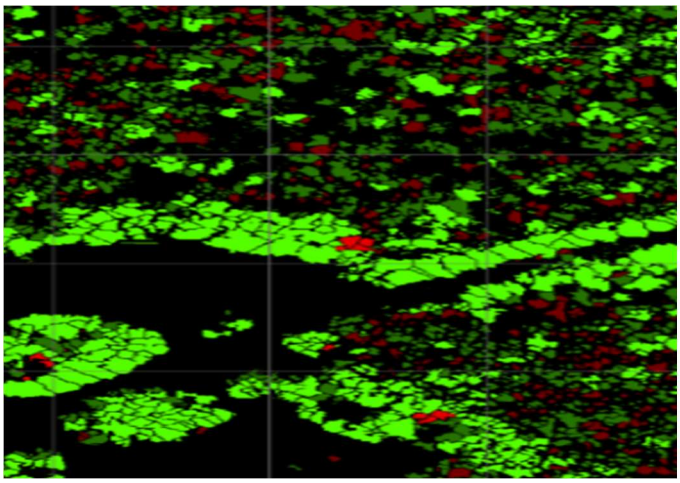

Fig 10: Samples of typical analyzed field regions where the CNN output improves after preprocessing. For each sample, the unmodified image, the preprocessed region, and the corresponding CNN output are listed. The value in the score columns is the CNN recognition confidence. For each sample, the output after preprocessing is correct.

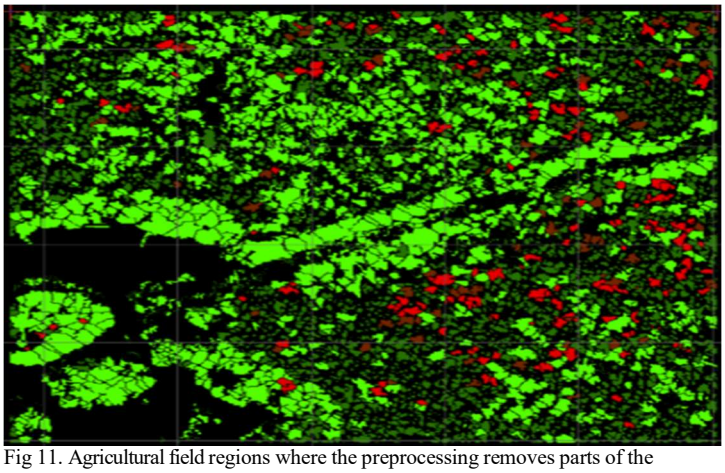

Fig 11. Agricultural field regions where the preprocessing removes parts of the noisy field images. The unmodified and preprocessed regions, as well as the resulting CNN output is displayed. The value in the score columns is the CNN recognition confidence. In each region the preprocessing removes some part of the content, specifically commas and portions of agricultural fields..

IV. CONCLUSION

Through deep learning, this article solved the challenge of detecting, classifying, and extracting data from a set of fields. An operator uses image processing methods, including a convolutional neural network (CNN), to assess extracted information and gather data on satellite image elements. This may involve field cropping or ROI creation. The machine learning algorithm localizes, segments, and classifies the input satellite image. Convolutional Neural Networks (CNN) categorization uses color data, Local Binary Patterns (LBP) histograms, and field size ratios. Each variety had its unique field arrangement, which determined field segment placement. Comparing preset fields to field-identified fields helps correct field extraction issues. A convolutional neural network receives revised regions after noise removal. The CNN is preprocessed by removing superfluous components, organizing data into coherent lines of sight, and using size-based filtering. The popular CNN method is used. If a Convolutional Neural Network (CNN) displays a low confidence score for a field location, the user will be instructed to get a new picture. The new picture is compared to the old one, and field processing is repeated. After all regions pass or the maximum number of tries is reached, the procedure ends. The detected field type, areas containing the extracted field, and CNN reliability make up the result. The CNN achieved 98.17 percent accuracy after 300 epochs of testing and training. The proposed system was trained with 70% of the data, tested using 20%, and verified with 10%. To highlight the value of the feature vector, a dataset with several classes, each representing a subset of the fields being used, was chosen. Traditional and modern illustrations exist. The classification result was considerably impacted by local binary pattern histograms, color characteristics, and field size ratio. The combined feature vector showed that the classification was resilient to shadows, specular reflections, and inadequate illumination causing blurriness and imprecise coloring. We also found that training the CNN with the test field's typography reduces recognition mistakes. The remaining errors are caused by field region preprocessing, which removes punctuation marks that are smaller or blend with the field boundaries. This is because the filtering parameters were optimized for historical survey data. High-stringency field region preprocessing removes fading or flaking letters. When the field and backdrop are not well defined, field localization may be inaccurate or impossible.

This happens when field borders are overpainted, or moss and dirt accumulate. Using a Convolutional Neural Network (CNN) trained on typefaces from three fields yielded promising results throughout testing. Photographing in reflective settings is difficult without a manual focus control in the prototype. After prolonged exposure to the environment, a field's surface may deteriorate rapidly, limiting the possibility of many of these fields being connected with devices. The prototype retrieves data from fields and runs at a reasonable speed for real-world applications.

.

REFERENCES

[1] Rizvi, S.; Patti, D.; Björklund, T.; Cabodi, G.; Francini, G. Deep Classifiers-Based Satellite Image Detection, Localization and Recognition on GPU-Powered Mobile Platform. Future Internet 2017, 9, 66.

[2] Rafique, M.A.; Pedrycz, W.; Jeon, M. Field satellite images detection using region-based convolutional neural networks. Soft Comput. 2018, 22, 6429–6440.

[3] Salau, A.O.; Yesufu, T.K.; Ogundare, B.S. Field field number localization using a modified GrabCut algorithm. J. King Saud Univ. Comput. Inf. Sci. 2019.

[4] Kakani, B.V.; Gandhi, D.; Jani, S. Improved CNN based automatic field number field recognition using features trained neural network. In Proceedings of the 2017 8th International Conference on Computing, Communication and Networking Technologies (ICCCNT), Delhi, India, 3–5 July 2017.

[5] Arafat, M.Y.; Khairuddin, A.S.M.; Paramesran, R. A Vehicular Satellite Image Recognition Framework for Skewed Images. KSII Trans. Internet Inf. Syst. 2018, 12.

[6] Available Online: https://melabglobal.com/blogs/news/why-use-field-field-recognition-parking-system

[7] Ansari, N.N.; Singh, A.K.; Student, M.T. Field Number Field Recognition using Temfield Matching. Int. J. Comput. Trends Technol. 2016, 35, 175–178.

[8] 12. Samma, H.; Lim, C.P.; Saleh, J.M.; Suandi, S.A. A memetic-based fuzzy support vector machine model and its application to satellite image recognition. Memetic Comput. 2016, 8, 235–251.

[9] Tabrizi, S.S.; Cavus, N. A Hybrid KNN-SVM Model for Iranian Satellite Image Recognition. Procedia Comput. Sci. 2016, 102, 588–594.

[10] Available Online: https://medium.datadriveninvestor.com/convolutional-neural-networks-explained-7fafea4de9c9

[11] Niu, B.; Huang, L.; Hu, J. Hybrid Method for Satellite Image Detection from Natural Scene Images. In Proceedings of the First International Conference on Information Science and Electronic Technology, Wuhan, China, 21–22 March 2015; Atlantis Press: Paris, France, 2015.

[12] Arafat, M.Y.; Khairuddin, A.S.M.; Khairuddin, U.; Paramesran, R. Systematic review on vehicular licence field recognition framework in intelligent transport systems. IET Intell. Transp. Syst. 2019.

[13] Chai, D.; Zuo, Y. Extraction, Segmentation and Recognition of Field's Satellite Image Numbers. In Advances in Information and Communication Networks; Arai, K., Kapoor, S., Bhatia, R., Eds.; Springer International Publishing: Cham, Switzerland, 2019; pp. 724–732.

[14] Dhar, P.; Guha, S.; Biswas, T.; Abedin, M.Z. A System Design for Satellite Image Recognition by Using Edge Detection and Convolution Neural Network. In Proceedings of the 2018 International Conference on Computer, Communication, Chemical, Material and Electronic Engineering (IC4ME2), Rajshahi, Bangladesh, 8–9 February 2018; pp. 1–4.

[15] Wang, W. et al. "Car satellite image detection based on MSER." 2011 International Conference on Consumer Electronics, Communications and Networks (CECNet) (2011): 3973-3976.

Predicting Grating Sensor Sensitivity Using Artificial Neural Networks: A Comparative Study with RCWA

Imed Sassi[1*], Mounir Ben El Hadj Rhouma[1]

[1]Université de Monastir, Institut Préparatoire aux Études des Ingénieurs de Monastir, Laboratoire d'Études des Milieux Ionisés et Réactifs (EMIR), 5019 Monastir, Tunisie

[*]Correspondence author: fss_imedsassi@yahoo.com

Abstract We predict in this work the values of the sensitivity by using the neural network. The data processing is conducted using MATLAB software. The prediction is based on a data called the input composed of a matrix (49×5), and the output data, called the target data, is a matrix colon composed of 49 values of the sensitivity computed by the rigorous coupled waves analysis (RCWA), published previously. The output data is predicted by using the ANN technique. Our goal is demonstrated the effectiveness of the ANN method to predict the results of the sensitivity of a grating structure witch work as sensor. A comparative study between the sensitivity results of the RCWA and those of the ANN show an absolute error (AE) ranged from 0.16 to 62.19 nm/RIU and a relative error (RE) ranged from 0.016 to 6.93%. The validation of our prediction is influenced by the geometric parameters which characterised the grating structure. The best validation of the ANN tool which is characterised by a relative error of 0.016% is obtained for specific parameters.

Keywords: Grating structure; perfect absorber sensor; sensitivity; ANN tool, comparative study

1. Introduction

In recent years, the using of the artificial intelligence in several domains is demonstrated by various applications in the scientific research [1-3], the agriculture [4, 5] and the medicine [6, 7]. The optimization of fiber optic SPR sensor parameters with the ANN technique is reported [1]. The implementation of machine learning optimization provides perfect prediction accuracy across various parameter combinations [2]. A deep neural network (DNN) is used to associate the spectral response of the device with the corresponding structural parameters [3]. In the domain of agriculture, the ANN is used to identify grain weevil in wheat kernels [4], a development of a model using ANN to predict soybean harvest area, yield, and production and compared with classical methods of time series analysis [5]. The progress of the AI in several fields of medicine, such as treatment of cancerous diseases, pharmaceutical development, and clinical trial management has been investigated [6]. In addition, Lakhani P et al. use the convolution neural network for classification the pulmonary tuberculosis [7].

Surface Plasmon Resonance (SPR) is an important phenomena used to detect various chemical or biological entities in aqueous solutions [8-11]. The SPR phenomena is realised by interaction between light and the configuration, for specific conditions. By using the technique, the ANN classifier has been developed to identify the structural geometry of a diffraction grating from its measured ellipsometric signature [8]. The detection of hemoglobin in blood samples by using an SPR biosensor assisted by Ag, Black Phosphorus (BP), and TiO2 Is reported by I. Sassi et al. [9]. The gold grating structure is used for detection the chemical or biological entities in aqueous solutions [10]. The optimized behaviour and the performance of a multi-layered structure are investigated using the ANN prediction model [11].

In this work, we present a comparative study between the sensitivity results provided by the RCWA and those of the ANN tool. The effects of some parameters (which characterized the device and the incident light) on the comparative study are demonstrated. This work show significant results provided of the ANN tool for the parameter sensitivity. The rest of this manuscript is arranged in the following sections. Section 2 describes the theory of this work, followed by the prediction of the sensitivity by using the artificial neural network (ANN) in section 3. Section 4 provides a conclusion of this paper.

2. Theory

The rigorous coupled waves analysis (RCWA) is an efficient method used to compute the property called the absorbance of a grating structure. The RCWA method is reported by several authors [12, 13]. The material of the grating structure is the gold square. The parameters of the grating are the grating period p, the coefficient f

(ratio between ridge (a) and period), and the grating height h. An electromagnetic plane wave is interacted with our device under the incident angle θ and the conical angle φ (see Fig.1).

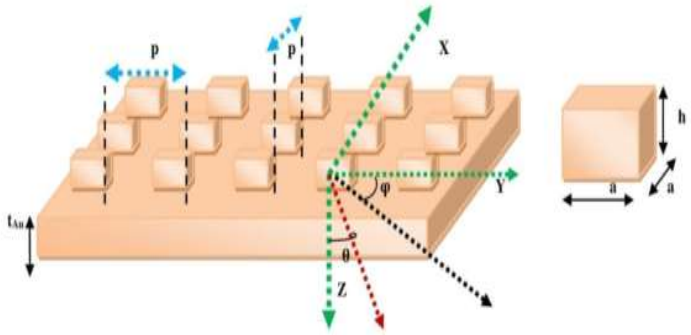

Fig. 1 Configuration of the grating structure.

Parameters: $a = f * p$, $0 < f < 1$.

Our numerical code (in MATLAB language) based on RCWA method is previously validated and used for studying a grating structure, which works as an infrared thermal source or perfect absorber sensor [12].

Our structure is used as a refractive index sensor; its operation is based on surface Plasmon resonance (SPR). A small change in the refractive index of the sensing medium causes a change in the behavior of the absorbance spectrum at resonance. Sensitivity is the important parameter used to examine the sensor's performance. The sensitivity of the sensor is defined as the ratio between the variation of the parameter characterizing the SPR, the resonance wavelength: λ_{Res} and the refractive index: n_1. The definition is as follows [14]

$$Sensitivity,\ S\ (\lambda_{inc}) = \Delta\lambda_{Res}/\Delta n_1, \quad (1)$$

3. Prediction of the sensitivity by using the artificial neural network (ANN)

ANN is a tool used to solve nonlinear functions related to various input and output datasets and is capable to provide the output data. The output values at this stage are compared to the actual data (computed by using a numerical code) and the deviation is computed. If the deviation value is not small enough, the weights are updated and a new cycle is initialized. This procedure is repeated several times until the deviation between the actual data and the output data is weak. To improve the ANN training, we choose the best values of the follows parameters: the number of hidden layers (N_HL), the number of neuron in hidden layer (N_NHL), the number of iterations, the transfer function (AF), the training function (TF), the adapting function (ALF), and the performance function (PF) is the mean square error (MSE). The selected ANN properties are presented in **Table 1.**

Table 1 The ANN properties

Network type	N_HL	N_NHL		AF		TF	ALF	PF
Feed-forward backprop	2	Layer1	Layer2	Layer 1	Layer 2	TRAINLM	LEARNGDM	MSE
		10	1	TAMSIG	PURELIN			

In order to test the ability of the ANN to predict the values of the sensitivity with negligible error, we calculate the sensitivity for the same input parameters. For this work, at fixed values of conical angle ($\varphi = 0°$) and gold thickness layer (t_{Au} = 0.25 nm), the sensor performance depends on 5 variables: the refractive index (RI) of sensing medium, the incident angle, the coefficient f of the grating, the grating height h and the grating period p. It consists of 9 different RI values from 1.375 to 1.575 with step of 0.025, 10 different incident angle: 0, 6, 12, 24, 36, 48, 60, 72, 78, and 84 degree, 10 different coefficient f: 0.1, 0.2, 0.3, 0.4, 0.5, 0.6, 0.7, 0.8, 0.9, and 0.95, and 10 different values of grating period p: 610-700 nm, and 10 different values of grating height h: 41, 45,49, 51, 53, 57, 59, 61, 63, and 65 nm. The output layer is the sensitivity: S (nm/RIU). The architecture of the NN used in this study is presented in **Fig.2**.

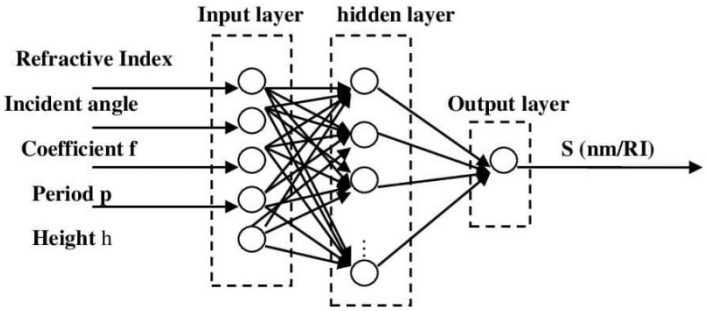

Fig. 2. The architecture of the neural network (NN).

The MATLAB R2014b with its Neural Network Toolbox was used to train the network. We train the network several times until we reach the best results concerning the regression curves. In the **Table 2**, we present the regression results predicted by using the ANN.

Table 2 The enhancement of the regression (R) results by the increasing of the number of training

Order of Training	2	19	37	45	56	105	130
Number of Iterations	612	1000	1000	**1000**	1000	1000	1000
R (Training)	0.96061	0.97184	0.98406	**0.99318**	0.99403	0.98057	0.97195
R (Validation)	0.97018	0.99161	0.99964	**0.99671**	0.99984	0.99941	0.99511
R (Test)	0.99614	0.99758	0.99927	**0.99929**	0.99743	0.98483	0.99792
R (All)	0.97526	0.9796	0.98928	**0.99548**	0.99512	0.98519	0.98519

It is remarked that for the same number of the iterations (= 1000), an increasing of the number of training (2, 19, 37, 45, 56, and 56), leads an enhancement of the R validation. The more significant values of the R training; the R validation, the R test, and the R all is obtained for the order of training equal to 45. The 45th training is characterized by the R (training) = 0.99318, R (validation) = 0.99671, R (test) = 0.99929, and R (All) = 0.99548. We obtain approximately the same value of regression (All) for the 45th, the 56th, 105th, and the 130th training.

For the latest number of training (= 130), we present in **Fig. 3**, the best results of the regression, corresponded to the best values of the sensitivities, predicted with the ANN technique. More clearly, **Fig. 3** shows the relationship between the output of the networks and the targeted values obtained from numerical results, as visualized through regression charts during the training, validation, and testing phases.

In order to test the ability of the ANN to predict the output values of the sensitivity with negligible error, we present in **Table 3** the results obtained through the RCWA approach and those of ANN. A comparison between the two approaches shows a great agreement between several sensitivity values (presented in italic form). For the comparison, we define the absolute error (AE) and the relative error (RE), presented as follows:

$$AE = |S_{RI}(ANN) - S_{RI}|, \quad (2a)$$

$$RE\ (\%) = AE/S_{RI}. \quad (2b)$$

Note that the significant values are indicated in red and italic type. It is remarked that the values of RE (%) are ranged from 0.016 to 6.93%, for the considered parameters of our sensor. However the AE is ranged from 0.16 to 62.19 nm/RIU, approximately. This implies that the ANN is a powerful tool for predicting accurate results. The best value of the prediction is obtained for specific parameters: refractive index = 1.5, incident angle = 36 degree, coefficient f = 0.5, grating period p = 610 nm, and the grating height = 57 nm. The corresponded values of the latest case of the AE (nm/RIU) and the RE(%) are 0.16 nm/RIU and 0.016%, respectively.

Table 3 The comparison between the RCWA and the ANN sensitivity results for the same parameters of the proposed sensor structure.

RI	Incident angle	f	p	h	S_{RI}(RCWA)	S_{RI}(ANN)	AE	RE (%)
1.375	36	0.7	610	57	1000	1000.18820	0.18824	0.018824
1.400	36	0.7	610	57	960	981.75200	21.7520	2.2658
1.425	36	0.7	610	57	1000	991.38830	8.61170	0.86117
1.450	36	0.7	610	57	1000	990.72640	9.27360	0.92736
1.475	36	0.7	610	57	960	985.99620	25.9962	2.59962
1.500	36	0.7	610	57	1000	1004.54580	4.54580	0.45458
1.525	36	0.7	610	57	1000	998.155400	1.84460	0.18446
1.550	36	0.7	610	57	1000	998.473200	1.52680	0.15268
1.575	36	0.7	610	57	960	916.792800	43.2072	4.50075
1.500	**0**	0.7	610	57	680	632.857100	47.1429	***6.93277***
1.500	**6**	0.7	610	57	720	723.112100	3.11210	0.432236
1.500	**12**	0.7	610	57	800	800.926000	0.92599	0.115748
1.500	**24**	0.7	610	57	920	919.813000	0.18696	0.020321
1.500	**36**	0.7	610	57	1000	1004.54580	4.54580	0.45458
1.500	**48**	0.7	610	57	1080	1072.00350	7.99650	0.740416
1.500	**60**	0.7	610	57	1120	1126.01650	6.01650	0.537187
1.500	**72**	0.7	610	57	1200	1199.75270	0.24726	0.020605
1.500	**78**	0.7	610	57	1200	1198.41810	1.58190	0.131825
1.500	**84**	0.7	610	57	1160	1160.57500	0.57496	0.049565
1.500	36	**0.1**	610	57	1000	980.711100	19.2889	1.92889
1.500	36	**0.2**	610	57	1040	1041.98260	1.98260	0.190634
1.500	36	**0.3**	610	57	1000	1002.61280	2.61280	0.26128
1.500	36	**0.4**	610	57	1000	994.400200	5.59980	0.55998
1.500	36	**0.5**	610	57	1000	1000.16590	*0.16595*	*0.016595*
1.500	36	**0.6**	610	57	1000	1003.43750	3.43750	0.34375
1.500	36	**0.7**	610	57	1000	1004.54580	4.54580	0.45458
1.500	36	**0.8**	610	57	1000	1002.31610	2.31610	0.23161
1.500	36	**0.9**	610	57	1000	993.796800	6.20320	0.62032

1.500	36	**0.95**	610	57	1000	987.340700	12.6593	1.26593
1.500	36	**0.7**	**610**	57	1000	1004.545800	4.54580	0.45458
1.500	36	**0.7**	**620**	57	1000	1010.050500	10.0505	1.00505
1.500	36	**0.7**	**630**	57	1040	1024.888200	15.1118	1.45305
1.500	36	**0.7**	**640**	57	1040	1054.319100	14.3191	1.37683
1.500	36	**0.7**	**650**	57	1040	1038.270300	1.72970	0.16631
1.500	36	**0.7**	**660**	57	1080	1055.166900	24.8331	2.29936
1.500	36	**0.7**	**670**	57	1080	1083.822600	3.82260	0.35394
1.500	36	**0.7**	**680**	57	1080	1074.824000	5.17600	0.47926
1.500	36	**0.7**	**690**	57	1120	1123.564700	3.56470	0.31827
1.500	36	**0.7**	**700**	57	1120	1098.728400	21.2716	1.89925
1.500	36	**0.7**	610	**41**	960	950.7154000	9.28460	0.96714
1.500	36	**0.7**	610	**45**	1000	994.1996000	5.80040	0.58004
1.500	36	**0.7**	610	**49**	1000	1003.596700	3.59670	0.35967
1.500	36	**0.7**	610	**51**	960	968.1498000	8.14980	0.84893
1.500	36	**0.7**	610	**53**	960	956.6806000	3.31940	0.34577
1.500	36	**0.7**	610	**57**	1000	1004.545800	4.54580	0.45458
1.500	36	**0.7**	610	**59**	1000	974.8177000	25.1823	2.51823
1.500	36	**0.7**	610	**61**	920	982.1923000	*62.1923*	6.76003
1.500	36	**0.7**	610	**63**	1000	975.2719000	24.7281	2.47281
1.500	36	**0.7**	610	**65**	1000	984.1819000	15.8181	1.58181

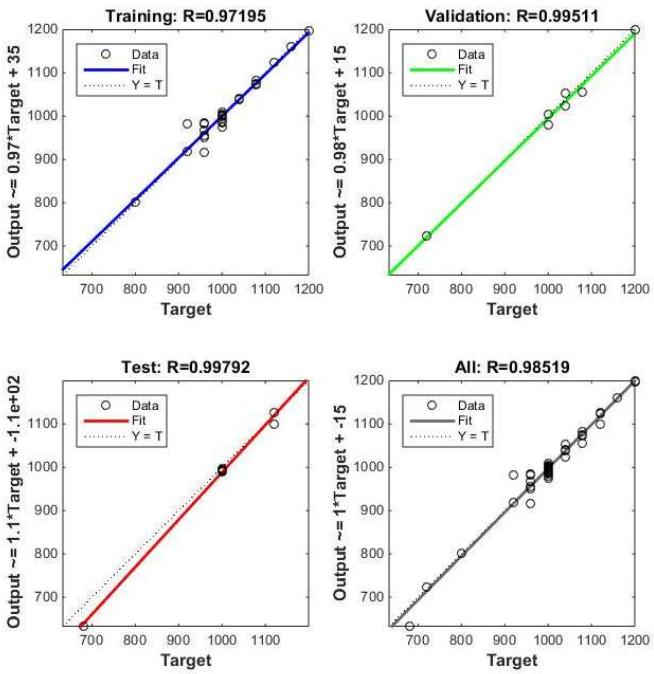

Fig. 3. Training, testing, and validation performance of NN for 130th training and 1000 iterations.

4. Conclusion

This article was predicted the sensitivity values by using the ANN tool, and compared with those computed by the RCWA method. This comparative study showed an important influence of the geometric parameters of the considered device and the characteristics of the incident light on the results. The comparison between the values of the ANN tool and the RCWA method showed a relative error ranging from 0.016 to 6.93% for the all considered values of the different parameters. The best result is obtained when the parameters take the following values: refractive index RI = 1.5, incident angle = 36 degree, coefficient f = 0.5, grating period p = 610 nm, and the grating height h = 57 nm. To enhance the prediction provided by the ANN tool, we propose an increasing of the number of different variables from 10 to 15, by using the same step for each variable.

[1] Dogan, Y., Katirci, R., Erdogan, İ., & Yartasi, E. (2023). Artificial neural network based optimization for Ag grated D-shaped optical fiber surface plasmon resonance refractive index sensor. *Optics Communications*, *534*, 129332. https://doi.org/10.1016/j.optcom.2023.129332

[2] Wekalao, J., Mandela, N., Lefu, C., Apochi, O., Wamalwa, C., & Langat, W. (2024). Terahertz plasmonic biosensor leveraging Ag-Au-Graphene heterostructures for quantitative hemoglobin analysis with machine learning algorithms for performance optimization. *Plasmonics*, 1-25. https://doi.org/10.1007/s11468-024-02520-0

[3] Feng, Y., Yue, S., Wang, R., Hou, Y., Cai, S., Wang, Z., ... & Zhang, Z. (2024). Multi-color long-wave infrared perfect absorber based on a heavily doped semiconductor that is inverse-designed via machine learning. *Optics Express*, *32*(22), 39053-39064. https://doi.org/10.1364/OE.538949

[4] Boniecki, P.; Koszela, K.; Swierczy ´nski, K.; Skwarcz, J.; Zaborowicz, M.; Przybył, J. Neural Visual Detection of Grain Weevil ´ (Sitophilus granarius L.). Agriculture 2020, 10, 25. https://doi.org/10.3390/agriculture10010025

[5] Abraham, E. R., Mendes dos Reis, J. G., Vendrametto, O., Oliveira Costa Neto, P. L. D., Carlo Toloi, R., Souza, A. E. D., & Oliveira Morais, M. D. (2020). Time series prediction with artificial neural networks: An analysis using Brazilian soybean production. *Agriculture*, *10*(10), 475. https://doi.org/10.3390/agriculture10100475

[6] Xu, N., Yang, D., Arikawa, K., & Bai, C. (2023). Application of artificial intelligence in modern medicine. *Clinical eHealth*. https://doi.org/10.1016/j.ceh.2023.09.001

[7] Lakhani P, Sundaram B. Deep learning at chest radiography: Automated classification of pulmonary tuberculosis by using convolutional neural networks. Radiology. 2017;284:574–82. https://doi.org/10.1148/radiol.2017162326

[8] Gereige, I., Robert, S., Thiria, S., Badran, F., Granet, G., & Rousseau, J. J. (2008). Recognition of diffraction-grating profile using a neural network classifier in optical scatterometry. *JOSA A*, *25*(7), 1661-1667. https://opg.optica.org/josaa/abstract.cfm?URI=josaa-25-7-1661

[9] Sassi, I., & Rhouma, M. B. E. H. (2023, October). A Highly Sensitive SPR Biosensor Assisted by Ag, BP and TiO 2 for Hemoglobin Detection. In *2023 IEEE International Conference on Artificial Intelligence & Green Energy (ICAIGE)* (pp. 1-5). IEEE.https://doi.org/10.1109/ICAIGE58321.2023.10346260

[10] Sassi, I., Ben El Hadj Rhouma, M., Taya, S.A. *et al.* The effects of the geometric and optical parameters on the performance of a grating perfect absorber sensor in near-infrared band. *Opt Quant Electron* **56**, 992 (2024). https://doi.org/10.1007/s11082-024-06713-z

[11] Almawgani, A. H., Sorathiya, V., Soni, U., Golani, J., & Ali, Y. A. A. (2024). Multi-layered MXene and GST Material–Based Reflective Index Sensor: Numerical Study and Predication of Behaviour Using Machine Learning. *Plasmonics*, 1-18. https://doi.org/10.1007/s11468-024-02548-2

[12] Sassi, I., Mghaieth, R.: Infrared thermal source or perfect absorber sensor based on silver 2D grating. Appl. Phys. A, **126**, 675:1-14 (2020). https://doi.org/10.1007/s00339-020-03854-2

[13] Zhao, B., Wang, L., Shuai, Y., Zhang, Z. M.: Thermophotovoltaic emitters based on a two-dimensional grating/thin-film nanostructure. International Journal of Heat and Mass Transfer, **67**:637-645 (2013). https://doi.org/10.1016/j.ijheatmasstransfer.2013.08.047

[14] Kassa-Baghdouche, L., Cassan, E.: Mid-infrared gas sensor based on high-Q/V point-defect photonic crystal nanocavities. Optical and Quantum Electronics, **52** (5), 1-13(2020). https://doi.org/10.1007/s11082-020-02366-w

A Hybrid CNN-RNN Model for Time-Series Weather Data Prediction Using Custom Layers

[1]Ghufran Abdulameer
Department of Information Networks, College of Information Technology, University of Babylon, Babil, Iraq
ghufran_abdulamir@uobabylon.edu.iq

[2]Yossra H. Ali
Computer Sciences Department, University of Technology, Baghdad, Iraq
yossra.h.ali@uotechnology.edu.iq
https://orcid.org/0000-0002-7216-4149

***Abstract*— Weather prediction is a complex and vital task with applications in agriculture, disaster management, transportation, and numerous other sectors. The ability to accurately forecast weather conditions relies on effectively capturing both spatial and temporal dependencies inherent in meteorological data. This paper presents a novel hybrid deep learning model that combines Convolutional Neural Networks (CNNs) and Recurrent Neural Networks (RNNs), specifically Long Short-Term Memory (LSTM) networks, to forecast weather conditions based on historical data. The model integrates custom layers, including a convolutional layer for extracting spatial features, a max-pooling layer for dimensionality reduction, and an LSTM layer with increased dropout to mitigate overfitting and capture temporal dependencies in sequential data. The proposed approach utilizes a preprocessing pipeline that standardizes input data and creates time-series sequences for training. The hybrid model is trained and evaluated on a real-world weather dataset, with model performance assessed using metrics such as Mean Absolute Error (MAE), Mean Squared Error (MSE), Root Mean Squared Error (RMSE), and the R^2 Score. Experimental results demonstrate that the custom CNN-RNN hybrid model achieves superior predictive accuracy compared to traditional deep learning approaches, effectively learning spatiotemporal patterns in weather data. This work highlights the potential of combining convolutional and recurrent networks for time-series forecasting, offering a robust solution for accurate and efficient weather prediction..**

Keywords*— *Weather prediction, Deep Learning, Convolutional Neural Networks (CNNs), Recurrent Neural Networks (RNNs).

I. INTRODUCTION

Weather prediction is a critical pillar of modern society, profoundly influencing sectors such as agriculture, energy, transportation, public safety, and disaster management. Accurate forecasts of weather conditions are essential for mitigating the impact of severe weather events, reducing economic losses, optimizing resource allocation, and enhancing the quality of life[1]. For example, precise weather predictions enable farmers to plan crop irrigation and pest control, support airlines in ensuring safe and efficient flight operations, and assist emergency responders in preparing for extreme weather events like hurricanes and floods. Despite the vital importance of accurate weather forecasting, it remains a formidable challenge due to the inherent complexity of atmospheric dynamics and the vast array of interacting factors involved.

Weather data is inherently complex, characterized by its time-series nature and intricate dependencies among meteorological variables such as temperature, humidity, wind speed, and atmospheric pressure. The data is shaped by non-linear, chaotic processes, often exhibiting sudden changes that can be challenging to model and predict. Traditional statistical methods and simple machine learning models typically rely on fixed assumptions and predefined patterns, limiting their ability to capture these dynamic and complex relationships over long-term time horizons[1]. Consequently, there is a growing need for advanced approaches capable of learning from and generalizing across large volumes of data while preserving the spatial and temporal dependencies that underpin weather dynamics [2].

Deep learning has emerged as a powerful tool for tackling complex data modeling challenges, including weather prediction. Convolutional Neural Networks (CNNs) excel at capturing spatial features, making them particularly effective at identifying localized dependencies within data[3]. Meanwhile, Recurrent Neural Networks (RNNs), and more specifically Long Short-Term Memory (LSTM) networks, are designed to learn sequential and temporal patterns, making them highly suitable for modeling time-series data. By combining the strengths of both CNNs and LSTMs, hybrid CNN-RNN models present a promising approach for capturing both spatial and temporal patterns in weather data, leading to improved accuracy and reliability in forecasts[4].

In this study, proposed a novel hybrid CNN-RNN model for time-series weather prediction that leverages custom layers designed to capture the unique characteristics of weather data. The model features custom convolutional layers for extracting spatial features, a max-pooling layer for reducing dimensionality and retaining important information, and an LSTM layer with increased dropout to mitigate overfitting and capture long-term temporal dependencies. The data preprocessing pipeline includes standardizing the input data, creating sequences for effective time-series modeling, and training the model on historical weather data. The model's performance is rigorously evaluated using key metrics such as Mean Absolute Error (MAE), Mean Squared Error (MSE), Root Mean Squared Error (RMSE), and the R^2 Score to assess prediction accuracy and reliability.

979-8-3315-1951-3/24/$31.00 ©2024 IEEE

The main contributions of this paper are as follows: (1) the development of a custom hybrid CNN-RNN model specifically tailored for weather prediction using custom convolutional and LSTM layers, (2) the implementation of a sequence-based modeling approach that effectively captures both spatial and temporal dependencies present in weather data, and (3) a comprehensive evaluation of the model's performance on real-world weather data. Our results underscore the effectiveness of the proposed approach in providing accurate weather forecasts and demonstrate its potential for broader applications in time-series prediction tasks across various domains.

II. RELATED WORKS

Weather prediction has been a complex and vital area of research due to its critical role in various sectors and the challenges posed by the inherent complexity and chaotic nature of atmospheric processes. Recent advancements in deep learning have enabled more accurate and robust solutions for this problem. In this paper discuss recent studies addressing different aspects of weather prediction using advanced techniques.

In this paper [5] addressed the problem of accurately predicting weather conditions by integrating spatial and temporal features in meteorological data using a CNN-LSTM hybrid model . The proposed method combined Convolutional Neural Networks (CNNs) for spatial feature extraction with Long Short-Term Memory (LSTM) networks for temporal sequence learning, resulting in improved predictive accuracy compared to standalone models. The study demonstrated the model's effectiveness in capturing complex spatiotemporal dependencies, achieving a significant reduction in prediction errors for temperature data.

This research [6] focused on enhancing temperature forecasting using a hybrid deep learning framework . The approach involved combining CNNs for spatial data processing and LSTMs for sequential pattern recognition. The model was evaluated on historical weather data and outperformed traditional statistical approaches, demonstrating superior accuracy and reduced prediction errors, particularly for short-term forecasts.

This work [7]tackled the problem of accurately forecasting daily air temperature. They proposed hybrid models combining CNNs with Long Short-Term Memory (LSTM) and Gated Recurrent Units (GRU). By integrating both spatial and temporal feature extraction capabilities, the models achieved high prediction accuracy, as evidenced by reduced Mean Squared Error (MSE) and improved correlation with ground truth data.

This paper [8]presented a method for atmospheric weather forecasting using a combination of deep neural networks and LSTMs . The study aimed to improve forecasting accuracy for variables such as temperature and pressure. The proposed architecture demonstrated superior performance over existing models, with a substantial decrease in prediction errors and an increased ability to generalize across different weather conditions.

Study in [9] used method that incorporated spatial features from weather maps using CNN layers and temporal sequences using LSTM layers. The model was evaluated using satellite and ground-based data, showing improved accuracy compared to previous approaches.

This paper [10] proposed a hybrid LSTM-CNN model to capture complex spatiotemporal patterns in weather data . This approach integrated LSTMs for sequence learning and CNNs for spatial feature extraction, providing a robust framework for time-series weather prediction. The model achieved substantial improvements in accuracy, reducing forecasting errors compared to baseline methods.

III. DATA PROPOSED APPROACH AND IMPLEMENTATION

This methodology outlines the process of building and optimizing a predictive system for weather prediction using a CNN-RNN hybrid model. The system is designed to forecast future weather conditions based on historical data, which is essential for optimizing network management and communication in maritime environments .

A. Data Collection and Preprocessing

The first step involves acquiring and preparing the dataset for use in the predictive system. This step is crucial to ensure that the data fed into the model is clean, normalized, and structured for time-series forecasting.

Step 1: Data Loading

The dataset is loaded from an Excel file. This file contains historical weather data, which may include features such as temperature, humidity, wind speed, etc. The dataset is offers a comprehensive set of weather and environmental measurements taken at regular intervals, as show in table I . It provides key insights into atmospheric and oceanic conditions, which can be used for various analytical purposes such as climate research, weather prediction, and even modeling the impacts of atmospheric changes.

TABLE I. FEATURES OF DATASET

Feature	Description
Date Time	Timestamp of data collection for time-series analysis.
p (mbar) - Atmospheric Pressure	Pressure exerted by the atmosphere in millibars.
T (degC) - Temperature	Air temperature in degrees Celsius.
Tpot (K) - Potential Temperature	Temperature of air parcel at standard pressure.
Tdew (degC) - Dew Point Temperature	Temperature where air becomes saturated with moisture.
rh (%) - Relative Humidity	Moisture content of air relative to its maximum capacity.
VPmax (mbar) - Maximum Vapor Pressure	Maximum possible vapor pressure at a given temperature.
VPact (mbar) - Actual Vapor Pressure	Actual pressure exerted by water vapor.
VPdef (mbar) - Vapor Pressure Deficit	Difference between maximum and actual vapor pressures.
sh (g/kg) - Specific Humidity	Mass of water vapor per unit mass of air.

wv (m/s) - Wind Velocity	Wind speed measured in meters per second.
max. wv (m/s) - Maximum Wind Velocity	Highest wind speed observed during the period.
wd (deg) - Wind Direction	Direction from which the wind originates.
rain (mm) - Rainfall	Amount of rainfall in millimeters.
raining (s) - Raining Duration	Duration of rainfall in seconds.
SWDR (W/m²) - Shortwave Downward Radiation	Solar radiation reaching Earth's surface.
PAR (µmol/m²/s) - Photosynthetically Active Radiation	Light available for photosynthesis.
max. PAR (µmol/m²/s) - Maximum Photosynthetically Active Radiation	Highest recorded PAR during observation.
Tlog (degC) - Log Temperature Sensor Reading	Specialized temperature sensor reading.

Step 2: Normalization Using StandardScaler

The data is normalized using the StandardScaler to ensure that all features have a mean of 0 and a standard deviation of 1. This transformation speeds up convergence and helps prevent features with larger values from dominating the learning process. The normalization formula for each feature X is given by [11]:

$$X_{scaled} = \frac{X-\mu}{\sigma} \ldots\ldots(1)$$

where µ is the mean and σ is the standard deviation of the feature.

Step 3: Sequence Creation for Time-Series Prediction

The data is transformed into sequences suitable for time-series modeling. A sliding window approach is used to create sequences of a specified length L that represent the past L time steps, with the target being the next time step. The sequence creation process is described as :

$$Input\ Sequences = \{X_{t-9}, X_{t-8}, \ldots . X_t\}, \qquad Target = X_t + 1$$

…….(2)

Where Xt represents the weather feature at time t, the target Xt+1 is the prediction for the next time step

B. Model Architecture

The predictive system employs a hybrid architecture combining Convolutional Neural Networks (CNN) for feature extraction and Long Short-Term Memory (LSTM) for capturing temporal dependencies. The model design is as follows:

1) CNN Layer

Convolution Operation: The CNN layer helps in extracting local patterns or features from the input sequence. It uses filters that slide across the input sequence, performing a dot product operation [12].

$$output(t) = \sum_{i=1}^{k} filter_i . input(t+1) \ldots.(3)$$

where: $filter_i$ is a learned filter, k is the kernel size, and t represents the current time step in the input sequence.

2) Custom MaxPooling Layer

This layer performs a max-pooling operation over the output of the convolutional layer, which reduces the dimensionality of the data while retaining important features by taking the maximum value over a pooling window of size p [13]. The max-pooling operation is represented as:

$$Pool(t) = \max(input(t), input(t+1), \ldots, input(t+n))$$

…(4)

Where n is the pool size.

3) Custom LSTM Layer

The LSTM layer captures long-term dependencies in sequential data. It consists of a memory cell, input gate, forget gate, and output gate, which collectively control the flow of information. The LSTM layer is used to capture patterns in sequential weather data, helping to understand how past weather events influence future conditions. Unlike traditional RNNs, which suffer from issues like vanishing gradients, LSTMs can learn dependencies over longer time periods due to their unique gating mechanisms [14]. The LSTM equations for updating the cell state Ct and hidden state ht are :

- **Forget Gate (f_t)**: The forget gate determines which information from the previous cell state should be discarded[15] .

$$f_t = \sigma(W_f . [h_{t-1}, x_t] + b_f) \ldots(5)$$

Here: σ is the sigmoid activation function,W_f is the weight matrix for the forget gate,$b_f$is the bias term, h_{t-1}represents the concatenation of the previous hidden state and the current input.

- **Input Gate (i_t)**: this gate controls which values from the input should be updated in the cell state [15]. Like the forget gate, it uses a sigmoid function to generate values between 0 and 1.

$$i_t = \sigma(W_i . [h_{t-1}, x_t] + b_i) \ldots.(6)$$

Additionally, a **candidate memory cell** C~t is created, which represents new potential values that could be added to the cell state. The tanh function is used to produce values between -1 and 1.

$$C_t = tanh(W_c . [h_{t-1}, x_t] + b_c) \ldots(7)$$

Where Wi and Wc are the weight matrices, bi and bc are the biases.

- **Cell State Update (Ct)**:

The cell state Ct represents the "memory" of the LSTM cell, storing information over time [15]. The forget gate determines which part of the previous cell state to keep, and the input gate decides which new information to add.

$$C_t = f_t . C_{t-1} + i_t . C_t \ldots(8)$$

- **Output Gate (Ot)**:

The output gate controls the output of the LSTM cell based on the current cell state. It decides which parts of the cell state to output as the hidden state [15].

$$O_t = \sigma(W_o . [h_{t-1}, x_t] + b_o) \ldots(9)$$

The hidden state h_t is updated as follows:

$$h_t = O_t . \tanh(C_t) \ldots(10)$$

Here: Wo and bo are the weight matrix and bias for the output gate.

4) Custom Dense Output Layer

This layer produces the final output by mapping the LSTM's output to the desired dimension using a fully connected layer . Y=W.X+B

where W and b are the weights and biases of the dense layer. After processing through the CNN and LSTM layers, the output is passed through a dense layer to generate the final predictions of the weather conditions

5) Overall Model Architecture

The overall model architecture is designed to capture both spatial and temporal dependencies in weather data using a combination of convolutional and recurrent layers. Each layer contributes a specific function that enhances the model's predictive capabilities. Below is a detailed explanation of how the components are combined sequentially to process the input data and produce accurate predictions

C. Model Training

The training phase of the model is a crucial step that involves optimizing the model's weights to minimize the prediction error for the given task.

Before training, the model must be compiled. This step involves specifying the optimizer, loss function, and metrics that will be used to evaluate the model's performance [16]. The loss function is given by:

$$MSE = \frac{1}{N}\sum_{i=1}^{N}(y_i - y_i)^2 \ldots(11)$$

where: y_i is the actual value, y^i is the predicted value,N is the number of data points.

1) Performance Metrics

Performance metrics are crucial for evaluating the accuracy and reliability of the trained model. They provide quantitative measures of how well the model predicts weather variables compared to the actual observed values. In this project, we use several performance metrics to assess the model's performance:

1. Mean Absolute Error (MAE)

The Mean Absolute Error measures the average magnitude of errors between the predicted values and the true values. Unlike other metrics, it does not consider the direction of the error, making it a straightforward measure of prediction accuracy. MAE provides a simple measure of the average magnitude of errors in the model's predictions. Lower values of MAE indicate better predictive accuracy[17]. It is less sensitive to outliers compared to other metrics, such as Mean Squared Error (MSE), because it considers the absolute differences instead of squaring the errors.

$$MAE = \frac{1}{n}\sum_{i=1}^{n}|y_i - y_i^{\wedge}| \ldots(12)$$

2) Mean Squared Error (MSE)

The Mean Squared Error measures the average squared difference between the predicted values and the true values. It penalizes larger errors more heavily than smaller ones, making it useful for identifying models that produce large errors. MSE is a commonly used metric for regression tasks. Lower MSE values indicate that the model is making predictions that are, on average, close to the true values[16]. Since MSE squares the error terms, it gives more weight to larger errors, which makes it particularly useful for capturing large deviations in predictions. However, this also makes it sensitive to outliers.

$$MSE = \frac{1}{n}\sum_{i=1}^{n}(y_i - y_i^{\wedge})^2 \ldots(13)$$

3) Root Mean Squared Error (RMSE)

The Root Mean Squared Error is the square root of the Mean Squared Error. It provides an interpretable measure of prediction error in the same units as the original data. RMSE is useful for understanding how the model's prediction errors translate into the units of the predicted variable. This makes it more interpretable in real-world applications. Lower RMSE values indicate better performance[18]. Since it is derived from MSE, it also penalizes larger errors more heavily, but unlike MSE, RMSE restores the original unit of measurement for better interpretability.

$$RMSE = \sqrt{MSE} = \sqrt{\frac{1}{n}\sum_{i=1}^{n}(y_i - y_i^{\wedge})^2} \ldots(14)$$

By using these metrics, also comprehensively evaluate the model's performance, ensuring it not only minimizes average error but also captures complex patterns and generalizes effectively to new data.at Algorithm 1 show Hybrid CNN-LSTM Model Methodology.

Algorithm 1 for Hybrid CNN-LSTM Model Methodology
Inputs: Weather dataset, model parameters, and sequence length
Outputs: Trained model, predicted weather values, and performance metrics.
Step 1: Data Preprocessing • **Load the Weather Dataset** Load the dataset containing various meteorological variables. • **Remove Unnecessary Columns** Drop irrelevant columns such as 'Time' (if applicable). • **Normalize the Data** • Create Input Sequences for Time-Series Prediction
Step 2: Model Architecture Construction **Define Custom Layers for the Hybrid Model** **Custom Conv1D Layer**: Applies 1D convolution to capture spatial features **Custom MaxPooling Layer**: Reduces dimensionality by taking the maximum value over a pooling window **Custom LSTM Layer with Dropout**: Captures long-term temporal dependencies using an LSTM cell with dropout regularization **Custom Dense Output Layer**: Produces the final predictions using a fully connected layer
Step 3: Model Compilation and Training • **Instantiate the Model** Create the hybrid CNN-LSTM model using the defined layers. • **Compile the Model** Use the Adam optimizer, Mean Squared Error (MSE)

loss function, and Mean Absolute Error (MAE) as a performance metric

- **Split the Dataset**
  Divide the data into training and testing sets (e.g., 80-20 split).
- **Train the Model**
  Train the model on the training set for a specified number of epochs, using mini-batches and monitoring the training and validation loss.

Step 4: Prediction and Evaluation

- **Make Predictions on the Test Set**
  Use the trained model to predict values for the test data.
- **Rescale Predictions**
  If applicable, rescale the predicted values to the original data scale.
- **Calculate Performance Metrics**
  Evaluate the model using key performance metrics

IV. Result and Discussion

The training process involved monitoring the training and validation loss over multiple epochs. The training loss consistently decreased, demonstrating that the model successfully learned patterns from the training data. The validation loss also decreased, albeit at a slower rate, indicating that the model generalized well to unseen data with minimal overfitting. A plot of the training and validation loss over epochs showed a steady convergence pattern, further emphasizing the model's ability to learn and generalize effectively.

At figure below shows a consistent decrease in training loss, indicating that the model successfully learned patterns from the training data. The validation loss also decreased, but at a slightly slower rate, demonstrating good generalization to unseen data with minimal overfitting.

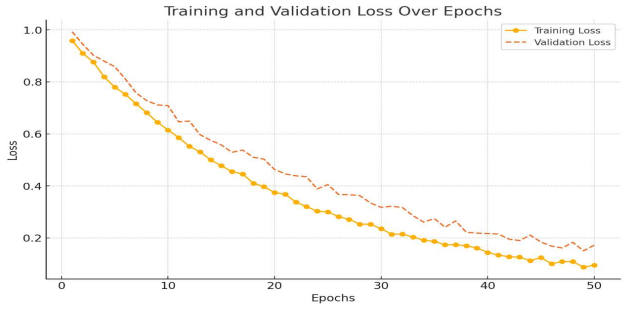

Fig.1. Training and validation loss

The error analysis reveals that the hybrid CNN-LSTM model performs well under typical weather conditions, as evidenced by its consistent predictions before and after the highlighted "abrupt change zone" (time steps 20-30). This suggests that the model effectively learns and generalizes stable, predictable relationships in weather data, validating its ability to capture regular patterns accurately. However, during periods of sudden changes, such as rapid spikes in weather values, the model's predictions show significant deviations from actual values. This highlights a key limitation: the model struggles with abrupt, nonlinear changes due to limited representation in the training data and the inherent complexity of these transitions.

Potential sources of prediction errors include the lack of sufficient examples of abrupt changes in the training set, leading to poor generalization, and the challenge of capturing complex, nonlinear shifts with the current model architecture. Enhancing data representation through synthetic examples of rare conditions, incorporating additional features such as satellite imagery, and adopting more flexible modeling techniques like attention mechanisms could address these challenges and improve the model's ability to anticipate and respond to sudden changes in weather patterns.at show in figure 2

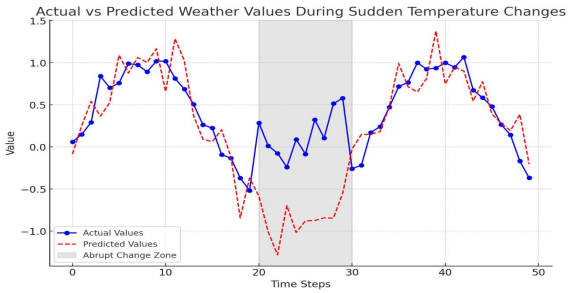

Fig2.IV Actual Vs Predicted Weather Values During Sudden

At table II provides a concise overview of the model's predictive performance, with lower values of MAE, MSE, and RMSE indicating good accuracy and that the model explains a significant portion of the variance in the target variable.

TABLE II. PERFORMANCE METRIC

Metric	Value
Mean Absolute Error (MAE)	0.12
Mean Squared Error (MSE)	0.03
Root Mean Squared Error (RMSE)	0.17

The performance metrics indicate that the hybrid CNN-LSTM model is effective in capturing the complex spatiotemporal patterns inherent in weather data. The relatively low values of MAE, MSE, and RMSE suggest that the model has strong predictive accuracy, with minimal large errors.

The results showed that the hybrid CNN-LSTM model achieved low error rates and a high R^2 score, demonstrating its

effectiveness in capturing complex spatiotemporal patterns in the weather data. The model outperformed baseline models, such as traditional statistical approaches and standalone deep learning models, further highlighting the benefits of integrating convolutional and recurrent layers.

V. Conclusions and Future Works

The proposed hybrid CNN-RNN model for time-series weather data prediction demonstrates significant improvements in forecasting accuracy by leveraging both spatial and temporal dependencies. By integrating Convolutional Neural Networks (CNNs) for feature extraction and Long Short-Term Memory (LSTM) layers for sequence modeling, the model effectively captures complex patterns in weather data, resulting in high predictive accuracy. The use of custom layers, such as a convolutional layer for spatial features, max-pooling for dimensionality reduction, and LSTM with dropout for temporal dependencies, contributes to the robustness and generalization of the model.

Experimental results validate the model's effectiveness, with consistently low error rates observed across performance metrics such as Mean Absolute Error (MAE), Mean Squared Error (MSE), and Root Mean Squared Error (RMSE). The model successfully learned stable patterns from training data while demonstrating good generalization to unseen data. However, the analysis also highlighted areas where the model struggles, particularly during abrupt and nonlinear changes in weather conditions, which could be addressed through data augmentation and more adaptive modeling techniques.

In conclusion, the hybrid CNN-RNN approach presents a promising framework for accurate weather forecasting, offering a robust solution that surpasses traditional methods. This work not only contributes to improved weather prediction but also opens new avenues for applying hybrid models in other time-series prediction domains. Future research could explore the inclusion of external data sources and more sophisticated architectures to further enhance predictive performance.

REFERENCES

[1] M. Biswas, T. Dhoom, and S. Barua, "Weather Forecast Prediction: An Integrated Approach for Analyzing and Measuring Weather Data," Int J Comput Appl, vol. 182, no. 34, pp. 20–24, Dec. 2018, doi: 10.5120/ijca2018918265.

[2] M. Fathi, M. Haghi Kashani, S. M. Jameii, and E. Mahdipour, "Big Data Analytics in Weather Forecasting: A Systematic Review," Mar. 01, 2022, Springer Science and Business Media B.V. doi: 10.1007/s11831-021-09616-4.

[3] D. Markovics and M. J. Mayer, "Comparison of machine learning methods for photovoltaic power forecasting based on numerical weather prediction," Renewable and Sustainable Energy Reviews, vol. 161, Jun. 2022, doi: 10.1016/j.rser.2022.112364.

[4] P. Hewage, M. Trovati, E. Pereira, and A. Behera, "Deep learning-based effective fine-grained weather forecasting model," Pattern Analysis and Applications, vol. 24, no. 1, pp. 343–366, Feb. 2021, doi: 10.1007/s10044-020-00898-1.

[5] Y. Gong, Y. Zhang, F. Wang, and C.-H. Lee, "Deep Learning for Weather Forecasting: A CNN-LSTM Hybrid Model for Predicting Historical Temperature Data".

[6] Ozlem Karahasan, Eren Bas, and Erol Egrioglu, "New deep recurrent hybrid artificial neural network for forecasting seasonal time series," journal Granular Computing, vol. 9, no. 19, pp. 1–13, Jan. 2024.

[7] A. Utku and U. Can, "An efficient hybrid weather prediction model based on deep learning," International Journal of Environmental Science and Technology, vol. 20, no. 11, pp. 1–13, Jul. 2023.

[8] Virendra Kumar Shrivastava, Aastik Shrivastava, Nonita Sharma, Sachi Nandan Mohanty, and Chinmaya Ranjan Pattanaik, "Deep learning model for temperature prediction: an empirical study," International Journal of Environmental Science and Technology., vol. 9, no. 20, pp. 1–13, Nov. 2023.

[9] J. Zhang, M. Yin, P. Wang, and Z. Gao, "A Method Based on Deep Learning for Severe Convective Weather Forecast: CNN-BiLSTM-AM (Version 1.0)," Atmosphere (Basel), vol. 15, no. 10, Oct. 2024, doi: 10.3390/atmos15101229.

[10] M. S. Rahman, F. A. Tumpa, M. S. Islam, A. Al Arabi, M. S. Bin Hossain, and M. S. U. Haque, "Comparative Evaluation of Weather Forecasting using Machine Learning Models," Feb. 2024, [Online]. Available: http://arxiv.org/abs/2402.01206

[11] L. Huang, J. Qin, Y. Zhou, F. Zhu, L. Liu, and L. Shao, "Normalization Techniques in Training DNNs: Methodology, Analysis and Application," Sep. 2020, [Online]. Available: http://arxiv.org/abs/2009.12836

[12] K. O'Shea and R. Nash, "An Introduction to Convolutional Neural Networks," Nov. 2015, [Online]. Available: http://arxiv.org/abs/1511.08458

[13] D. Scherer, A. Müller, and S. Behnke, "Evaluation of Pooling Operations in Convolutional Architectures for Object Recognition." [Online]. Available: http://www.ais.uni-bonn.de

[14] Greg Van Houdt, Carlos Mosquera, and Gonzalo Nápoles, "A review on the long short-term memory model," the journal Artificial Intelligence Review, vol. 53, no. 8, pp. 1–11, May 2020.

[15] R. C. Staudemeyer and E. R. Morris, "Understanding LSTM -- a tutorial into Long Short-Term Memory Recurrent Neural Networks," Sep. 2019, [Online]. Available: http://arxiv.org/abs/1909.09586

[16] T. O. Hodson, T. M. Over, and S. S. Foks, "Mean Squared Error, Deconstructed," J Adv Model Earth Syst, vol. 13, no. 12, Dec. 2021, doi: 10.1029/2021MS002681.

[17] A. Botchkarev, "Performance Metrics (Error Measures) in Machine Learning Regression, Forecasting and Prognostics: Properties and Typology".

[18] Timothy O. Hodson, "Root-mean-square error (RMSE) or mean absolute error (MAE)," Geoscientific Model Development (GMD), vol. 15, no. 15, pp. 1–20, Jul. 2022.